1-1-2016

Wave Interaction With Epsilon-znd-Mu-Near-Zero (emnz) Platforms and Nonreciprocal Metastructures

Ahmed Mohamed Abdelwahab Mahmoud
University of Pennsylvania, amwmahmoud@gmail.com

Wave Interaction With Epsilon-znd-Mu-Near-Zero (emnz) Platforms and Nonreciprocal Metastructures

Abstract
The concept of metamaterials has offered platforms for unconventional tailoring and manipulation of the light-matter interaction. In this dissertation, we explore several concepts and designs within this scope. We investigate some of the electromagnetic characteristics of the concept of "static optics", i.e., wave interaction with structures in which both the relative effective permittivity and permeability attain near-zero values at a given operating frequency and thus the spatial distributions of the electric and magnetic fields exhibit curl-free features, while the fields are temporally dynamic. Using such structures, one might in principle 'open up' and 'stretch' the space, and have regions behaving electromagnetically as 'single points' despite being electrically large. We study some of the wave-matter interaction in these platforms and suggest possible designs for implementation of such structures in different frequency regimes and experimentally verify our findings in the microwave regime. Another research direction that is explored in this dissertation is the development of some nonreciprocal metaplatforms. We investigate theoretically an approach through which one-way electromagnetic wave flow can be achieved using properly designed nonlinearity combined with structural asymmetry. The approach is rather general and applicable for any desired frequency regime and opens doors for high performance "electromagnetic diodes" and nonreciprocal metasurfaces and metastructures. We also theoretically study the usage of time-dependent materials in achieving wave flow isolation within plasmonic waveguides environments. We also provide physical remarks on our various findings.

Degree Type
Dissertation

Degree Name
Doctor of Philosophy (PhD)

Graduate Group
Electrical & Systems Engineering

First Advisor
Nader Engheta

Keywords
Metamaterials, Near Zero Paramaters Materials, Nonreciprocity

Subject Categories
Electromagnetics and Photonics | Optics

WAVE INTERACTION WITH EPSILON-AND-MU-NEAR-ZERO (EMNZ) PLATFORMS AND NONRECIPROCAL METASTRUCTURES

Ahmed M. Mahmoud

A DISSERTATION

in

Electrical and Systems Engineering

Presented to the Faculties of the University of Pennsylvania

in

Partial Fulfillment of the Requirements for the

Degree of Doctor of Philosophy

2016

Supervisor of Dissertation

Nader Engheta , H. Nedwill Ramsey Professor of Electrical and Systems Engineering

Graduate Group Chairperson

Alejandro Ribeiro, Rosenbluth Associate Professor of Electrical and Systems Engineering

Dissertation Committee

Jan Van der Spiegel, Professor of Electrical and Systems Engineering

Dwight Jaggard, Professor of Electrical and Systems Engineering

Firooz Aflatouni, Skirkanich Assistant Professor

WAVE INTERACTION WITH EPSILON-AND-MU-NEAR-ZERO (EMNZ) PLATFORMS AND NONRECIPROCAL METASTRUCTURES

To my family, my friends, time and music. To those questions that were never asked, most of which have been answered along the way, and to those answers that appeared to be irrelevant at the time but made the most sense afterwards.

ACKNOWLEDGMENT

I would like to thank my adviser Prof. Nader Engheta for his continuous support throughout the program. I would also like to thank all the students and postdocs at the Fields and Waves laboratory.

ABSTRACT

WAVE INTERACTION WITH EPSILON-AND-MU-NEAR-ZERO (EMNZ) PLATFORMS AND NONRECIPROCAL METASTRUCTURES

Ahmed. M. Mahmoud

Nader Engheta

The concept of metamaterials has offered platforms for unconventional tailoring and manipulation of the light-matter interaction. In this dissertation, we explore several concepts and designs within this scope. We investigate some of the electromagnetic characteristics of the concept of "static optics", i.e., wave interaction with structures in which both the relative effective permittivity and permeability attain near-zero values at a given operating frequency and thus the spatial distributions of the electric and magnetic fields exhibit curl-free features, while the fields are temporally dynamic. Using such structures, one might in principle 'open up' and 'stretch' the space, and have regions behaving electromagnetically as 'single points' despite being electrically large. We study some of the wave-matter interaction in these platforms and suggest possible designs for implementation of such structures in different frequency regimes and experimentally verify our findings in the microwave regime. Another research direction that is explored in this dissertation is the development of some nonreciprocal metaplatforms. We investigate theoretically an approach through which one-way electromagnetic wave flow can be achieved using properly designed nonlinearity

combined with structural asymmetry. The approach is rather general and applicable for any desired frequency regime and opens doors for high performance “electromagnetic diodes” and nonreciprocal metasurfaces and metastructures. We also theoretically study the usage of time-dependent materials in achieving wave flow isolation within plasmonic waveguides environments. We also provide physical remarks on our various findings.

TABLE OF CONTENTS

LIST OF TABLES

LIST OF ILLUSTRATIONS

CHAPTER 1: Introduction

The field of telecommunications has been a milestone in the development of civilization throughout the history of mankind. Starting from smoke signals that were used as a simple mean of long distance communications to transfer simple information like the availability of food or water or the presence of danger. Then with the discovery of electricity, exploiting it in telegraphs and later on integrating it with electromagnetic theory a huge boom in human civilization took place resulting in launching and spreading of TVs and radios. The significant progress in wired and wireless communications that accompanied the World War II has eventually led to another big step in the world which in turn led to the satellite and internet technologies taking over almost every aspect of our lives since the beginnings of the twenty first century. We currently live in a world where telecommunications is of great importance to every human being, and with global directions towards a more connected world through the so called the “Internet of Things” and utilizing big data links we as electrical engineers are required to come up with innovative solutions. The field of electronics currently plays a major role in almost every aspect of our life, but what about a world where electronics and photonics go hand in hand in a complementary and innovative fashion ? one can imagine that there are no limits to the possibilities that can be achieved. For example, in the area of telecommunications, merging electronics and optics can eventually lead to an extreme boost in the data transfer rates, to the order of Tb/s, orders of magnitude higher than the current conventional rates. The possibilities are, however not limited to

telecommunications. This merge would open the door for a new era in solar energy utilization [1], high resolution lithography [2], and medical treatment and biosensing [3] among many other applications. Thus, photonics and electromagnetics in general add lots of possibilities and degrees of freedom. However conventional electromagnetic and photonic components are not easily integratable and consequently the task of creating flexible non bulky photonic systems and components is a bottle neck that needs to be surpassed in order to open all those possibilities. In this thesis we discuss several research directions through which we are approaching and trying to resolve some of those challenges by proposing novel concepts and pushing electromagnetics and photonics to the "extreme". The flexibility of electronics and the concept of modularization (the ability of designing each stage in electronic systems separately and assembling the whole system relatively easily), in addition to the relative simplicity of electrical interconnects has been a key factor in its progress throughout the years. Part of the reason in the success and power of on-chip electronics is such flexibility. However, the design of electromagnetic and photonic systems and waveguide bends and interconnects is a rather complicated process that requires extensive design and optimization efforts. Can we achieve geometrically-flexible, or geometrical-invariant photonics ?

From an electromagnetic perspective, in simple terms, the main reason for the difference between the electronic and the photonic systems is that two points in space separated by an arbitrary distance ordinarily experience two different phase values that depend on various parameters, including signal's frequency and refractive indices of the media by which these points are surrounded. Can we engineer these media such that the two points

"feel electromagnetically the same" at that frequency, regardless of their distance and the structure around them? In other words, can we imagine an electromagnetic system that under some conditions and with proper design would effectively follow "static" distribution spatially, but at the same time being dynamic temporally? By proper engineering, one can design media with effective relative permittivity and permeability near zero, resulting in zero effective refractive index and stretching the effective wavelength for that frequency, thus endowing uniform phase value across such media so the two distant points exhibit the same phase. We have explored the notion of "static optics" [4], in which electricity and magnetism may be effectively decoupled macroscopically [5] thus the monochromatic fields are spatially distributed statically, while being temporally dynamic [4]. Using such epsilon-and-mu-near-zero(EMNZ) medium, one may in principle 'stretch' the space, and have regions behaving electromagnetically as 'single points' despite being large and arbitrarily shaped [4,5]. One way is to utilize photonic bandgap structure with Dirac dispersion and accidental degenary as shown by Chan and his group [6]. In this dissertation we propose another route: we have theoretically and experimentally studied how the insertion of a simple dielectric rod in a single unit of 2D epsilon-near-zero(ENZ) host with arbitrary cross-sectional shape can lead to effective EMNZ properties [4]. The ENZ host can be selected from a variety of nonmagnetic materials/structures such as transparent conducting oxides for the near-infrared region, polar dielectric materials for the mid-infrared domain, and a parallel-plate waveguide with metallic walls operating at its TE_{10} cut-off frequency for the microwave region the latter of which we demonstrated experimentally. The EMNZ structures can provide

exciting platforms for sculpting light-matter interaction with unconventional classical and quantum optical features.

Another research direction that is explored in this dissertation is the development of nonreciprocal (NR) metaplatforms. We introduce an approach through which one-way electromagnetic wave flow can be achieved using properly designed nonlinearity 7,8. The approach is rather general and applicable for any desired frequency regime. It relies on the difference in the field profiles along a non-symmetric structure exhibited when the structure is excited from opposite ends. Thus, if a non-linearly loaded planar resonator is placed at a plane where the ratio of the local fields excited from both sides is significant, the resonance frequency of the resonator would be different when excited from different ends of the structure. This leads to different transmission rates at the operating frequency depending on the wave flow direction. As a proof of concept, one-way waveguide is designed and verified numerically. Building on those findings, we propose and study a new concept for observing nonreciprocal polarization rotation (such as Faraday rotation) in passive structures without any biases (neither electrical (voltage or current), nor magnetic bias) 8. Fan and his group proposed the concept of breaking transmission symmetry using spatio–temporal modulation 9. This spatio–temporal refractive index modulations that simultaneously impart frequency and wave vector shifts during the photonic transition process would lead to a process of mode conversion for a wave propagating in one direction, while no mode conversion happens for a wave propagating in the opposite direction. Thus, with a notch filter designed at the frequency of the second mode one would achieve one way flow of light. We build on those findings and

investigate such behavior in plasmonic Metal/Dielectric/Metal waveguide and prove analytically and numerically the ability of such waveguides to achieve this isolation over smaller footprints. In addition, owing to the plasmonc nature of those waveguides we analytically reveal a new operation mode where complete wave flow isolation is theoretically possible, ommitting the need for the notch filter and consequently further reducing the system complexity.

In the following chapters, we will discuss the details of our findings.

CHAPTER 2: Wave-matter interaction in epsilon and mu near zero (EMNZ) structures

2.1 Introduction

Throughout the past several years, there have been extensive research efforts in the field of metamaterials[10–14] – artificial structures that exhibit unusual properties that do not readily exist in nature. Recently there has been great interest in the near-zero parameters materials. This is the category of metamaterials whose relative permittivity is near zero (i.e., epsilon-near-zero (ENZ)), or relative permeability is near zero (i.e., mu-near-zero (MNZ)), or both relative permittivity and permeability are near zero (i.e., epsilon-and-mu-near-zero (EMNZ)). The special feature of such media basically lies in having a low wave number (i.e., stretched wavelength) as a consequence of the near-zero refractive index that leads to a relatively small phase variation over physically large region of such media. This has opened the door to various interesting wave phenomena and applications. One track in which this category of metamaterials was utilized efficiently is the field of antenna design, where ENZ or EMNZ materials were considered for tailoring the radiation patterns, i.e., to attain highly directive radiation patterns [5,15–20], or for significantly enhancing the radiation efficiency [21–23]. On the other hand, near-zero-parameters materials have also been extensively studied and used as means to realize unconventional tunneling of electromagnetic energy within ultra-thin sub-wavelength ENZ channels or bends (a phenomenon coined as supercoupling) [24–27], tunneling through large volumes using MNZ structures [28] and to overcome the problem of weak coupling

between different electromagnetic components that are conventionally not well matched, e.g. in a coaxial to waveguide transition [29]. Another interesting field of research has been about manipulating the transmission characteristics using near zero media [30–33] where such media have been loaded by certain properly designed inclusions that allow shaping of the system's transmission profile.

Recently, the field of anisotropic near-zero parameters media has also been explored, adding extra degrees of freedom and thus achieving some interesting phenomena [34–37] . Moreover, zero parameters materials have been integrated with non-linear elements to achieve controllable transmission [38] or to enhance the non-linear response of Kerr-based structures in the optical regime [39,40]. Owing to the numerous potential applications and novel physical phenomena that can result from such media, great efforts have been put into the actual realization of those media, from naturally available materials [41–43] to using photonic crystals that exhibit dirac cones dispersion [6,44,45] and structures in the microwave regime [46,47], and suggestions for the more challenging optical regime [40, 41] where gain media has usually been exploited to overcome the problem of high losses [42].

It is also worth mentioning here the research efforts related to the so-called DB boundary conditions, namely the set of boundary conditions that require vanishing normal components of **D** and **B** vectors at the interface. Within that context, reflection of arbitrary plane waves was analyzed for the planar DB boundary by Lindell and Sihvola [51] and it was shown that transverse electric (TE) and transverse magnetic (TM) waves are reflected from respective perfect electric conductor and perfect magnetic conductor planes [51]. Moreover, possible realizations of the DB boundary in terms of an interface of

uniaxially anisotropic metamaterial half-space with zero axial parameters media or sheets has also been studied by the same authors [51–53]. However in those works the main emphasis was on plane waves with oblique incidence angles, showing that such interfaces can act as spatial filters reflecting plane waves incident at any angle for both polarizations with the exception of a narrow window around normal incidence.

In this chapter, we shed light on some of the other exotic phenomena of EMNZ media in bounded scenarios, providing a study regarding two of the main pillars of electromagnetic behavior within EMNZ bounded environments, namely its scattering properties and its interaction with emitting dipoles. Moreover, building on the findings in earlier works [25] we propose a design scheme that provides us with both effective permittivity and effective permeability near zero over a relatively large "empty" volume, and discuss the limitations [4].

2.2 "Opening up" the space

Since in such an EMNZ medium, both $\nabla \times \mathbf{E} = 0$ and $\nabla \times \mathbf{H} = 0$ simultaneously, the electric and magnetic phenomena are decoupled and spatially distributed statically, while still temporally dynamic[10]. This leads to a paradigm in which we may have optical phenomena while the field distributions are static-like, effectively having a scenario as "DC optical circuits". Having such an EMNZ region, as shown in Fig.1(a), we can break an air-filled parallel-plate waveguide at a point, and effectively "open up" or "stretch" the space between two parts of this waveguide, without affecting external electromagnetic entities and quantities, implying that we can have an electromagnetically large bounded

physical volume, that would have otherwise influenced the electromagnetic wave propagation externally, but now owing to the EMNZ effect it behaves as if it is a ‘single point’ electromagnetically as viewed from the external world. The external boundary of the entire two-dimensional (2D) region shown in Fig. 1 (except for the input and output exit ports) is perfect electric conducting (PEC) wall. As depicted in a 2D simulation shown in Fig. 1(b), perfect transmission (with unit magnitude and zero phase difference) from the input to the output port is preserved regardless of the arbitrary shape and size of the EMNZ region. Moreover, in this 2D simulation of the EMNZ region, the magnetic field spatial distribution is uniform while the electric field is distributed spatially as though a “battery” is connected between the top and the bottom plates of the EMNZ region.

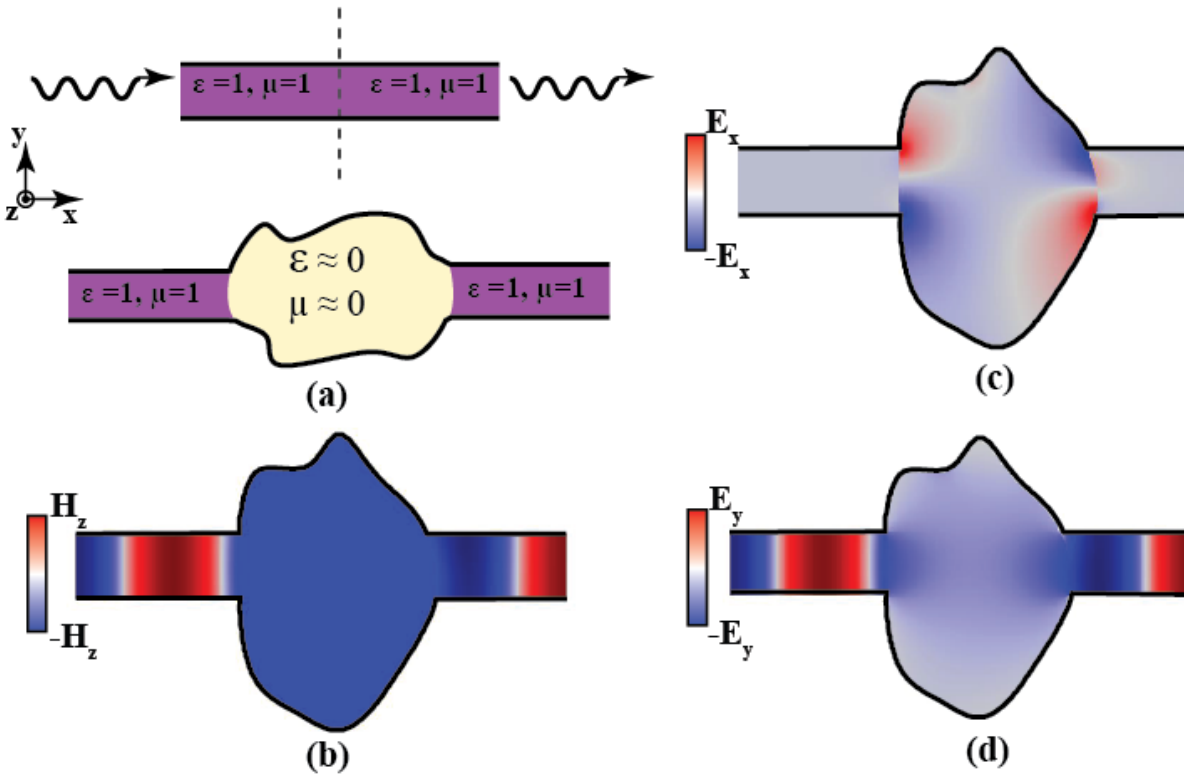

***Fig. 1**: **EMNZ medium as an "electromagnetic point"**: (a) Schematic of an epsilon-and-mu-near-zero (EMNZ) medium emulating opening up or stretching the space at the dotted line between the two sections of an air-filled parallel-plate waveguide, while keeping the region as a "single point" electromagnetically. (b) Snapshot of the z-component of the magnetic field distribution (shown with blue color) and the x-component (c) and y-component (d) of the electric field distributions over the proposed two-dimensional structure with an arbitrarily shaped cross section filled with an idealized EMNZ material. The external walls (except at the exits of the two ports) are made of perfectly electric conductor (PEC).*

2.3 Scattering within EMNZ media

An interesting phenomenon that takes place within EMNZ bounded environments is the unconventional scattering performance of perfectly electric conducting (PEC) objects

embedded in an EMNZ medium. Recently, there has been some works investigating the behavior of zero-index media when loaded by various structures and the ability of these systems to manipulate the transmission and reflection profile owing to the unique scattering performance within zero-index media [30–33] . Here, using the two-dimensional Mie scattering theory we study the unique scattering performance from two-dimensioanl PEC objects, embedded in a 2D host EMNZ medium. We begin by analytically solving for the scattered fields from a 2D PEC cylinder of radius a embedded in an unbounded EMNZ medium for both the transverse magnetic (TM, i.e., the incident **H** vector is parallel with the cylinder axis) and transverse electric (TE, i.e., the incident **E** vector is parallel with the cylinder axis) incident waves normally incident on the cylinder. For a TM wave, the incident and the scattered fields can be written (assuming $e^{-i\omega t}$ and that the axis of the cylinder is along the z axis) in the time harmonic case as follows

$$\vec{\mathbf{H}} = \hat{z}\mathbf{H}_{\mathrm{o}} \sum_{n=-\infty}^{\infty} i^n J_n(k_{\mathrm{EMNZ}} r) e^{in\phi} \qquad (1)$$

$$\vec{\mathbf{H}}^{\mathrm{s}} = \hat{z}\mathbf{H}_{\mathrm{o}} \sum_{n=-\infty}^{\infty} c_n^{\mathrm{TM}} H_n^{(2)}(k_{\mathrm{EMNZ}} r) \qquad (2)$$

Applying the boundary conditions we find that

$$c_n^{\mathrm{TM}} = -i^n \frac{J_n^{'}(k_{\mathrm{EMNZ}} a)}{H_n^{'(2)}(k_{\mathrm{EMNZ}} a)} e^{in\phi} \qquad (3)$$

Similarly, for the TE case, we can find that

$$c_n^{\mathrm{TE}} = -i^n \frac{J_n(k_{\mathrm{EMNZ}}a)}{H_n^{(2)}(k_{\mathrm{EMNZ}}a)} e^{in\phi} \qquad (4)$$

We investigate the dependence of $|C_n|$ on k_{EMNZ} as depicted in Fig.2(a) and (b). As shown, there exists an interesting difference between the scattering behavior of the cylinder being illuminated by a TM wave versus a TE wave. For the TM mode as shown in Fig. 2(a) the dependence of $|C_n|$ on k_{EMNZ} is relatively weak around the strict zero condition, meaning that for the case where k_{EMNZ} is small but not strictly zero we can still consider having zero $|C_n|$ for all *n*'s. Thus for that mode a conducting cylinder would introduce no scattering and would effectively be totally "cloaked". (An intuitive way to appreciate this point is to consider the fact that in the EMNZ medium, $\mathbf{D} = 0$, and thus $\nabla \cdot \mathbf{D} = 0$. Therefore, no charge can be induced on the surface of this 2D PEC cylinder when illuminated by the TM wave.). On the other hand, Fig. 2(b) shows that for the TE mode $|C_0|$ exhibits a relatively stronger dependence on k_{EMNZ} in vicinity of the strict zero condition, suggesting that for the case where k_{EMNZ} is near zero, but not strictly zero, we should expect a strictly non-zero scattering from the cylinder with the scattered fields being azimuthally symmetric, when illuminated by that mode. These findings are verified numerically in the insets of Fig. 2(a) and (b) where in (a) we see the scattered fields from a PEC 2D cylinder of radius $5\lambda_0$, with λ_0 being the free space wavelength, embedded in an EMNZ unbounded medium, and illuminated by a TM wave. As expected the scattered fields due to the 2D PEC cylinder vanish. On the other hand, the inset of Fig. 2(b) shows the scattered fields from a conducting cylinder of the same radius that is illuminated by a

TE wave. It is shown that for that polarization we get a non-zero scattering only for the *n* = 0 component of the scattered field when the relative permittivity and permeability are near zero (but not strictly zero), as expected. Moreover, the interesting property of PEC objects introducing no scattering being illuminated by a TM wave when embedded in an EMNZ medium still holds regardless of how arbitrarily shaped the EMNZ region and the conducting object are, owing to the ability of EMNZ media to open up the space as discussed before. This is depicted clearly in Fig. 2(c), where a physically large-cross-section 2D PEC cylinder of an arbitrary shape is embedded into the EMNZ bounded region with another arbitrary shape connected to two air-filled parallel-plate waveguides, shown in Fig. 1(b), providing no scattering at all, with unity transmission and almost no phase progression as the wave traverses the EMNZ region containing this cylinder. (As in Fig. 1, the external boundary (except for the input and output ports) is made of PEC wall. The two parallel-plate waveguides connected to the 2D EMNZ region are filled with air). The numerical results shown in Figs. 1 and 2 were achieved using the RF module of the finite-element-method commercial software COMSOL Multiphysics®, using triangular meshing of maximum element size $\lambda_0 / 30$, where λ_0 is the operating wavelength in free space.

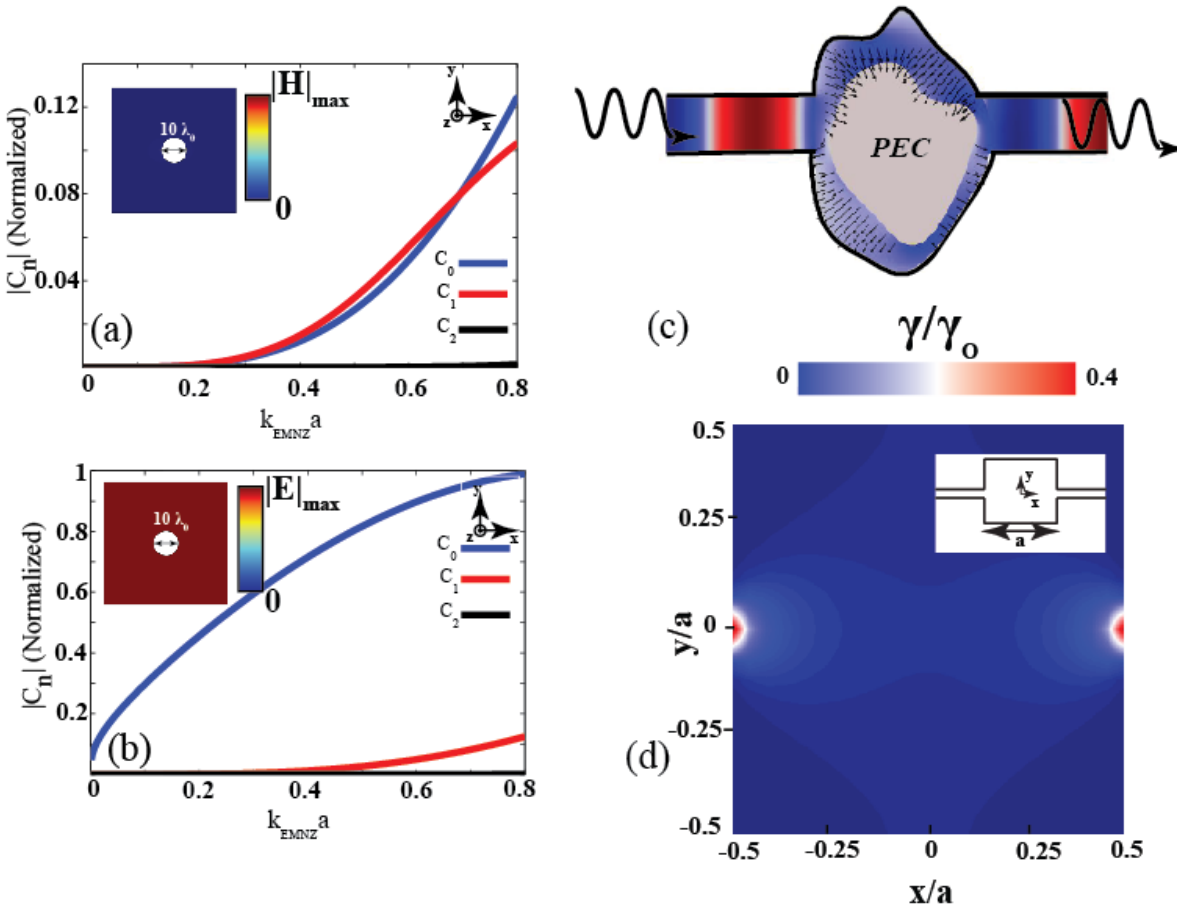

Fig. 2: ***Mie scattering coefficients and spontaneous emission rate in EMNZ.*** *Mie scattering coefficients for (a) TM mode, (b) TE mode. Two-dimensional scattered magnetic field from a 2D conducting cylinder of radius* $5\lambda_0$ *embedded in an ideal EMNZ medium when illuminated by TM mode (inset (a)), and two-dimensional scattered electric field from a conducting cylinder of radius* $5\lambda_0$ *embedded in an ideal EMNZ medium when illuminated by TE mode (inset (b)). (c) Snapshot of the two-dimensional electric (shown as arrows) and magnetic (shown as blue color) field distributions in a two-dimensional EMNZ region, loaded with a conducting cylinder, both with arbitrarily*

shaped cross sections. External walls (other than the exits of the two ports) are assumed to be PEC walls. (d) Distribution of normalized spontaneous emission rate of a two-dimensional electric dipole inside the two-dimensional EMNZ enclosure with two ports connected to parallel-plate waveguides filled with air, versus the dipole position within the structure. The geometry of the EMNZ enclosure and the two air-filled parallel-plate waveguides are shown in the inset.

2.4 Spontaneous emission rate of emitters in presence of EMNZ media

In this section we investigate the behavior of emitting dipoles in presence of arbitrarily shaped EMNZ media, and more specifically how the EMNZ environment influences the spontaneous emission rate of emitters leading to some interesting unprecedented behavior. In [24] the phenomenon of supercoupling that relies on energy squeezing through subwavelength narrow channels has been introduced in epsilon-near-zero (ENZ) metamaterials. Owing to the substantial electric field enhancement within the narrow ENZ channel, placing an electric-dipole emitter within that ENZ channel leads to significant emission enhancement that can be quantitatively described in terms of the dipole's spontaneous emission rate γ as compared to its emission rate in free space γ_o i.e., γ / γ_o [26,54]. However, a unique feature of such structure as compared to any other resonant system coupled to a radiating element or molecule is the nearly uniform phase distribution of that enhanced electric field along the channel, which is in principle independent of the channel length. This leads to the independence of the emission

enhancement on the dipole's location within the channel[26,54]. In an EMNZ medium on the other hand, the supercoupling phenomenon is still preserved, however, without the need for ultranarrow subwavelength channels as was the case for ENZ media, which in addition to providing a larger platform to place the dipole within the medium, leads to no mandatory enhancement in the fields within the EMNZ region. This may lead to the novel effect of emission inhibition regardless of the position of the dipole within the EMNZ region. To numerically demonstrate that phenomenon, we investigate the 2D structure shown in the inset of Fig. 2(d), where a two-dimensional y-oriented dipole is placed within a $5\lambda_0 \times 5\lambda_0$ bounded enclosure filled with an ideal EMNZ material connected to two narrow parallel-plate waveguides filled with air. (The cross-sectional shape of this 2D EMNZ region is chosen arbitrarily. The external boundary, except for the two ports, is make of PEC wall). As shown in Fig. 2(d) where a color map of two-dimensional distribution of γ/γ_o versus the dipole location within the EMNZ region is shown, we get significant emission inhibition (i.e, γ/γ_o less than unity) within the EMNZ region as expected. Owing to the reciprocity, this γ/γ_o distibution resembles the distribution of the y-component of the electic field when this structure is fed with the transverse electromagnetic (TEM) mode incident from one of the air-filled parallel-plate waveguide port. Finally, that for the normalized spontaneous emission rate calculations shown in panel (d) of Fig. 2 a two-dimensional dipole emitter has been used whose dipole moment has been fixed and for each location the total radiated power was calculated numerically from which the corresponding spontaneous emission rate can be found

analytically and normalized to the spontaneous emission rate of the same dipole moment at the same frequency in free space.

2.5 Proposed Design (2D)

Now we explore a scenario in which a properly selected single dielectric inclusion within a host medium whose permittivity (or effective permittivity) is near zero may lead to simultaneously having effective permittivity and permeability near zero. It was shown in previous work [25] that with an ENZ host medium one can also achieve an effective MNZ by periodically loading this host medium with inclusions of proper dimensions and permittivity. In this section we show that this can be extended into a non-periodic case with arbitrary shape of the cross section, and that even within one unit cell, which can be arbitrarily large and not limited to a sub-wavelength size, we can still have both effective permittivity and permeability near zero.

The first proposed structure in which we theoretically demonstrate the EMNZ behavior is shown in Fig. 3, where we have an input channel that is a 2D air-filled parallel plate waveguide (region 1) feeding the 2D region of interest (region 2) which is filled with a host medium whose permittivity follows the Drude model $\varepsilon_h = \varepsilon_0\left(1-\frac{\omega_p^2}{\omega(\omega+i\Gamma)}\right)$, where ω_p is the plasma frequency, Γ is the collision frequency (that is assumed to be zero, i.e., a lossless medium). This medium obviously behaves as ENZ at the plasma frequency. This region is enclosed by PEC walls and is connected to another output channel, another air-filled parallel plate waveguide (region 3). We choose

the inclusion to be a 2D dielectric rod of radius R and permittivity ε_i , which when embedded in an ENZ host, one can achieve an effective permeability shown in [25] to be

$$\mu_{eff} = \mu_o \left(\frac{A_{h,cell}}{A_{cell}} + \frac{2\pi R^2}{A_{cell}} \frac{1}{k_i R} \frac{J_1(k_i R)}{J_0(k_i R)}\right) \quad \text{at } \omega_p \qquad (5)$$

where A_{cell} is the total area of the unit cell and is equal to $a \times a$, $A_{h,cell} = A_{cell} - \pi R^2$, and $k_i = \omega\sqrt{\varepsilon_i \mu_o}$. As mentioned before, we are interested in a zero effective permeability, thus we search for $(k_i R)$ versus the normalized radius $\frac{R}{a}$ for which we achieve zero effective permeability are shown in Fig. 4(a). Since our main goal is to achieve a large enough inclusion-free region where the EMNZ behavior is exhibited, we choose to investigate a scenario where $\frac{R}{a}$ is very small, e.g., $1/15$ for three different cases namely $a = \lambda$, 1.5λ, and 3λ. The required dielectric constant for the rod inclusion to achieve zero effective permeability turns out to be 33.23, 14.77, and 3.69 respectively. In Fig. 5, for the three cases, it is verified that even within a single unit cell that can be several wavelengths large we achieve the EMNZ behavior of "opening up" the space, as suggested by the perfect transmission between the input and output ports and the uniform phase within the proposed EMNZ region. As shown in Fig. 6, the EMNZ behavior shows to be preserved regardless of the location of the single dielectric rod within the unit cell, which provides us with a large enough "real-state" with effective epsilon and mu near zero, within which we can exploit the exotic EMNZ features discussed in previous sections.

Moreover, we show that for a fixed 2D cross-sectional area, radius and permittivity of the dielectric inclusion, we would always get the structure to behave as EMNZ regardless of its arbitrary cross-sectional shape. Therefore, using the same findings of the previous discussion, for the case of a normalized radius $1/15$ and a unit cell area of $\lambda \times \lambda$ we investigate two different cross-sectional shapes for the unit cell to prove our concept. In Fig. 7 we use a circular-cross-section enclosure, while in Fig. 8 we have an arbitrarily-shaped-cross-section enclosure, and we note that the EMNZ behavior is still preserved for both cases. As shown from the required permittivities for achieving the near-zero effective permeability, it is clear that as we increase the size of the region of interest, within which we are aiming for EMNZ behavior, we need smaller values of permittivities, for example the value required for $3\lambda \times 3\lambda$ region is 3.69 which in the range of permittivities of readily available materials like Lithium Niobate. Fig. 4(b) shows the required dielectric constant of the rod to achieve a zero effective permiability for $R = \frac{\lambda}{8}$ versus the normalized area $\frac{A_{cell}}{\lambda^2}$. The numerical simulation has been performed using similar approach to the one used in Figs. 1 and 2.

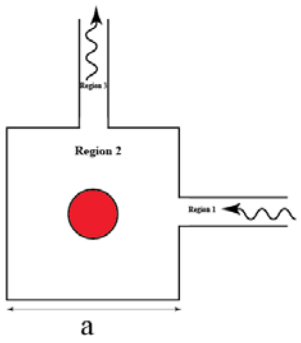

Fig. 3 Geometry of the proposed 2D structure in which a dielectric rod is inserted in an ENZ host medium, causing region 2 to behave as EMNZ medium.

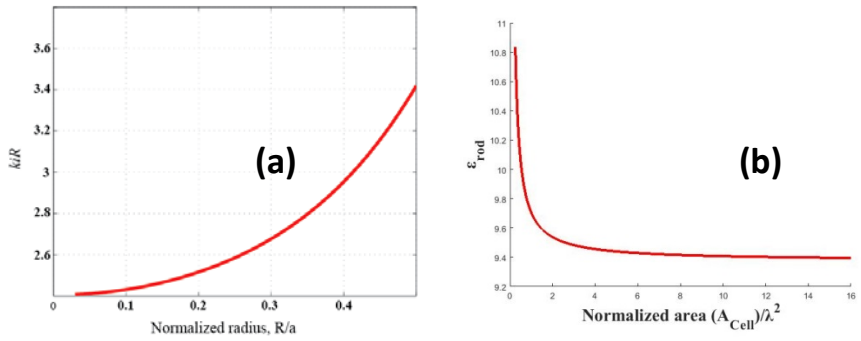

Fig. 4 Investigating the dependence of the dielectric constant of the rod to achieve EMNZ behavior on geometrical aspects, *Plot of the (a) required normalized index of refraction of the rods as a function of the normalized radius R/a, in order , (b) required permittivy of the rods as a function of the normalized area to achieve* $\mu_{eff} = 0$.

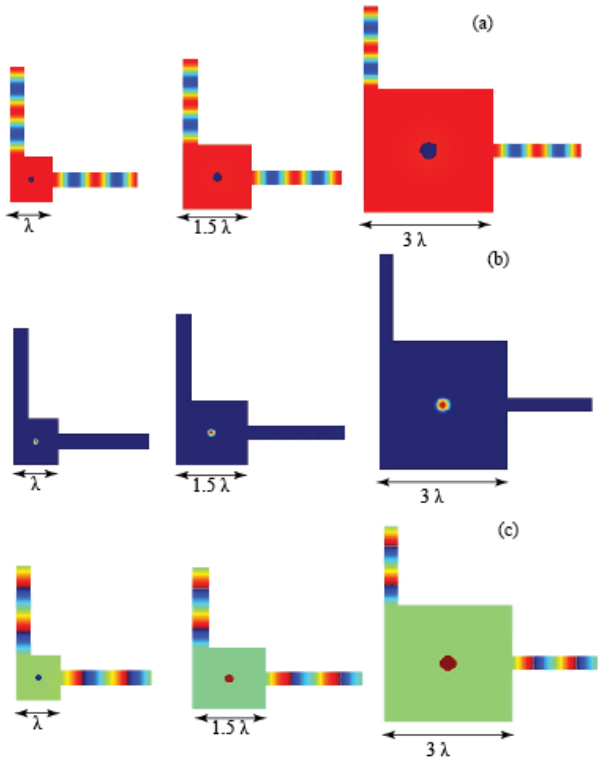

Fig. 5 The proposed 2D structure to exhibit EMNZ behavior for a normalized radius R/a ***of*** $1/15$ *, (a) Snapshot of the magnetic field distribution for* $a=\lambda$, $a=1.5\lambda$, $a=3\lambda$, *(b) Amplitude and (c) phase of the magnetic field distribution for* $a=\lambda$, $a=1.5\lambda$, $a=3\lambda$.

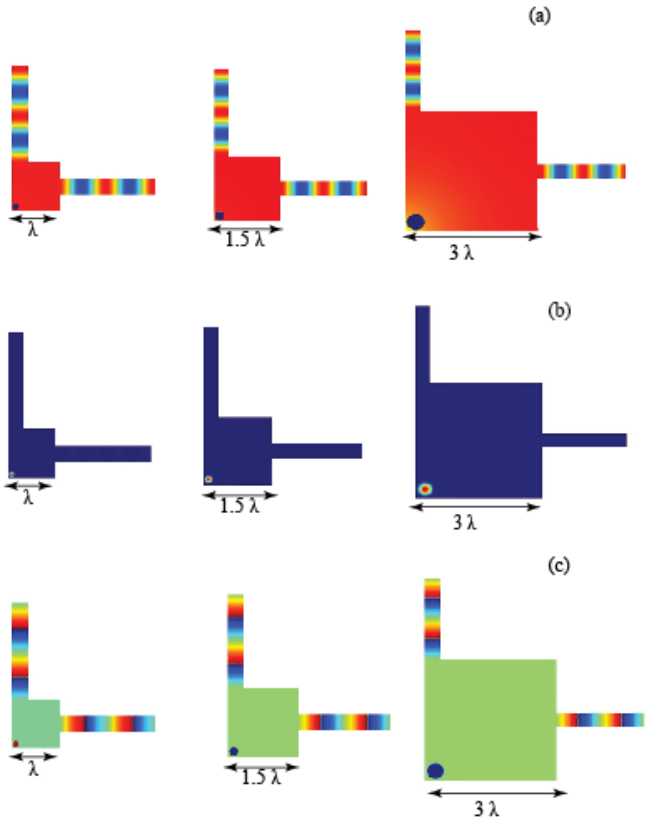

Fig. 6 Similar to Fig. 5, except the 2D dielectric inclusion is moved to the corner of the region. The structure still behaves as an EMNZ.

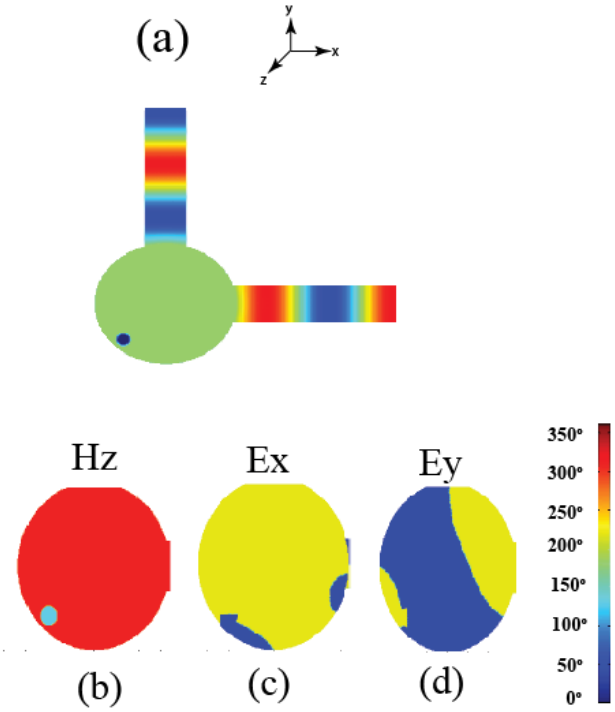

Fig. 7 The proposed 2D structure to exhibit EMNZ with a circular cross section behavior for a normalized radius R/a ***of*** $1/15$ *(a) Snapshot of the magnetic field distribution, Phase of (b) magnetic field Hz, (c) x-component of the electric field, and (d) y-component of the electric field over the EMNZ region.*

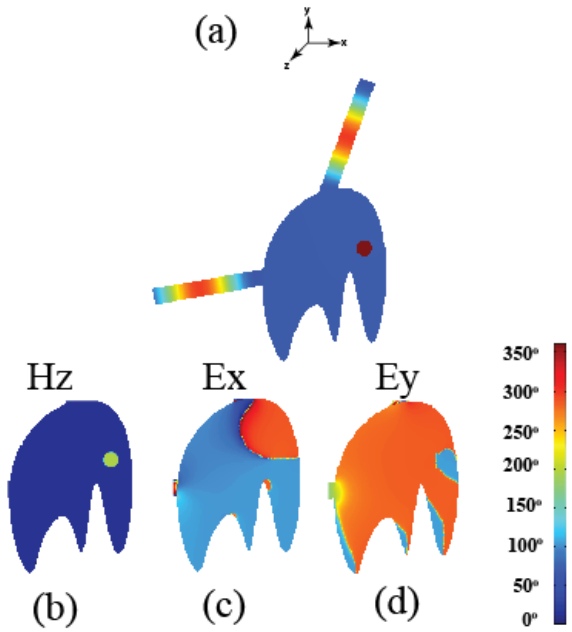

Fig. 8 Similar to Fig. 7, except the cross section of the structure is chosen to be arbitrary.

2.6 Proposed Design (3D)

Now we propose a practical design in which the interesting features of EMNZ can be studied in the microwave regime. At such frequencies, ENZ materials are not readily available in nature, however it has been shown in [55] that parallel metallic plates can simulate a two-dimensional artificial plasma when the TE10 mode is considered. The effective permittivity of the such waveguide structures follows a Drude-like model, i.e., $\varepsilon_{\mathrm{h}}/\varepsilon_0 = \varepsilon_{\mathrm{d}} - (\frac{\pi}{k_0 d})^2$, where ε_d is the relative permittivity of the dielectric between the metallic plates, d is the separation between the metallic plates, and k_0 is the wave

number in free space. In such an environment, if d is chosen to be $\lambda_0/2$, where λ_0 is the free space wavelength at some chosen operating frequency ω_c we need to load this waveguide with a material of permittivity $\varepsilon_i + 1$, in order to emulate a material with relative permittivity ε_i. Thus as shown in Fig. 9(a) the input and output channels that are required to emulate an air-filled parallel plate waveguide with the TEM mode are mimicked using TE_{10} mode in rectangular waveguides filled with a dielectric of relative permittivity of 2 (regions 1 and 3). In the proposed EMNZ region (region 2 in the middle) the ENZ host medium is emulated by a waveguide filled with dielectric of relative permittivity of 1. We choose the inclusion to be a circular-cylinder dielectric rod of radius *R* and permittivity ε_i. For $a = 1.3\lambda_0$ with a dielectric rod of radius $0.13\lambda_0$ requires the rod's relative permittivity to be 9.82. We show that even using only one unit cell we still get almost perfect transmission at the operating frequency ω_c as numerically shown in Fig. 9(b) as opposed to getting almost no transmission in absence of the dielectric rod. Fig. 9(c) shows a cross section of the distribution of the magnitude of the magnetic field at the middle plane within the structure, and the almost perfect transmission between the two ports is evident here, with almost uniform phase within the proposed EMNZ region as shown in Fig. 9(d). Thus, it is numerically verified that our proposed structure acquires the desired EMNZ behavior of opening up the space with near unity magnitude and zero phase transmission between the two ports. Intuitively, the presence of the dielectric rod, when designed properly, generates enough magnetic field inside the rod mostly in the opposite direction to the magnetic field in the ENZ region (i.e., outside the rod) in order

to make the total flux of $\mu_0\mathbf{H}$ to reach zero, achieving an effective near-zero permeability. The above design with the PEC walls is suitable for the microwave frequencies, in which highly conductive materials are readily available. However, in the optical regime, the metallic walls are lossy. The effect of this loss and an alternative design using the photonic bandgap dielectric structures as the walls suitable for the optical frequencies are discussed in a following section. It is worth pointing out here that a small amount of mode coupling from the original TE_{10} mode to the TM_{10} mode may occur due to the curved boundary of the rod's cross section in the middle structure, since these two modes have the same cut-off frequencies in the parallel-plate waveguides. However, such small mode coupling may be reduced by adding few tiny conducting wires around the dielectric rod. This will be discussed in a following section. We should mention that that the numerical results shown in Fig. 9 were performed using the time domain solver of the commercial software CST Microwave Studio®, using automatic meshing.

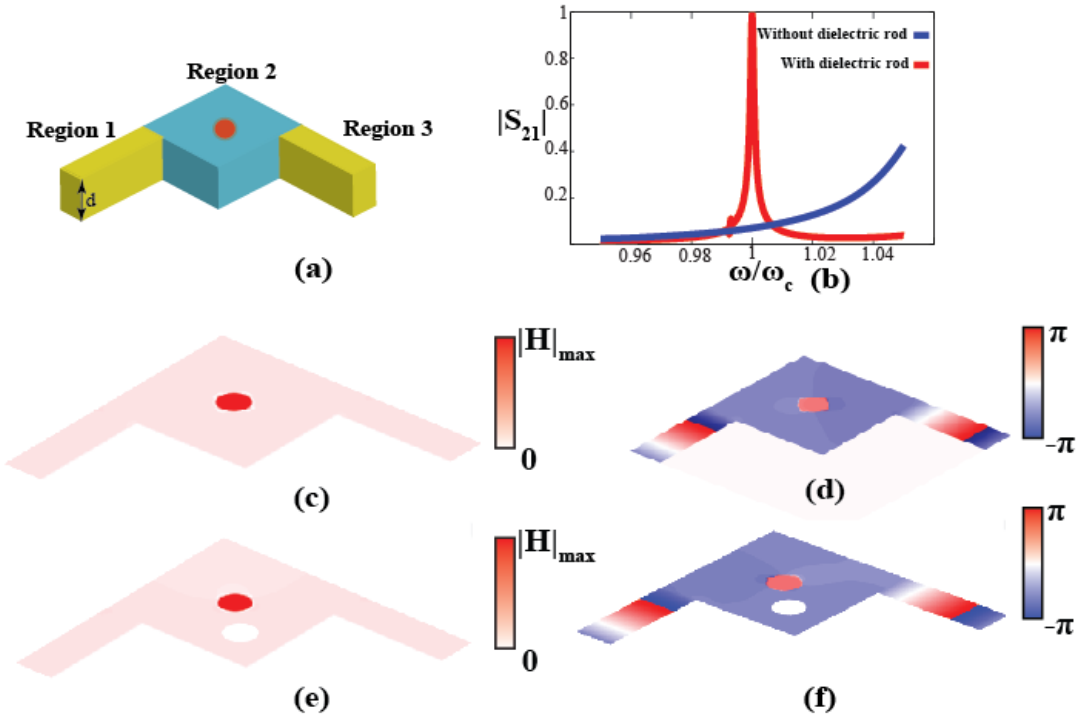

***Fig. 9**: **Proposed design for a structure imitating effectively an EMNZ medium**: (a) Geometry of rectangular air-filled metallic waveguide structure (middle region, blue) with a dielectric rod inclusion (red) emulating the EMNZ behavior. This middle section is connected to two idential dielectric-filled metallic rectangular waveguides (yellow) as the two ports (b) Magnitude of the transmission coefficient (S_{21}) of the structure shown in (a) vs normalized frequency, when fed by one of the waveguide ports. Here ω_c is the cut-off radian frequency of the waveguide section. Blue and red curves are for the cases of with and without the dielectric rod, respectively. (c) Amplitude and (d) phase of the magnetic field in the middle plane within the structure, when it is illuminated by a wave coming from one of the ports; (e) and (f) Amplitude and phase of the magnetic field in the*

middle plane within the structure when the PEC scattering cylinder is also inserted.

Next, we proceed to investigate whether having a PEC cylinder embedded in our proposed effectively EMNZ structure would introduce no scattering for the incident mode with the magnetic field vector parallel with the axis of the cylinder as discussed previously. This is depicted clearly in Figs. 9(e) and (f) where a PEC cylinder of radius $0.13\lambda_0$ is embedded into the proposed structure. It is worth mentioning here that now loading the EMNZ unit cell with a conducting cylinder, the effective area of the unit cell is reduced, and that consequently for the same radius of a dielectric rod, the rod's permittivity has to be adjusted to take that into account. As depicted clearly in Fig. 9(e) and (f) the PEC rod does not introduce any scattering as expected.

Finally we investigate an electric-dipole emission performance within our proposed structure. The phenomena of opening up the space and the unique scattering performance within an EMNZ medium are effectively "global" phenomena, i.e., they can be described using effective media approaches. On the contrary, the dipole spontaneous emission rate is a phenomenon that is highly dependent on its "local" surrounding environment. Thus one might expect the spontaneous emission inhibition phenomenon that was discussed previously within a idealized EMNZ medium would not necessarily take place within our proposed structure, whose "effective" permittivity and permeability exhibit near zero values (while the local material parameters may differ from zero), but the radiation from the ports may be influenced by such effective EMNZ characteristics. We numerically examine the radiation of a given x-oriented short 3D electric dipole placed in various

locations inside our proposed design for the effectively EMNZ bounded structure with two ports to the outside region. As shown in Fig. 10(a), where γ/γ_o distribution as a function of the 3D dipole's location within the proposed structure is given, there exists a significant enhancement in the spontaneous emission rate of such a dipole when it is located in proper locations within the structure. This enhancement is more pronounced towards the center of the structure, completely consistent with reciprocal scenario when one would get high values of electric field near the dielectric rod, if the incident energy were fed as a TE_{10} mode through one of the waveguide ports. This can also be explained by noting that as the dipole gets closer to the center, the fundamental mode of the dielectric rod (that is the mode for which effective zero permeability is achieved) is better coupled to the dipole emission. One of the highlights of the dipole emission in such an effectively EMNZ structure is the intriguing phenomenon of the equal distribution of the radiated power between the two output ports (due to the uniformity of the phase within the structure), regardless of the relative location of the 3D dipole to either of the ports and regardless of the location of the ports connected to the structures. This is shown in Fig. 10(b), (c), and (d) where moving the dipole from the center to the corner or towards the left port does not introduce any change on the ratio between the powers exiting the two ports. Specifically, while the total radiated power from the dipole may depend on its location inside this structure (e.g., this total power is weaker in Fig. 10(c) and 10(d) than in Fig. 10(b)), this power is divided equally as it exits from the two ports when the two ports' cross sections are the same. This intriguing power division is independent of how close the dipole may be located near one of the ports and is also independent of where the

two ports are connected to the structure. As can be seen in Fig. 10(c), the waves exiting from the two ports are the same in each case (with the same amplitude and phase), even though the dipole is very close to the left port and far from the right port. This implies that the radiation from the dipole couples to the two ports the same way despite of unequal distance of the dipole from the two ports. This phenomenon may have important implications in quantum optics and the photon entanglement in such platforms. The numerical results shown in Fig. 10 were performed using the time domain solver of the commercial software CST Microwave Studio®, using automatic meshing. For the normalized spontaneous emission rate calculations shown in panel (a) of Fig. 10 a point dipole emitter has been used whose dipole moment has been fixed and for each location the total radiated power was calculated numerically from which the corresponding spontaneous emission rate can be found analytically and normalized to the spontaneous emission rate of the same dipole moment at the same frequency in free space.

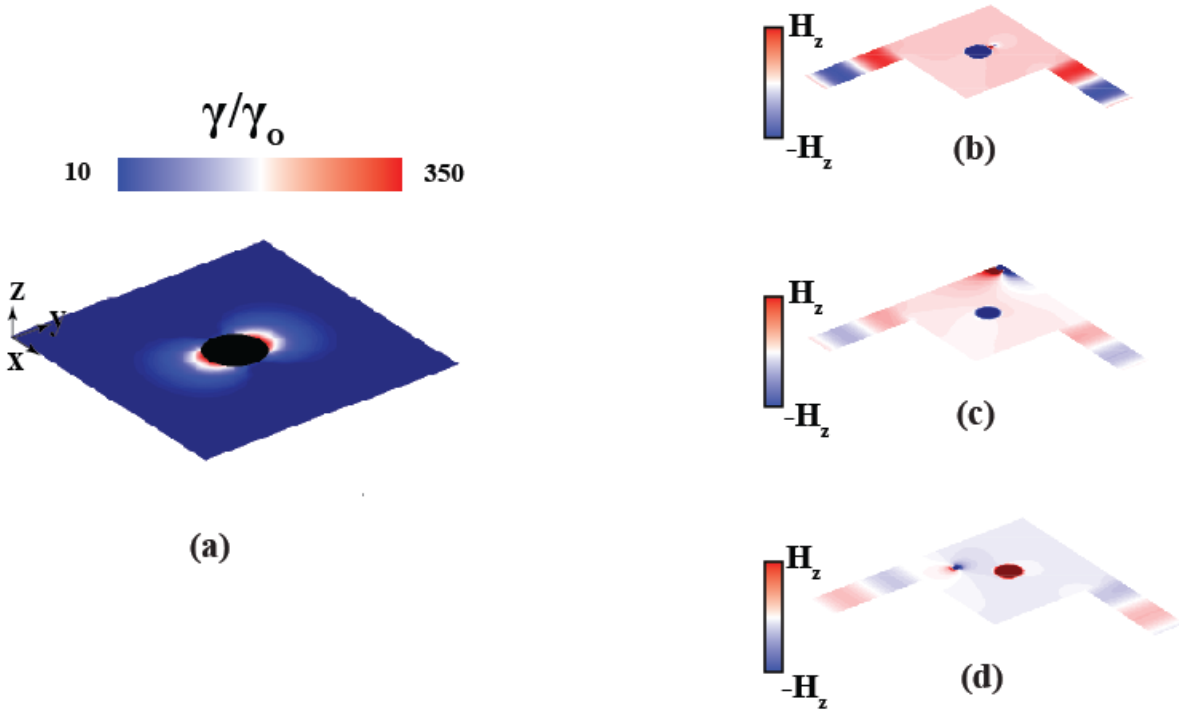

***Fig. 10**: **Emission of a dipole located inside the proposed structure**: (a) Distribution of the normalized spontaneous emission rate of the x-oriented short electric dipole versus the dipole position within the designed enclosure imitating EMNZ medium. (b) A snapshot of the magnetic field of the dipole radiation within the structure with the short electric dipole placed close to the center. (c) as in (b) but the dipole is brought to the corner of the structure. (d) as in (b) but the dipole is brought close to the left port. While the total radiated power is different in (b), (c), and (d), the power exited from the two ports is divied equally in each case, regardless of the location of the dipole within the structure and the relative location of dipole to the ports.*

To summarize, in this section we have theoretically and numerically explored some

of the intriguing phenomena of dipole emission and wave scattering in EMNZ bounded structures, and have proposed a design using a single dielectric rod embedded in a metallic waveguide near its TE_{10} cut-off frequency, imitating the medium with both effective relative permittivity and permeability near zero. We have numerically shown that this design exhibits the relevant features of the EMNZ structures.

2.7 Using Silver instead of PEC

Silver is often one of the candidate metals in the optical and near IR regime. In this section, we investigate the effect of lossy walls, using Silver for the walls of the waveguide discussed in Fig. 9, instead of idealized PEC. First, using the same design flow we proposed in the previous section for the case of PEC wall, we choose the parameters of the waveguide to operate at the telecommunication wavelength of $1.5\mu m$. For this case the height of the waveguide is about $\lambda_0 / 2$. However, for this design, which is originally for the PEC case, when we use the Silver for the wall (without changing any other parameters or dimensions) the cut-off frequency of the structure is no longer at the desired wavelength, as shown in Fig. 11 (a). In this simulation, we have used the permittivity of silver using the Drude model with plasma frequency $\omega_p = 1.37 \times 10^{16}$ rad/s and collision frequency $\omega_c = 8.5 \times 10^{13}$ rad/s [56]. Instead, we observe that the wavelength of maximum transmission is red-shifted to a longer wavelength (which is denoted as "Unscaled" in Fig. 11 (a). As depicted in Fig. 11 (b), for this case the transmission at the original operating wavelength of $1.5\mu m$ is quite low. Moreover, the phase across the intended EMNZ region is no longer uniform as desired as shown in Fig. 11 (c). This is

due to the fact that using Silver rather than PEC (and without changing anything else) a new cutoff condition for the waveguide is obtained. So if we keep the dimensions of the waveguide as the ones for the PEC case, it is evident that we will not get the desired EMNZ properties. However, for the section of interest to operate as the EMNZ, one needs to ensure that the host waveguide behaves as an ENZ structure, i.e., the waveguide in this section should operate near its new cut-off frequency. Therefore, we need to re-scale the separation between the upper and lower walls of the waveguide in order to take into account the change in the cutoff conditions, and thus bring the wavelength at which the new structure with lossy walls behaves as EMNZ back to the intended $1.5\mu m$ with acceptable transmission and uniform phase across the structure. This is denoted as the blue curve labeled "Scaled" in Fig. 11 (a). As shown in Fig. 11 (e) and (f), our simulations now show that the high transmission (albeit less than unity due to the increase of S11 (owing to now the impedance mismatch) and the wall losses) with the uniform phase within the EMNZ region can indeed now be achieved at $1.5\mu m$ even with the Silver walls.

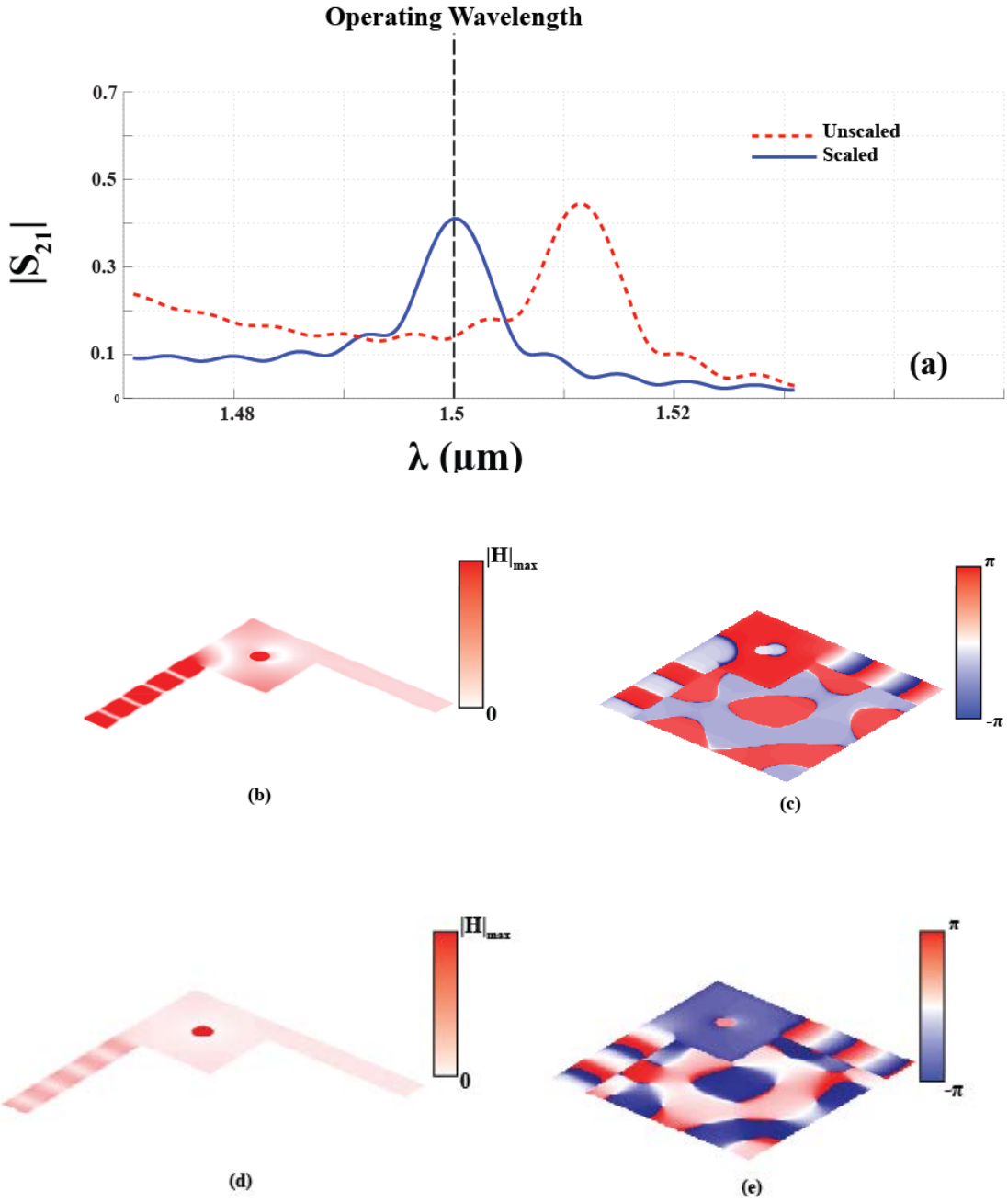

Fig. 11 Investigating the EMNZ behavior of the proposed structure when using silver walls instead of PEC *(a) Magnitude of the transmission coefficient (S_{21}) of a structure*

similar to the one shown in Fig. 9, but using Silver walls instead of PEC, using the same waveguide dimensions as in the design for the PEC case (red dashed curve labeled "Unscaled") and with the change in the dimension to take into account the shift in the waveguide cut-off frequency (i.e., ENZ frequency) and consequently adjusting its dimensions to bring the cut-off (ENZ) frequency back in order to coincide with the original operating frequency (blue solid curve labeled "Scaled". (b) Amplitude and (c) Phase of the magnetic field in the middle plane within the structure when illuminated by a wave coming from one of the ports when not taking into account the effect of the shift in the cutoff (ENZ) condition. (d) and (e) Same as (b) and (c) but taking into account the effect of the cutoff (ENZ) shift and adjusting the dimensions. We clearly see that our simulations in (d) and (e) show the uniform phase and relative high transmission even with the presence of the lossy walls.

2.8 Two-dimensional (2D) photonic crystal (PC) replacing PEC walls for operation at the optical domain

Photonic crystals have been a research topic of interest for several decades [57–66]. It is well known that a photonic crystal with a complete bandgap would not allow propagation of electromagnetic waves with frequency within that bandgap. However if one creates proper defects into the photonic crystals light can be guided in such defects [67,68]. In this section we show the possibility of using 2D PC with a complete photonic band gap as a background host within which our proposed ideas for EMNZ media can be considered without a need for PEC walls. This will provide exciting possibility for further

research into other interesting aspects of the EMNZ structure in the optical domain offering a platform within which EMNZ structures can be constructed and characterized.

To illustrate this point, here we utilize one of the available designs in the literature for the 2D PC with the bandgap (e.g., the design described in Professor Shanhui Fan's work in Ref [69]). In this design a 2D PC is constituted with a triangular lattice of air holes in a host medium of $\varepsilon_r = 6.25$. The air holes in [69] have a radius of 0.35 a, where *a* is the lattice constant at an operating frequency $\omega = 0.3468(c/a)$. To make the design in [69] suitable for our problem, each waveguide (input and output for our problem) is obtained by carving rectangular air region as shown in Fig. 12 (a). We then consider an EMNZ region between the two such waveguides within the 2D PC environment. As shown in Fig. 12 (b) and (c) our numerical simulation shows that we obtain almost perfect transmission between the two ports with almost uniform phase within the EMNZ region. Now if instead of using a hypothetical EMNZ medium, we use a host medium that is ENZ and load it with the properly designed dielectric rod to achieve the MNZ condition, we still get almost perfect transmission with almost uniform phase within the proposed EMNZ region as shown in Fig. 12 (d) and (e). Moreover, the performance is insensitive to the rod's location as expected from our analysis, owing to the ENZ nature of the host medium. As depicted in Fig. 12 (f) and (g) even moving the rod to the corner of the structure (but not too close to touch the wall) we still preserve the same performance. This numerical example shows that it is indeed possible to replace the PEC wall with such 2D PC. (Of course, there are certain special features and limitations associated with

use of 2D PC waveguides different from those of the PEC-wall waveguides, which need further investigation. This will be the subject of future study.

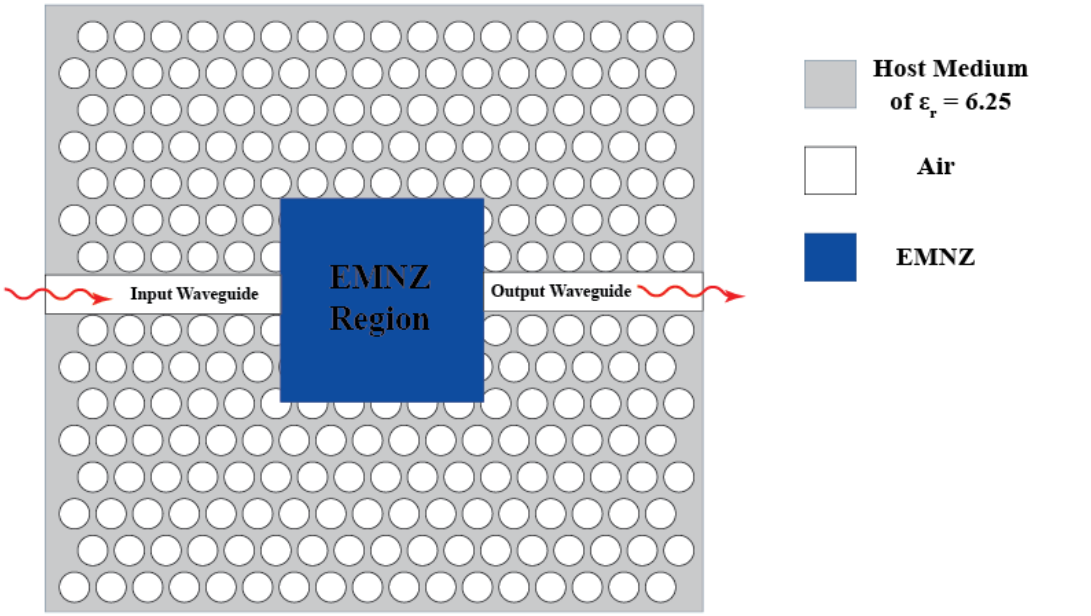

(a)

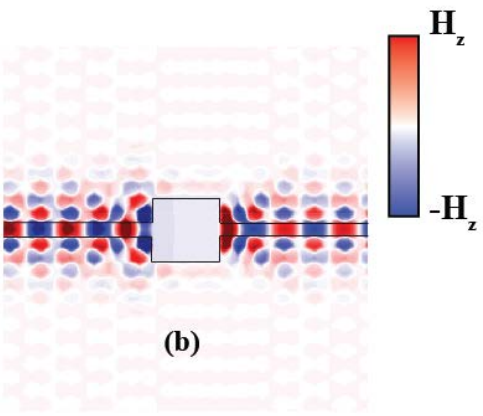

(b)

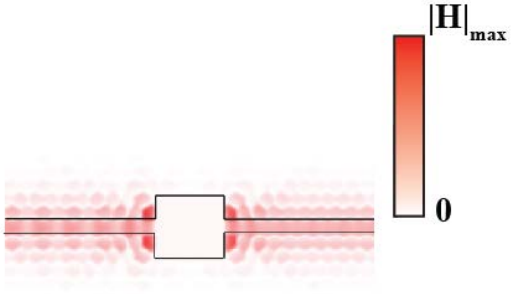

(c)

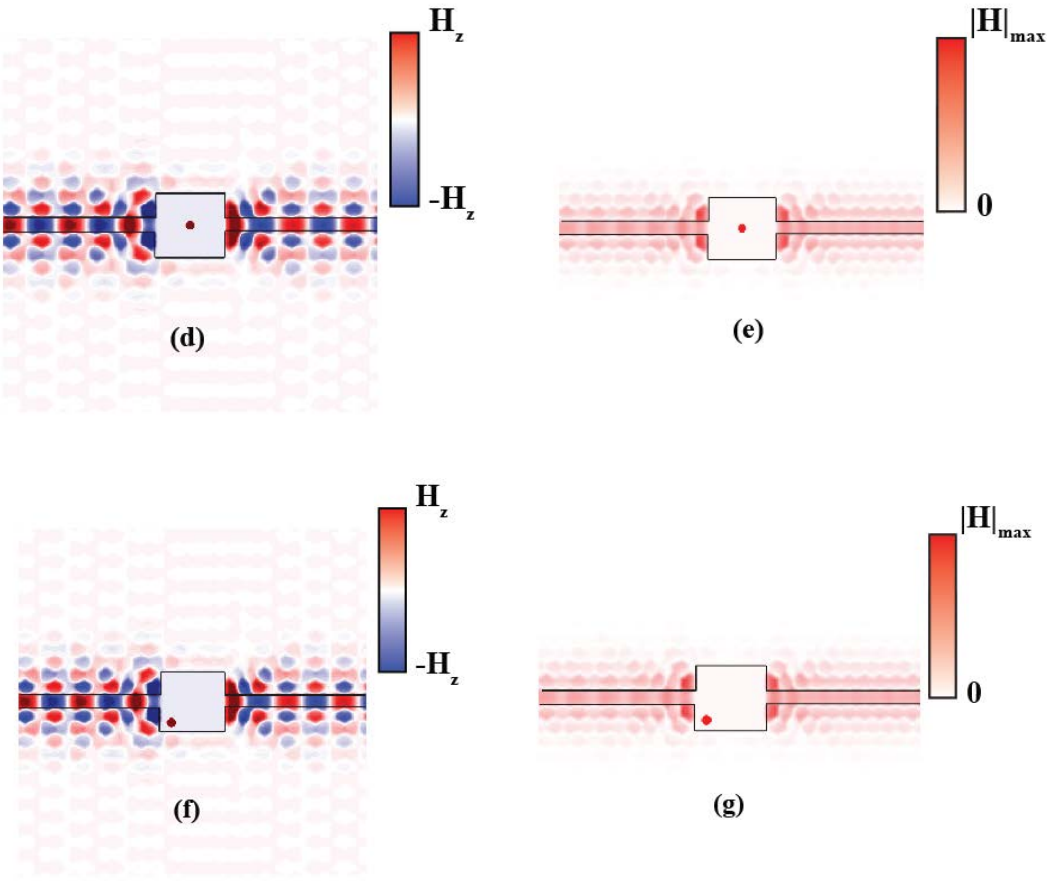

Fig. 12 Proposed design for EMNZ structure within photonic crystal environment using SiC as an ENZ host medium *(a) Schematic of the proposed structure where within a two dimensional photonic crystal an input air waveguide is carved that feeds an EMNZ region that in turn feeds an output air waveguide, the two dimensional photonic crystal replaces PEC walls in our originally proposed structure in the dissertation. The transverse magnetic mode is excited in this 2D structure. (b) Snapshot of the z-component of the magnetic field and (c) Amplitude of the total magnetic field distribution for the case when the EMNZ region is formed using a hypothetical medium whose constitutive parameters are both near zero. (d) and (e) as in (b) and (c) respectively but*

the EMNZ region is designed to consist of an ENZ host medium (a Drude-like medium near its plasma frequency) loaded with a properly designed dielectric rod at the center to force the MNZ condition as well. (f) and (g) as in (d) and (e), respectively, but the same rod is moved to the corner of the structure showing insensitivity of the performance to the rod's location as expected.

2.9 Experimental verification of EMNZ behavior

The main aim of this section is to experimentally demonstrate EMNZ behavior using the proposed structure. However, before we describe our experimental proof-of-the-concept for the EMNZ structure in this section, we first mention how we can avoid the mode coupling. In the proposed 3D structure, moving the rod from the center to the corner of the structure may lead to a slight shift for the EMNZ frequency. This is owing to the fact, that within this structure, due to being bounded with PEC walls along the direction of the magnetic field within the EMNZ region, there exists mode coupling from the desired TE mode to the undesired TM mode which is not accounted for while designing the EMNZ structure. This is depicted in Fig. 13(a) and (b) showing the magnitude of the electric field component normal to the PEC ceiling (E_z) at the ceiling's plane for the two cases of the rod at the center and at the corner, respectively. As we move the rod from the center to the corner we start to get a non-zero E_z component showing that some coupling from the desired TE to the undesired TM mode takes place. Fig. 13(c) shows that the frequency at which the EMNZ condition is achieved consequently exhibits a slight shift.

To avoid this coupling, we utilized the method that was suggested in the paradigm of waveguide metamaterials and waveguide metatronics described in Ref [70,71]. Following this method, we surround the perimeter of the dielectric rod with 8 thin PEC wires to prevent the excitation of the TM mode in the vicinity of the rod as shown in Fig. 13(d) and (e). Doing so, as shown in Fig. 13(d) and (e) we have zero E_z component regardless of the location of the rod. Consequently the frequency at which the structure exhibits the EMNZ behavior remains fixed regardless of the rod's location as shown in Fig. 13 (f).

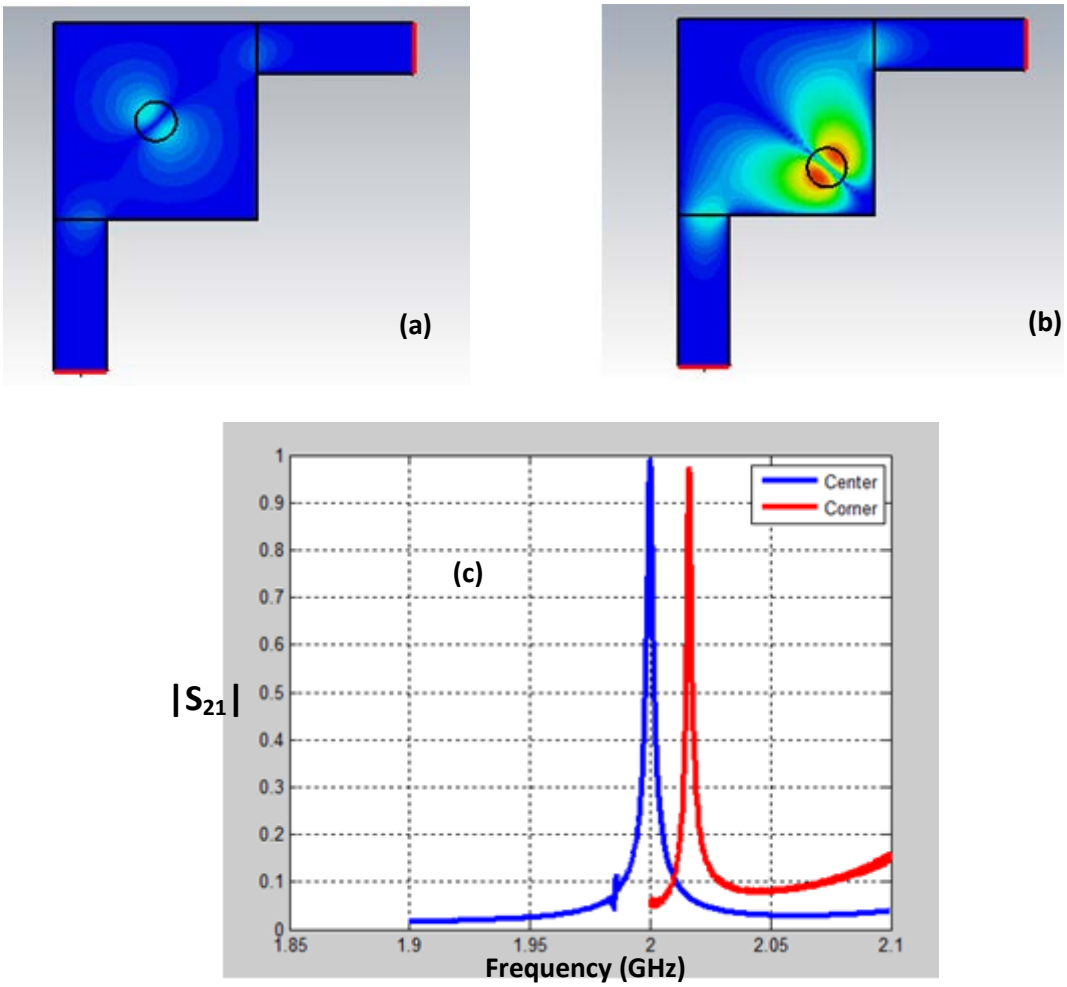

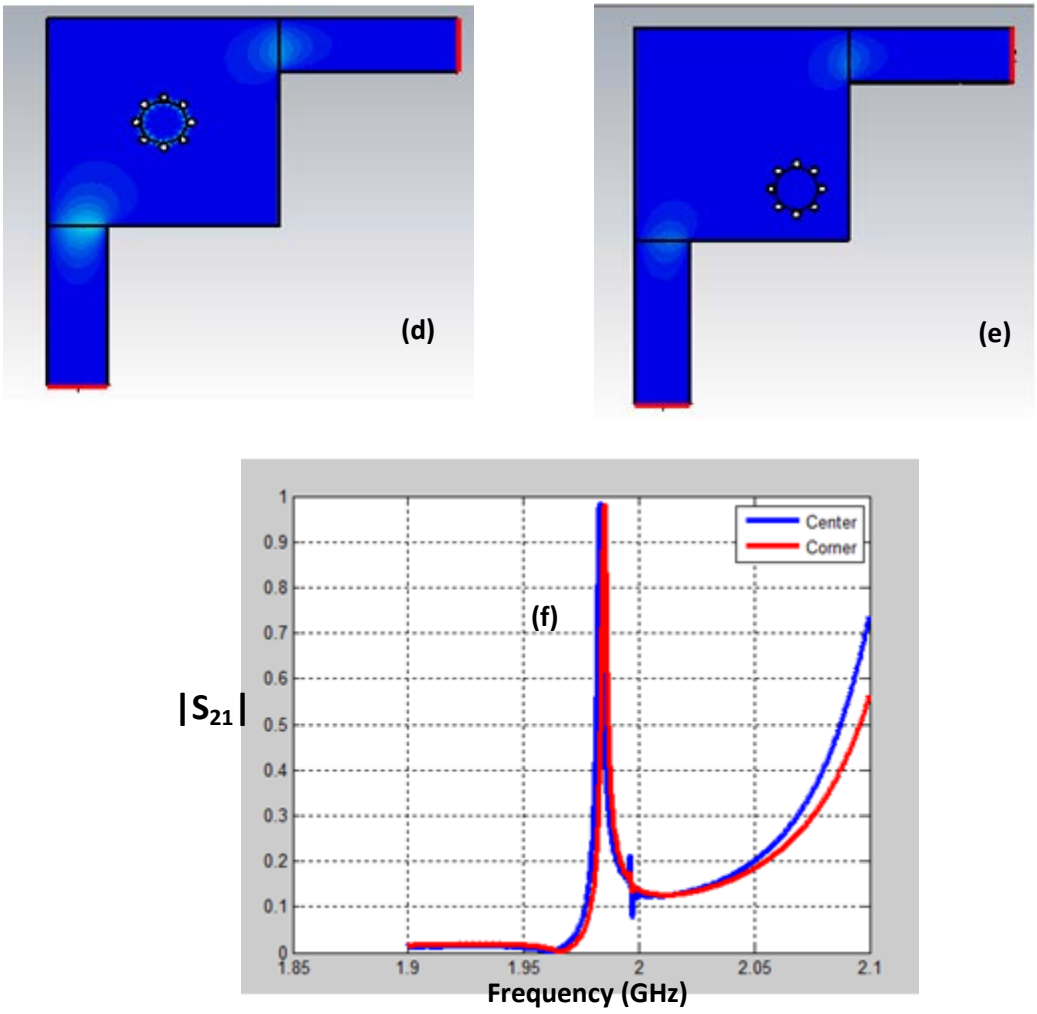

Fig. 13 Sensitivity of EMNZ behavior in 3D to dielectric rod location and mitigating it by putting thin wires around the dielectric rod*, (a), (b) of the magnitude of the electric field component normal to the ceiling (E_z) at the ceiling's plane for the two cases of the rod at the center and at the corner respectively. (c) Magnitude of the transmission coefficient (S_{21}) with the rod at the center (red curve) and at the corner (blue). (d), (e), and (f) similar to (a), (b), and (c) except the presence of metallic wires surrounding the dielectric rod to prevent TE to RM mode coupling*

As discussed earlier in this chapter, for a fixed surface area of the EMNZ section, regardless of the shape of the section and the location of the dielectric rod, its performance should be preserved. The experiment is designed to show our proposed structure behaves as EMNZ medium regardless of how arbitrary is the shape or the location of the dielectric rod. We start by designing our EMNZ structure to have a cross section area of $1.37\lambda_0 \times 1.37\lambda_0$. Following the previously shown analysis, in order to achieve the EMNZ condition we need a dielectric rod of radius $0.137\lambda_0$ and relative permittivity of 9. We would also need the input and output waveguides to have the dimensions $\frac{\lambda_0}{2} \times \frac{\lambda_0}{3}$ and be filled with dielectric of relative permittivity of 2. We choose our design frequency to be 2.376 GHz. At this frequency range, the dielectric rod can be implemented by filling a plastic tube with the commercially available powder from Emerson & Cuming under the set of materials labelled "ECCOSTOCK HiK500F". As for the input and output waveguides, having Teflon block with the proper dimensions wrapped in copper shape does the job. For this fixed cross-sectional area we design three arbitrary shapes as shown in Fig. 14 (a)-(c). For each of these shapes we choose three arbitrary locations for the rod.

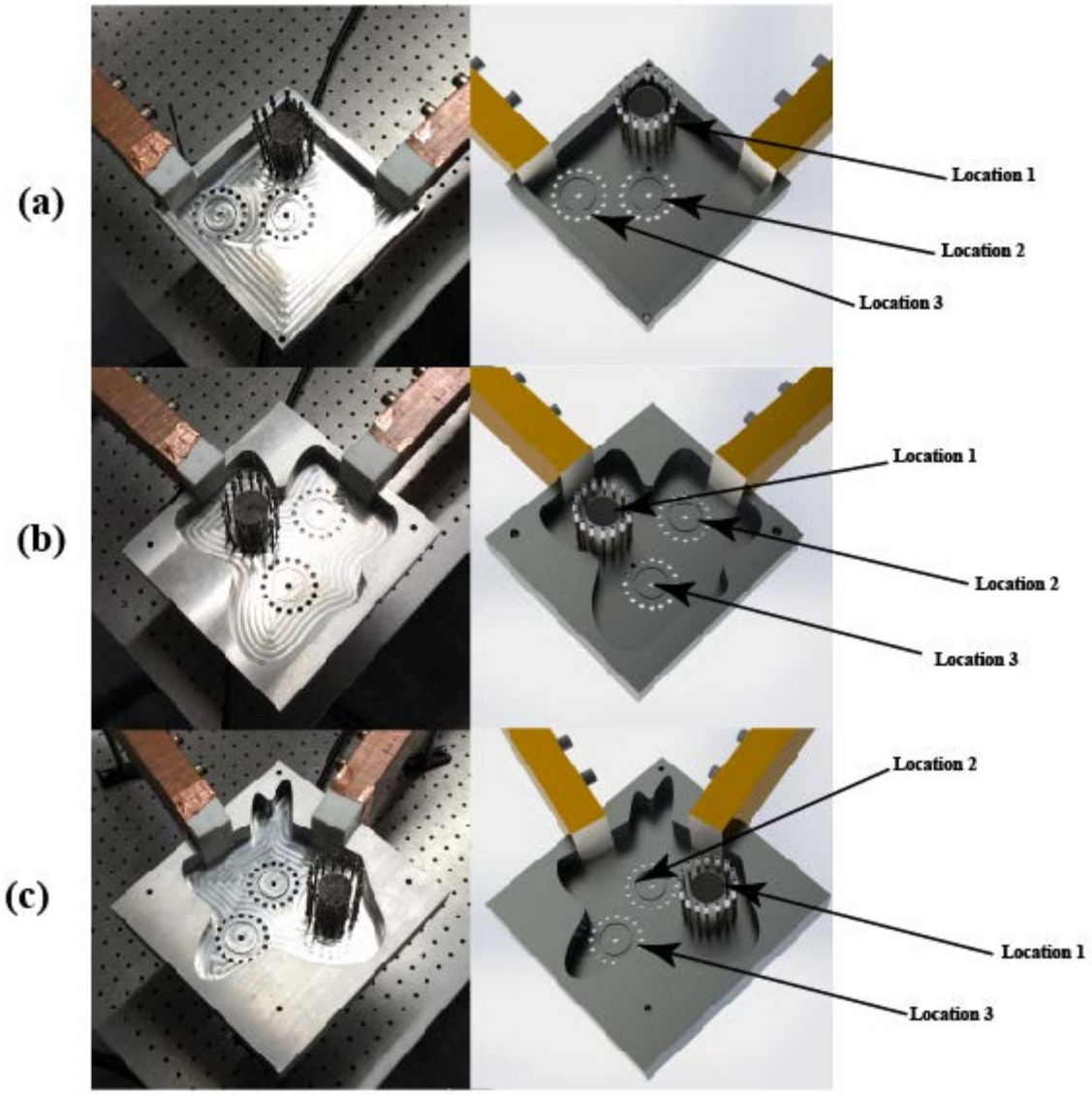

Fig. 14 Proposed concept for the experiment to verify EMNZ behavior*: Schematics of our three different arbitrary shaped EMNZ structures with three different locations of the dielectric rod. In all cases the EMNZ performance of opening up the space is preserved. (a) EMNZ structure of a square cross section connecting two waveguides, (b) Same as (a) but with an arbitrary-shaped cross section, (c) same as (b) but with the input and output ports arbitrary placed.*

There exists two main challenges in this experiment. The first technical challenge was to use some sort of a deembedding technique to extract the S-parameters for our measured sample. The lack of good perfect wideband absorbers for the Teflon filled waveguides that serve as our input and output ports prevents us from fully characterizing our sample by a single measurement using conventional network analyzer as would be the case if the input and output waveguides were air-filled (for which perfect wideband absorbers are readily available), as in most microwave experiments. To overcome this problem we characterize our samples by taking two sets of linearly independent measurements and using the proper deembeding from Ref [66] we extract the S-parameters for our samples. More details regarding this technique can be found in [72] . On the other hand, as discussed above, the dielectric rod has to be surrounded by metallic wires to prevent the undesired coupling from TE to TM mode. For this purpose, we choose 16 wires, each of 1/8" thickness. A big challenge in this design is to make good electrical connects between the wire and the floor and ceiling of the waveguide. This is addressed in the next section.

2.10 Good Electrical Contacts

We achieve this good electrical connection through the use of collets driven into the base (the floor and ceiling of the waveguides) by a set of screws as shown in Fig. 15. We find that making the base thick enough to accommodate the set of screws and collets length may drive up the cost. Therefore, we choose to fabricate the base and a "clamp" which affixes to the base to hold the set of screws as shown in Fig. 15. The designs

themselves were outsourced and developed using emachineshop CAD tools and fabricated at their workshop (http://www.emachineshop.com/machine-shop/Free-CAD-Design-Software/page100.html).

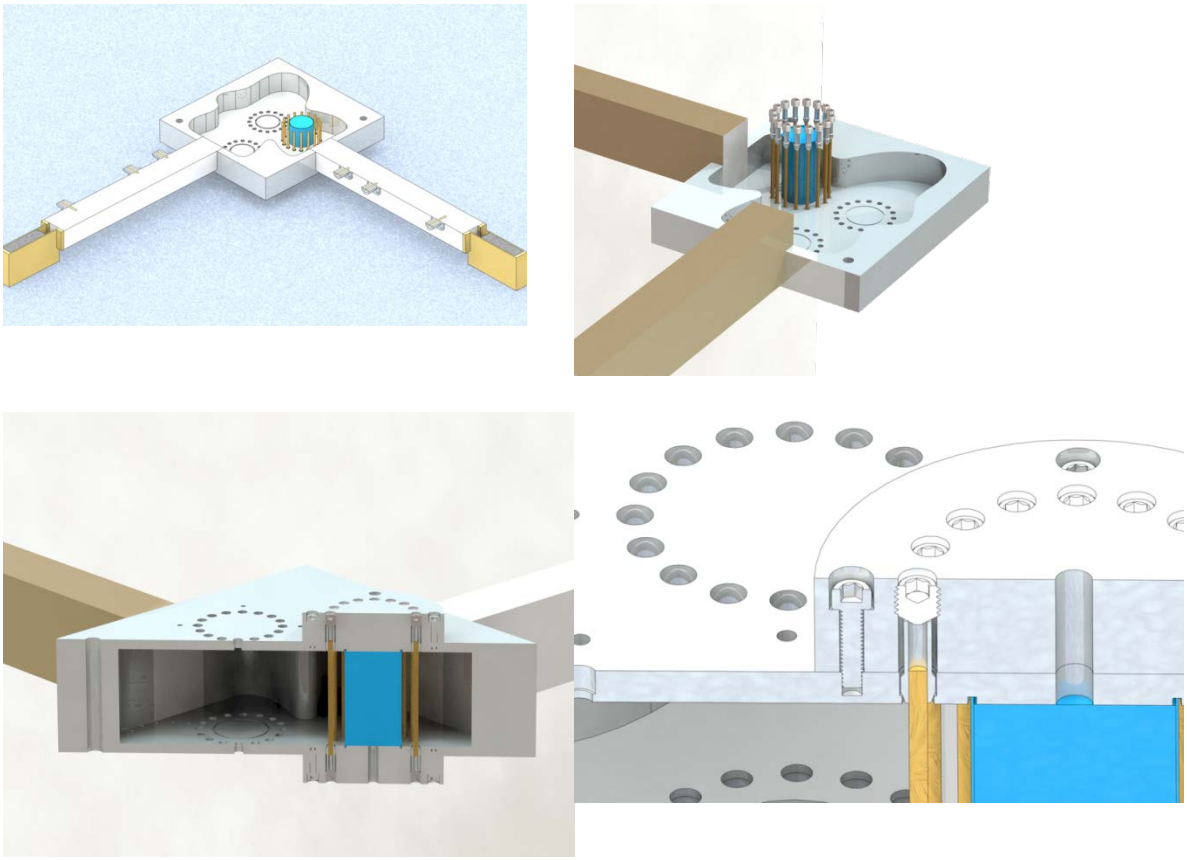

Fig. 15 Schematics showing the technique using collets to guarantee good electrical contacts

The key parameters in our design are listed as follows:

- Collet: Widget Supply Company D-ED16 (https://www.widgetsupply.com/product/D-ED16.html). Originally designed to hold 1/8” shaft dremel tool bits in a Dremel tool. By measuring it with the digital calipers and visual inspection the stock photo, the measurements are determined.
- Attachment Screws: MMC 92185A196 - 8-32 5/8=0.625” socket head cap screw. Head diameter 0.27”
- Push Screw: MMC 92694A420 5/16-24 5/16=0.313” High Hold Cone Point Set Screw.

Wire Clamping

- The 16 collet holes drilled to a depth of 0.187” at 0.250” diameter
- The remaining 0.063” of depth should be #12 = 0.216” diameter
- These holes are spaced equally around a circle with a diameter of 53.60mm = 2.110”

Clamp

- 16 collet holes threaded with 5/16-26
- 4 holes drilled to #18 = 0.170”, counter sunk with ~0.30” to a depth of 0.250”.
- The total thickness of the clamp is 0.75”

Clamp Mounting

- The 4 mounting holes are blind threaded holes down to a depth of 0.1875 = 3/16” with the 8-32 thread.
- These are equally spaced on a circle of 3” diameter

Tube sealing

- There is a ring milled down into the resonator to a depth depth 1.5mm
- Inside diameter 33.60mm
- Outside diameter of 36.60

General

- The surface area of the cavity is 172.72mm 172.72mm = 29832.20 mm^2 = 46.24 in^2
- The waveguide width is 42.09 mm
- The waveguide height is 63.13 mm
- All bases have a floor thickness of 0.250”
- The wall half-height off of the floor is 1.243”
- The waveguide penetration depth is 0.5”. The penetration depth is the distance shown in the top left panel of Fig. 16 as the uncovered Teflon, it is the clearance that we use to fit the Teflon waveguide into our arbitrary air filled waveguides, then after being covered with the ceiling it works as a Teflon waveguide

2.11 Experimental Results

The different cavities are fabricated at the emachineshop workshop and the experimental setup is constructed as shown in fig. 16. Measurements are taken for the three different cavities and three different rod locations in each cavity.

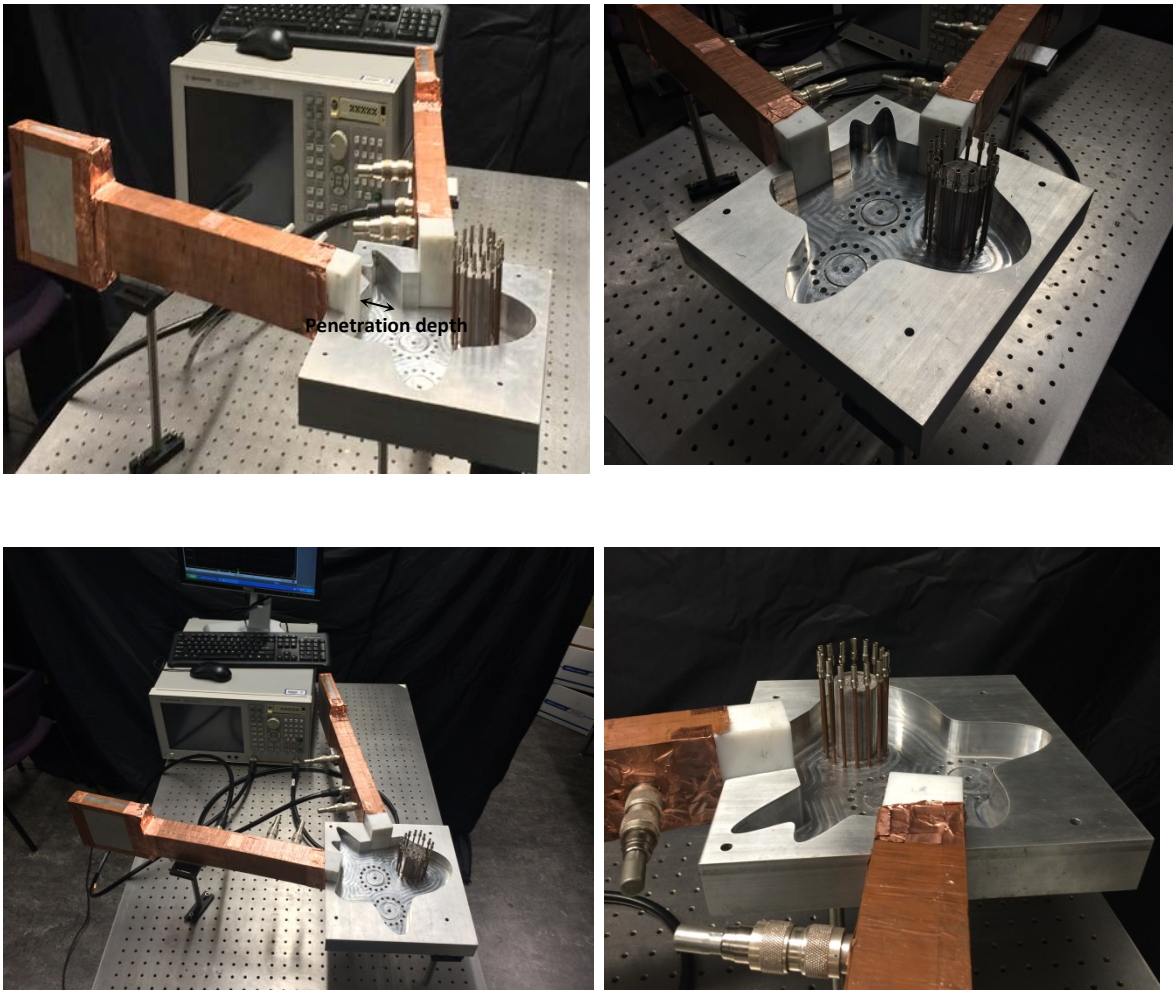

Fig. 16 Photographs of the experimental setup

After applying the deembeding technique [72] the experimental results are obtained as shown in Fig. 17. These results are compared with the simulation results and are found to be in good agreement with our predictions. At the EMNZ we have a pick in the transmission coefficient that does not change with the shape of the EMNZ cavity or with the rod's location as shown in Fig. 17 (a) and (b). At this EMNZ frequency the phase of the transmission coefficient is pinned to zero as shown in Fig. 17 (c) and (d), verifying the EMNZ property of opening up the space experimentally.

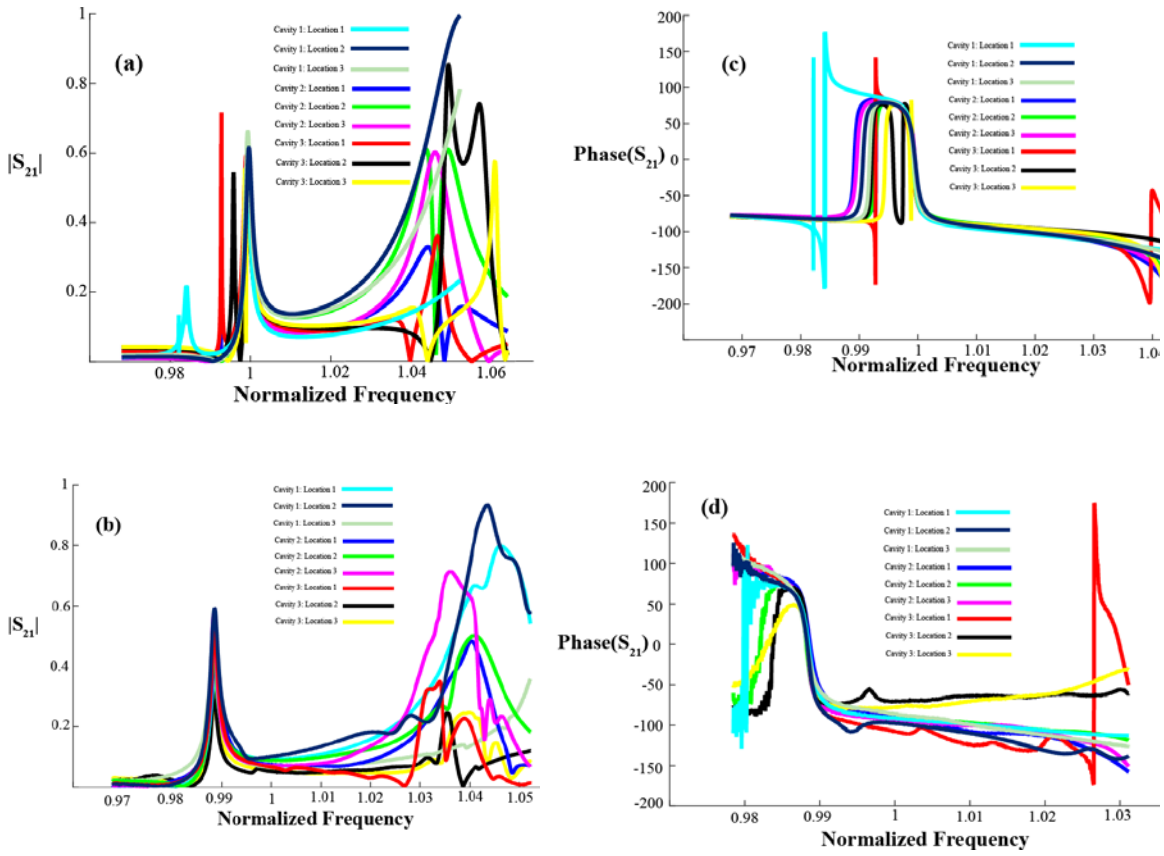

Fig. 17 Numerical and experimental results, *(a), (b) Numerical and experimental*

results for the magnitude of the transmission coefficient (S_{21}) for the three structures and the three rod locations per each, respectively. (c) and (d) Same as (a) and (b) but for the phase of the transmission coefficient (S_{21})

There is a slight red shift as shown to be around 0.989 instead of 1. This shift can be due to one or both of the following reasons

- The powder has epsilon that is not exactly 9 as designed; it can be slightly higher which would move the resonance to a slightly lower frequency.
- The plastic tube that is holding the powder has Epsilon that is not 1 as we assume in the simulations.

I would like to thank Dr. Brian Edwards for his input throughout the process of designing, building and measuring this setup.

The field of metamaterials has recently evolved to cover other various aspects of physics including quantum effects. Merging metamaterials with quantum sources and small optical emitters has recently attracted significant research efforts. For example it was discussed how near zero constitutive parameters, compared to those available in nature can offer an interesting paradigm for tailoring quantum emission properties of small sources [4,54,73–75]. Epsilon near zero (ENZ) metamaterial channels have been proposed to significantly enhance the spontaneous emission rates of quantum emitters owing to the enhanced field intensities within such channels. Moreover, exploiting the nearly uniform phase distribution of that enhanced electric field along the channel was shown to lead to the independence of the emission enhancement on the dipole's location

within the channel [73,74]. The possibility of significantly enhancing the spontaneous emission of a collection of two-level quantum emitters by embedding them in an epsilon-near-zero (ENZ) environment, consisting of a plasmonic waveguide operated at cutoff was also discussed. Furthermore, a hybrid of Purcell enhancement and Dicke superradiance effects [76], exploiting the large and uniform local density of states in ENZ channels [54] was explored. Within the same paradigm, the possibility of observing superradiance and subradiance effects in an ensemble of two level atoms, placed in a waveguide cladding of a zero index metamaterial was also investigated [77]. Moreover, integrating quantum emitters with negative constitutive parameters media has been investigated in various works. For example, it was shown that embedding a two level emitter in a negative permeability slab near the interface with an impedance matched negative permittivity slab leads to extremely high local density of states resulting in strong coupling between the emitter and the surface plasmon and an associated large Rabi frequency and spontaneous emission rate [78]. Within the same track of research, the spontaneous decay and quantum interference of a V-type Zeeman atom placed near a negative permeability slab was also investigated [79]. Based on the fact that the slab supports only TE polarized surface plasmon polariton (SPP) modes, the decay rate of the dipole component parallel to the interface was shown to be much larger than that normal to the interface. Consequently, high-level anisotropic environment can be created and the two dipoles can interfere with each other strongly by sharing such SPP modes even if they are orthogonal [79]. The category of metamaterials labelled as left handed materials (LHM) has also attracted a lot of attention within the field of quantum optics. The

quantum interference between two spontaneous emission transitions which are orthogonal, in a three-level system was shown to be greatly enhanced by using LHM due to the focusing and phase compensation effects [80]. Moreover, quantum interference between Zeeman levels of atom placed in the structure containing LHM's and zero index media (ZIM) was also investigated. Due the existence of the LHM and ZIM, dipole radiation was shown to be highly anisotropic with high contrast between decay rates of the dipole components parallel and normal to the surface. Furthermore, both decay rates were proven to be suppressed compared with those in free vacuum [81]. Within the same framework, it was shown that two emitters placed at the foci of a perfect lens formed by a parallel LHM exhibit perfect superradiance and subradiance over distances that can be orders of magnitude larger than the transition wavelength. Furthermore, complete suppression of spontaneous emission of an atom in front of a mirror with a layer of LHM owing to the negative optical path length in LHM was proposed [82]. Likewise, owing to the ability of such slab to support or prohibit both TE and/ or TM modes under certain conditions, the spontaneous decay rate can be significantly tailored in a different fashion than near a dielectric or a metallic slab. It was also shown that the decay through SPP will be larger than the decay through dissipation when the atom is placed at an appropriate position [83]. Integrating quantum emitters with novel materials such as graphene and topological insulators (TI) has also recently attracted significant research efforts, owing to the rich unconventional physical phenomena that such materials can offer. For example, superradiant and subradiant regimes were investigated both in transmission and reflection configurations in vicinity of two dimensional graphene sheets and one

dimensional ribbons [84]. The length scale of the coupling between emitters which in vacuum is predetermined by the free space wavelength was proven to be determined by the wavelength of the graphene surface plasmons in that case. This can be extremely short and easily tunable via gate voltages [85]. Moreover, the spontaneous emission rates near a topological insulator interface are significantly inhibited in comparison with that near a dielectric interface, especially for parallel dipole [86]. The properties of spontaneous emission of a two-level atom in anisotropic with ellipsoidal or hyperbolic dispersions has also been studied thoroughly in [87].

In this work, we explore the ability of EMNZ structures to introduce a new platform for long range interaction between relatively arbitrarily oriented emitters. First, we investigate the ability of a two dimensional (2D) version of the proposed structure in [4] that mimics EMNZ behavior to preserve such features, and make use of the flexibility of such structure and its robustness towards various aspects, including its shape and the location of the dielectric inclusion placed inside it to propose a rather flexible platform for long range emitters interaction. We also investigate theoretically our proposed concept within the three dimensional (3D) implementation in the microwave range shown in [4], discussing the limitations and proposing recipes for achieving almost perfect correspondence between 2D and 3D scenarios. We finally propose a design platform within which such phenomena can be preserved in an all dielectric two dimensional photonic crystal (2D PC) environment omitting the use of PEC walls and making it more suitable and experimentally feasible in the optical and mid IR domains.

2.12 Collective interaction between two emitters separated EMNZ structure (2D scenario)

Placing emitters inside a waveguide has always offered a platform for long range interaction between them making use of the guided nature of the emitted waves inside the waveguide. Despite the rather straight forward design and implementation, coupling two emitters within a waveguide still suffer from some limitations including dependence of the waveguide's Green's function on the presence of bends and/or scatterers , and the orientation of the emitters with respect to each other within the waveguide. It is of great interest to engineer systems where the interaction between the two emitters being separated by large distances kept the same regardless of the relative orientation of the two emitters. By exploiting the ability of EMNZ media to "open up" and "stretch the space", it is possible to keep the interaction the same between two emitters whose relative orientation is rather arbitrary as it would be in a straight waveguide being oriented in the same direction. This is depicted schematically in Fig. 18(b) where two waveguides are arbitrarily oriented and connected via an EMNZ region. The two emitters are placed within these waveguides (along the direction of the waveguide's electric field) Although the orientation of the two waveguides is arbitrary, the two emitters are still expected to preserve the same interaction as the two emitters shown in Fig. 18(a). As depicted schematically in Fig. 18(a), two emitters with transition frequency ω_0 and of dipole moments d_1 and d_2 placed inside a waveguide, separated by a distance *S* would exhibit collective interaction that can be described in terms of the electric field Green tensor as follows [77].

$$\Gamma_{12} = \frac{2\omega_0}{\hbar\varepsilon_0 c^2} d_1 \,\mathrm{Im}\{G(\bar{r}_i, \bar{r}_j, \omega_0)\} d_2$$

$$\Omega_{12} = \frac{\omega_0^{\,2}}{\hbar\varepsilon_0 c^2} d_1 \,\mathrm{Re}\{G(\bar{r}_i, \bar{r}_j, \omega_0)\} d_2$$

Where, Γ_{12} is the coupling coefficient that describes the radiative decay of atoms, Ω_{12} is the coupling coefficients that describe the frequency shift of atomic transitions due to dipole-dipole interaction.

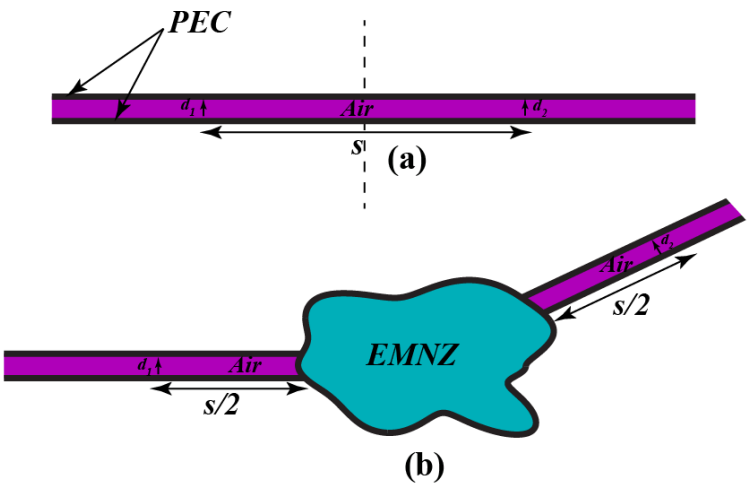

Fig. 18 ***Schematic of epsilon-and-mu-near-zero (EMNZ) opening up the space in a parallel plate waveguide****, (a), (b) Schematic of an EMNZ medium emulating opening up or stretching the space at the dotted line between the two sections of an air-filled 2D parallel-plate waveguide, while keeping the region as a "single point" electromagnetically. This keeps the interaction between two 2D emitters placed in the two sections of the waveguide the same as for a straight waveguide*

regardless from their relative orientation.

As we described in an earlier chapter, using a host medium that has a near zero permittivity (ENZ) and loading it with a properly designed dielectric rod we can achieve an effectively EMNZ medium. It was also discussed that owing to the ENZ nature of the host medium that the shape of the EMNZ structure as well as the location of the rod within the structure does not influence the EMNZ behavior, and that for a fixed area and dielectric rod properties (its radius and relative permittivity), the performance would be preserved regardless of how arbitrary the shape of the region is or the location of the rod is within the structure. Thus, the performance depicted schematically in Fig. 18 can be achieved using the structure shown in Fig. 19 (a) where an arbitrarily shaped ENZ region of a surface area $1.37\lambda_0 \times 1.37\lambda_0$ (where λ_0 is the free space wavelength) is loaded by a dielectric rod of radius $0.137\lambda_0$ and relative permittivity of 8. According to [4], such structure exhibits an EMNZ behavior at the operating frequency. This arbitrary region is in turn connected to two 2D parallel-plate waveguides that are also arbitrary oriented with respect to each other. The external boundary of the entire region shown in Fig. 19 (except for the input and output exit ports) is PEC wall. One 2D emitter is placed inside each 2D waveguide at distance $S/2$ from the interface between the waveguide and the EMNZ region. The 2D emitters are oriented such that they lie in the transverse plane to the direction of the waveguide along the direction of the electric field of the TEM mode supported by the waveguide. One of the waveguides (WG1) has a fixed orientation as shown in Fig 2, and the other waveguide (WG2) is rotated along the perimeter of the arbitrarily shaped EMNZ region in each of the three cases. For each of WG2's locations

along the perimeter of each of the structures we evaluate the quantities Γ_{12}^{EMNZ} and Ω_{12}^{EMNZ} by numerically calculating the fields in the structure and consequently evaluating the electric field Green tensor. To quantify the deviation of those quantities from their values for the case of two emitters separated by distance S in a single straight waveguide having the same orientation we define the quantities $\Delta\Gamma_{12}$ and $\Delta\Omega_{12}$ as follows

$$\Delta\Gamma_{12} = \frac{\Gamma_{12}^{EMNZ} - \Gamma_{12}^{0}}{\Gamma_{12}^{0}}$$

$$\Delta\Omega_{12} = \frac{\Omega_{12}^{EMNZ} - \Omega_{12}^{0}}{\Omega_{12}^{0}}$$

Where, Γ_{12}^{0} and Ω_{12}^{0} are the coupling coefficients that describe the radiative decay of atoms and the coupling coefficients that describe the frequency shift of atomic transitions due to dipole–dipole interaction between two emitters similarly oriented and separated by a distance S in a straight waveguide. The dielectric rod is then moved within the structure and at every location the fields within the structure is numerically calculated and consequently the electric field Green electric is evaluated. A color-map for $\Delta\Gamma_{12}$ and $\Delta\Omega_{12}$ are generated versus the location of the rod's center *C* within the EMNZ region. As depicted in Fig 19 (b) and (c), $\Delta\Gamma_{12}$ and $\Delta\Omega_{12}$ are almost zero everywhere showing that our proposed structure indeed acquires the phenomenon discussed for coupling nonparallel emitters over large distance regardless from the shape of the structure as well as the location of the rod within it.

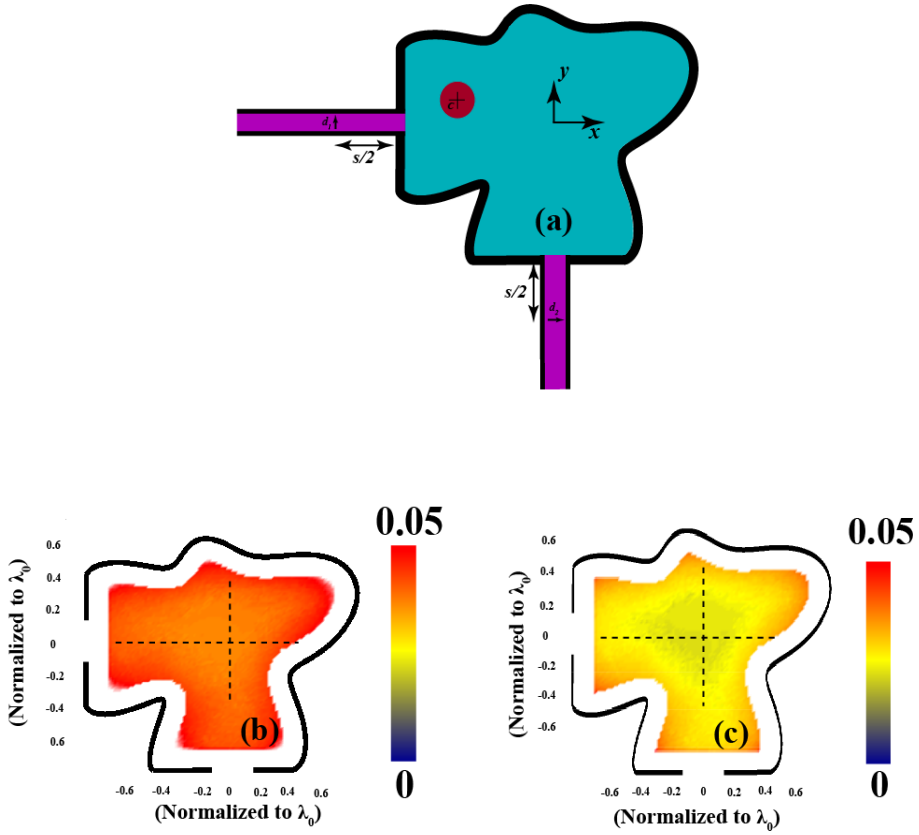

Fig. 19 Investigating the dependence of the interaction between two emitters separated by an arbitrary EMNZ structure on the location of the dielectric rod in a 2D scenario, *(a) Schematic of proposed implementation an epsilon-and-mu-near-zero (EMNZ) medium emulating opening up or stretching the space by being embedded between two air filled waveguide. (b), (c) Colormap of* $\Delta\Gamma_{12}$, $\Delta\Omega_{12}$ *as a function of the location of the center of the rod C within the proposed EMNZ region. The interaction between two 2D emitters placed in the two sections of the waveguide the same as for a straight 2D parallel-plate waveguide regardless of*

their relative orientation and the location of the rod.

2.13 Collective interaction between two emitters separated EMNZ structure in the microwave regime

We also explore theoretically this coupling features in our propsed set-up for the microwave regime. In this section we investigate the ability of that structure to exhibit the phenomenon of long range interaction between arbitrarily oriented emitters in a similar manner to the previously discussed 2D scenario. The proposed structure is as shown in Fig. 20(a), where the two waveguides that are required to emulate an air-filled parallel plate waveguide with the TEM mode are mimicked using TE_{10} mode in rectangular waveguides filled with a dielectric of relative permittivity of 2. The EMNZ section is formed of an air-filled waveguide of a surface area $1.5\lambda_0 \times 1.5\lambda_0$ (where λ_0 is the free space wavelength) loaded by a dielectric rod of radius $0.1\lambda_0$ and relative permittivity of about 15.74. Two scenarios are then considered to investigate the ability of such structure to mimic the emitter coupling features discussed above. The dielectric rod is placed at two locations within the proposed EMNZ section, at the center and at one of its corners. For each of the two cases, $\Delta\Gamma_{12}$ and $\Delta\Omega_{12}$ are evaluated in a similar fashion mentioned above. Unlike the 2D implementation discussed before as shown in Fig. 20(b) and (c), the performance of the structure shows not to be as robust to the rod location within the EMNZ region. Moving the rod from the center to the corner of the structure leads to a non-zero $\Delta\Gamma_{12}$ and $\Delta\Omega_{12}$. This is owing to the fact, that within this structure, due to being

bounded with PEC walls along the direction of the magnetic field within the EMNZ region, there exists mode coupling from the desired TE mode into an undesired TM mode as mentioned before. To avoid such coupling, as we discussed before in our simulations, we surround the perimeter of the dielectric rod with 8 thin PEC wires to prevent the mode coupling from TE to TM. Adding the PEC wires, as depicted in Fig. 20 (b) and (c) retrieves the structure's robustness to the location of the rod, with $\Delta\Gamma_{12}$ and $\Delta\Omega_{12}$ being almost zero at the operating frequency for both cases, when the rod is placed at the center and at the corner.

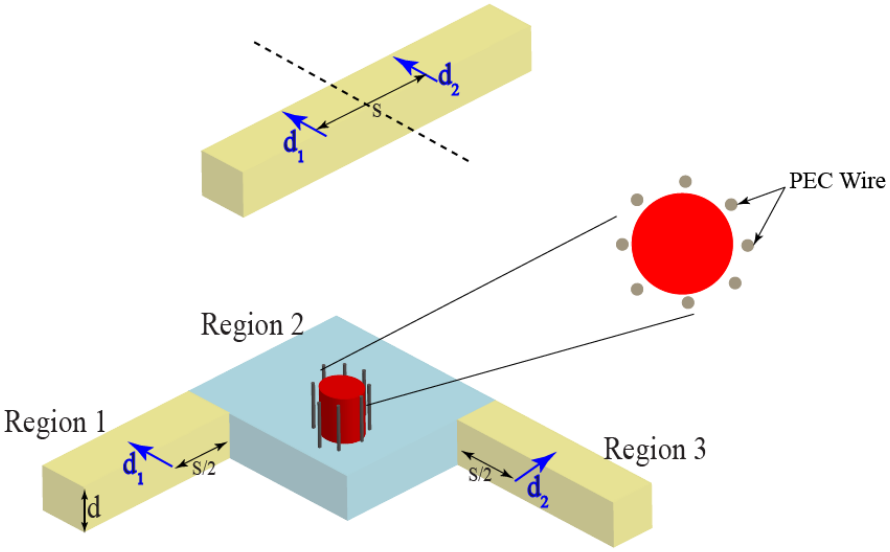

(a)

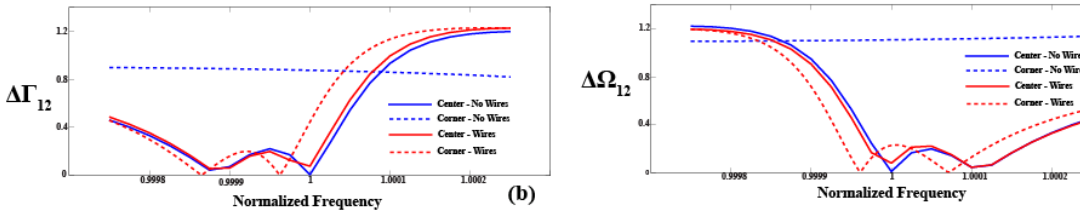

(b)

Fig. 20 Investigating the dependence of the interaction between two emitters separated by an arbitrary EMNZ structure on the location of the dielectric rod in a 3D scenario*, (a) Schematic of an EMNZ structure similar to what we discussed earlier, but now with two electric 3D dipoles at the two waveguide ports. This keeps the interaction between two emitters placed in the two sections of the waveguide the same as for a straight waveguide regardless of their relative orientation. PEC wires are added around the dielectric rod to prevent TM to TE mode coupling and preserve the insensitivity of the performance to the location of the rod within the structure. (b), (c)* $\Delta\Gamma_{12}$, $\Delta\Omega_{12}$ *as a function of normalized frequency. Addition of PEC wires around the dielectric rod omits the dependence of the performance on the location of the rod within the structure*

2.14 Collective interaction between two emitters separated EMNZ structure in the optical regime

Finally, in this section we theoretically investigate the possibility of applying our concept of coupling two emitters over large distances within an all dielectric photonic crystal environment omitting the use of PEC as boundaries for our structure and opening the door to applying our concept in the optical and near IR domains. In [6], Chan and his group established the conditions for realizing Dirac cones at k=0 in 2D PCs, and verified by numerical simulations and through experiments that an effective medium theory can indeed link such 'Dirac cone at k = 0' PCs with reasonable dielectric constants to a system with effective index near zero, and that purely dielectric PCs can behave as if they

acquire near zero constitutive parameters for the TE mode (whose Electric field is along the axis of the PC) [45]. In this section we show the possibility of using 2D PC with a complete photonic band gap as a background host within which our proposed ideas for EMNZ media can be considered without a need for PEC walls or inherently ENZ media. Combining such PC "walls" with the proposed 'Dirac cone at k = 0' PCs [6], we are able to propose an all dielectric platform within which our concept can be applied in the optical domain and mid IR domains. The proposed structure is shown in Fig. 21 (a). Region 1 is a 2D PC with a complete bandgap at the operation frequency constituted with a square lattice of silicon pillars of a lattice constant $a_1 = 0.28\lambda_0$, radius $r_1 = 0.0846\lambda_0$ and $\varepsilon_r = 12.5$ in a host medium that is air, where λ_0 is the operating wavelength. Each of the two waveguides (Regions 2 and 3) are obtained by removing one raw of pillars from the PC and creating a defect waveguide. We then consider an 'Dirac cone at k = 0' PCs region between the two waveguides within the 2D PC environment that is designed using the design flow proposed in [6] for achieving the zero index condition in a PC. The host medium is kept the same as in region 1 and the 'Dirac cone at k = 0' medium is also formed using a square lattice of silicon pillars of a lattice constant $a_2 = 0.56\lambda_0$, radius $r_2 = 0.112\lambda_0$. The 'Dirac cone at k = 0' region has an area of $6.16\lambda_0 \times 6.16\lambda_0$. Fig. 21 (b) shows the bandstructure of both the complete bandgap PC (shown as blue dots) and the 'Dirac cone at k = 0' PC (shown as red dots). The dotted horizontal line shows the operation frequency. As depicted, at the operation frequency Region 1 indeed exhibits a complete bandgap behavior, while Region 4 exhibits a Dirac cone with accidental degeneracy that leads to EMNZ performance. Worth mentioning here that we design the

system to work at slightly higher frequency than the exact Dirac cone point as shown in Fig. 21(b) to avoid exciting the longitudinal mode by the higher order K- vector components appearing at the interface of the waveguides and the 'Dirac cone at k = 0' PC.

We then place a y-oriented 2D magnetic dipole within the first waveguide (Region 2). Fig. 21 (c), (d), and (e) shows snapshots of the electric field for three different cases: a straight waveguide, 90^o bent waveguide, and 180^o bent waveguide respectively, while Fig. 21(f), (g), and (h) shows the phase of the electric field within the structure. As shown from our simulation, regardless of the orientation of the output waveguide (Region 3), the emitted fields from the dipole traverse the 'Dirac cone at k = 0' PC with almost no reflection and no phase progression. This verifies the possibility of applying our concept of long-range interaction between the two emitters, for having a rather flexible platform with an all-dielectric PC environment.

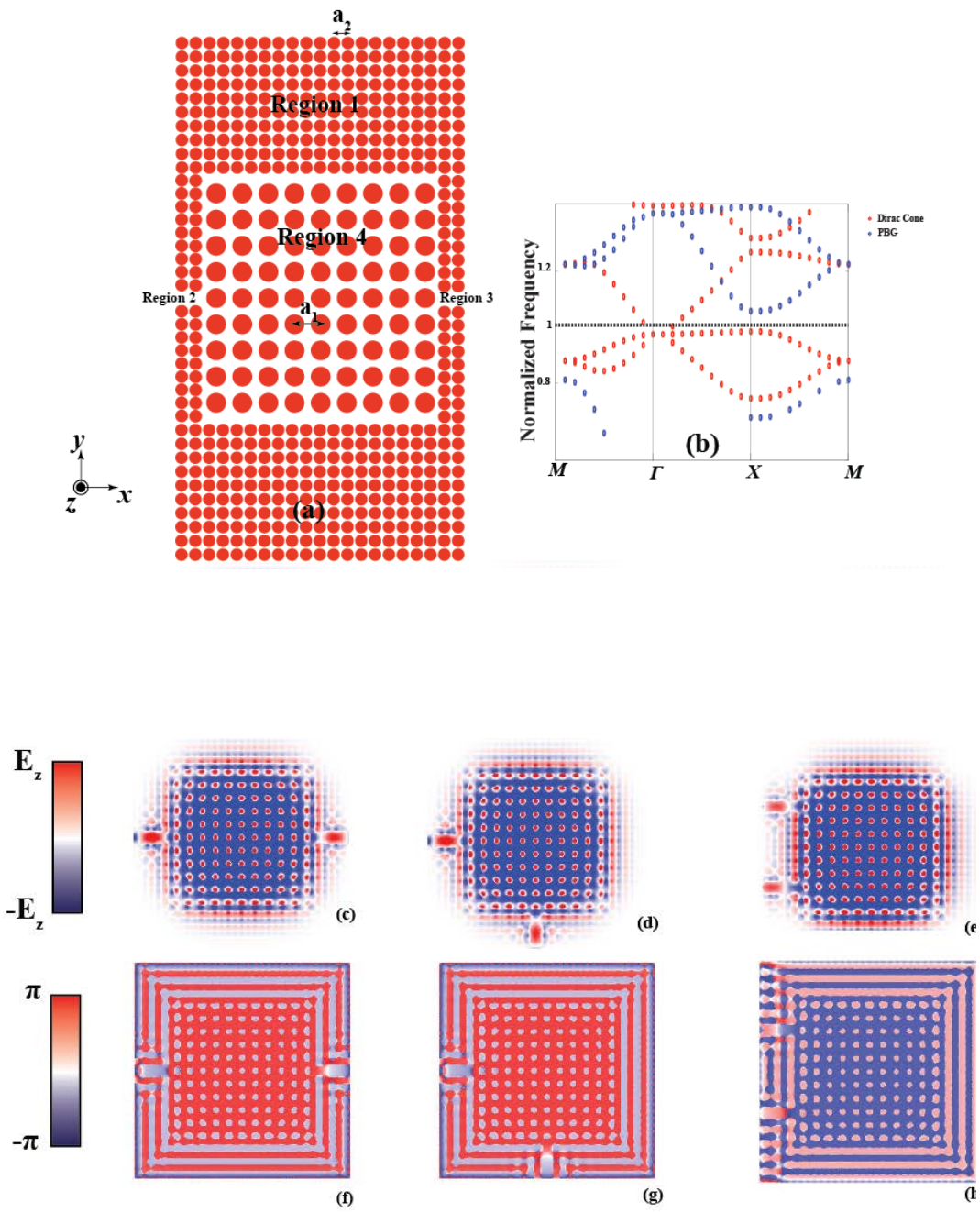

Fig. 21 ***Proposed structure for preserved interaction between two emitters regardless from their relative orientation in silicon based photonic crystal environment****, (a) Geometry of proposed structure, A photonic bandgap (PBG)*

photonic crystal (Region 1) with 2 defect regions (Region 2 and 3) that constitute the waveguides that are separated by a Dirac point PC (Region 4). (b) Bandstructure of the PBG (Region 1) and the Dirac cone PC (Region 4), (c), (d) Snapshot, Phase of the electric field (E_z) when the defect waveguides are straight, 90^o *bent,* 180^o *bent respectively*

CHAPTER 3 All-passive nonlinear electromagnetic ‘diode’and nonreciprocal metastructure

3.1 Introduction

One of the main challenges in the microwave, terahertz, optics and photonic systems is the design of electromagnetic systems that can transmit waves only in one direction. Based on the Lorentz reciprocity lemma, the transmission symmetry and the system reciprocity may be broken within one of the following paradigms: magnetically active systems [88–90], systems with time dependent material properties [9,91], and systems exhibiting nonlinear response in asymmetric structures [92–108]. Currently magneto-active devices are among the most commonly used systems for breaking the reciprocity and achieving optical isolation (almost all optical isolators and circulators available commercially exploit the magneto-optical activity). . It is worth mentioning here the works on optical isolation with magneto-photonic crystals [109,110]. However, such systems operate for the oblique incidence and can not serve for the optical isolation in waveguiding structures or for normally incident plane waves. Moreover, the intrinsic losses, relatively bulky systems, weak magneto-optical activity, and often inefficient design have motivated search for new methods and systems where the reciprocal symmetry of EM wave transmission may be broken using other mechanisms. Among the recent proposals are electrically biased systems exploiting active electronic elements to mimic the magnetic activity [111,112], and systems with spatio-temporal modulation of material parameters (which may also be classified as biased systems) [9,91]. The main goal

of this chapter is to develop a paradigm for a nonreciprocal system that does not require any biasing (i.e., self-sustained system) and that acts as an optical diode transmitting light in one direction and reflecting it in the other direction, such that the information is preserved. A possible way to design such a system is to utilize the nonlinear response in an asymmetric system. Indeed many previous works have proposed both theoretically and experimentally the concept of an electromagnetic diode using nonlinearities. It was shown in those works that by combining optical nonlinearity with structural asymmetry it is possible to achieve either significant difference in the transmission between forward and backward propagating waves (having high Nonreciprocal Transmission Ratio (NTR)) at the cost of having a very low transmission at the forward direction (having very high Insertion Loss (IL)) [92–100], or having an acceptably low IL at the expense of having low NTR [101–103]. In other words, owing to the design principles utilized in those works, there has always been a dramatic trade-off between having a high NTR and having an acceptably low Insertion Loss (IL). To shed more light on this trade-off we include Table 1 in which we report the results obtained in some of the most important past works within that paradigm (among other techniques like using PT symmetry that still suffer from the same trade-off). In [113] the general limitations of nonlinear systems when exploited for optical isolation are discussed in details. Traditionally optical diode behavior within such systems is based on the direction dependent resonance shift in structures with some distributed nonlinearity (with 3 exceptions to be discussed later in this section), for example, a nonlinear defect slab in a photonic crystal [106], or a nonlinear microring resonator combined with the structural asymmetry [92]. The nonlinear layer (or resonator)

is typically of the order of several wavelengths for efficient accumulation of the nonlinear response, e.g. nonlinear phase or resonance shift, and is sensitive to the average amplitude profile in the nonlinear element, rather than the local field intensity. Hence, one needs to design the structural asymmetry in such a way that the average amplitude in the whole slab is essentially different for forward and backward direction of illuminations. The latter can be achieved with the use of evanescent fields that due to their exponential amplitude profile naturally have strong amplitude gradient – placing the nonlinear element in the different parts of the evanescent field it is possible to trigger significantly different nonlinear responses, i.e., achieve very high NTR (Here we would like to refer to the Fig. 22 in Ref [95] that illustrates well this concept). It is obvious that transmission based on evanescent fields exploiting the tunneling mechanism is essentially low, leading to significant IL. Worth mentioning here is the work within the same paradigm constrained by the same trade-off, in which an acceptable IL and NTR have been achieved at the expense of having a large structure by cascading multiple defects within a photonic crystal environment [107]. In addition to the more conventional approach of achieving nonreciprocal transmission using nonlinearities that we discussed in the previous paragraph and to which we compared and pointed out the novelty of our work, to the best of our knowledge, there have been three works in the literature in which a different approach was used. In this paragraph we will point out clearly the mechanism on which those works are based and explain the advantage of using our approach when compared to them. (1) First, in Ref [104,105], where it was proposed theoretically [104] and shown experimentally [105] that a nonlinear waveguide for second-harmonic generation in

which the insertion of a localized phase discontinuity leads to nonreciprocal behavior. Although offering an elegant platform for nonreciprocal transmission, the work however has a few limitations that we try to eliminate in our work. First, since the optical diode behavior in that scenario is based on the process of second harmonic generation, it requires a host waveguide that is inherently nonlinear, imposing all the challenges and limitations of second harmonic generation including the necessity of satisfying the phase matching condition, a significant overlap integral between the mode profiles at the two frequencies in addition to being bound to devices of sizes comparable to the characteristic nonlinear length (The structure size was 4 cm for 1.55 um operation wavelength, ∽ 26000 λ). Furthermore, the proposed technique is such that the forward signal is transmitted, whereas the backward propagating signal is transferred into the "idler" second harmonic mode rather than reflecting back, a similar phenomenon as the one proposed in [9,91], i.e., technically withdrawing the signal from the system, or in the network theory language having the system as effectively a three-port system, rather than a strictly two-port system as the one we propose in our work which strictly follows the definition and functionality of an electromagnetic diode, namely a two port network device that allows the signal propagation in one direction and reflects it back in the other direction. (2) Among all the previous nonlinear diode works, to the best of our knowledge, ref [106] stands out as the only work in which local nonlinearities have been used, introduced as a δ- function Kerr nonlinearity. However, the idea of using the local field asymmetry that we propose in our work, to effectively trigger such local nonlinearity was not utilized there. Instead, the nonlinear layer was placed in a rather

arbitrary location within a composite RH/ LH periodic lattice aiming for enhancing the nonlinear effects. It should be noted that since the local field asymmetry was not utilized in that work, nonreciprocal transmission was achieved using an extremely high nonrealistic nonlinearity coefficient of 4. (3) Finally, we would like to point out the very recent work by Bulgakov and Sadreev [108] in which a design of all-optical diode in L-shaped photonic crystal asymmetric waveguide is proposed. It is based on a single nonlinear Kerr microcavity with two degenerate dipole modes. Asymmetry of the waveguide is achieved through different couplings of the dipole modes with the left and right legs of the waveguide. From one arm only one dipolar mode of the cavity is excited and the power reflects back, and from the other side coupling into the orthogonal dipolar mode of the cavity takes place, which leads to coupling into the second arm. However it is different from our work in the fact that the idea is rather specific to guided scenarios in addition to the fact that the resonator itself is inherently non-subwavelength. It has to be electrically large for efficient excitation of the dipolar modes. In addition, this idea of using the two degenerate modes can not be used in a strictly 1D scenario (metasurface) like ours for unbounded wave propagation.

Reference	IL (dB)	NTR (dB)
92	35	28
93	15.5	40
94	43	14
95	20	20
96	35	28

97	13.9	18
98	8.3	30.8
99	20 and 3	7 and 1.5 (respectively)
100	10	25
101	N/A	2.4
102	1.5	2
103	0.8	0.8
Our work	3.7	16 (Tunable)

Table 1: Insertion Loss (IL) and Nonreciprocal Transmission Ratio (NTR) of some nonlinear diodes reported in the literature

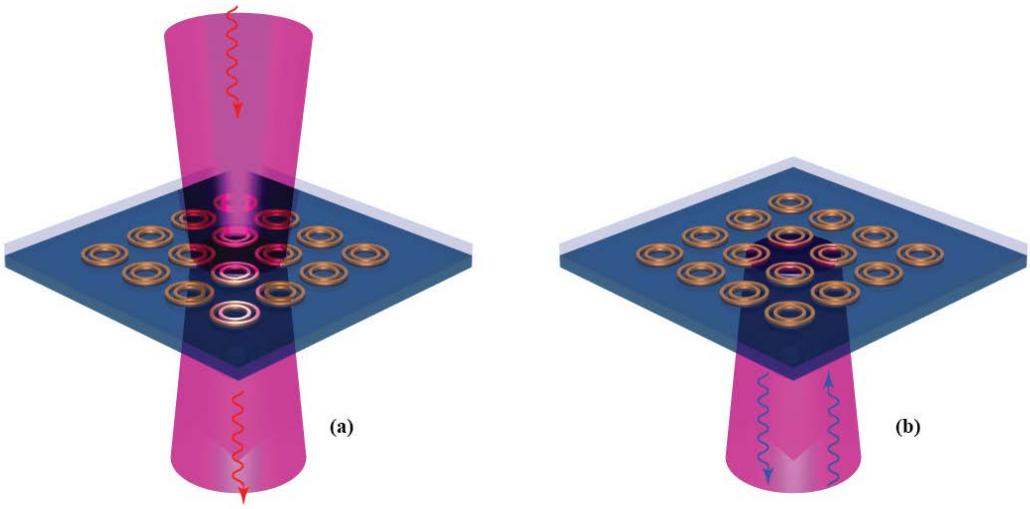

Fig. 22 Schematic illustration demonstrating our vision of an all-passive metasurface.

Here the metasurface acts as a one-way window transmitting light in one direction (a) and reflecting it for the other direction of incidence (b). Such an asymmetric transmission is possible due to an array of subwalength nonlinear resonators on top of a substrate and coated by a thin layer of dielectric with a different permittivity. The substrate and the coating naturally create a structural asymmetry important for the diode operation. This simple paradigm of design may be extended to other frequency domains as well.

In our work, we propose a different approach trying to overcome the above mentioned limitations. We show that utilizing subwavelength nonlinear elements and exploiting local nonlinear response (i.e., response to the local intensity of the electric field) it is possible to operate with propagating waves, rather than the evanescent waves and thus achieve higher performance. Importantly, our design principle allows for significantly reducing the size of the system while dramatically enhancing the performance of our nonlinear diode by making the above-mentioned trade-off between having a low IL and a high NTR less dramatic. We stress that our idea is rather general and may be exploited in different frequency regimes, including optical frequencies; provided that the subwavelength nonlinear resonant system is designed (it is worth mentioning that number of groups are working on engineering such elements [114–116]). Here we present a proof-of-principle simulation of our proposal in a microwave frequency domain, however, we see no fundamental limitations of extending our ideas to terahertz, near infrared, and optical frequencies. Furthermore, having such an efficient electromagnetic diode in hand we show that it may serve as a building block for more complex structures, such as, for example, Faraday-like metasurfaces that can mimic the

nonreciprocal polarization rotation, which previously has been achieved only within biased and/or active structures. We note that our idea of subwavelength nonlinear diode allows for the design of a subwalength nonreciprocal metasurfaces. A schematic illustration of our vision is presented in the Fig. 22. Here the substrate and superstrate, which are inherently present in any metasurface design, create a natural asymmetry necessary for the diode operation. As we will also show later, the thickness of both substrate and cover layer may be chosen smaller than the free-space wavelength.

3.2 Proposed concept for electromagnetic 'diode'

As mentioned earlier, to the best of our knowledge previous designs of an all-passive nonlinear electromagnetic diode reported in the literature have certain limitations that include the inherently large size of the device in addition to the significant trade-off between the transmission ratio and the insertion loss. Traditionally optical diode behavior within such systems is based on the direction dependent resonance shift in structures with some distributed nonlinearity, for example, a nonlinear defect slab in a photonic crystal [95], or a nonlinear microring resonator combined with the structural asymmetry [92] (We like to mention here that somewhat similar asymmetry mechanism is used in gain-loss, i.e., PT-symmetric, systems [99,100,117]). In contrast, here we show that utilizing subwavelength nonlinear elements and exploiting *local* nonlinear response (i.e., response to the local amplitude of the electric field) it is possible to operate with propagating waves, rather than the evanescent waves and thus achieve higher performance. Importantly, our design principle allows the possibility to reduce the size of the system significantly while enhancing the performance of our nonlinear diode by making the above-mentioned trade-

off between having a low IL and a high NTR less dramatic. We stress that this approach is rather general and may in principle be exploited in different frequency regimes, including optical frequencies provided that the subwavelength nonlinear resonant system is utilized [114,115,118,119].

We begin our analysis with the study of field distributions in a linear bilayered one-dimensional (1D) asymmetric slab infinitely extent in the transverse directions, schematically shown in Fig. 23(a).

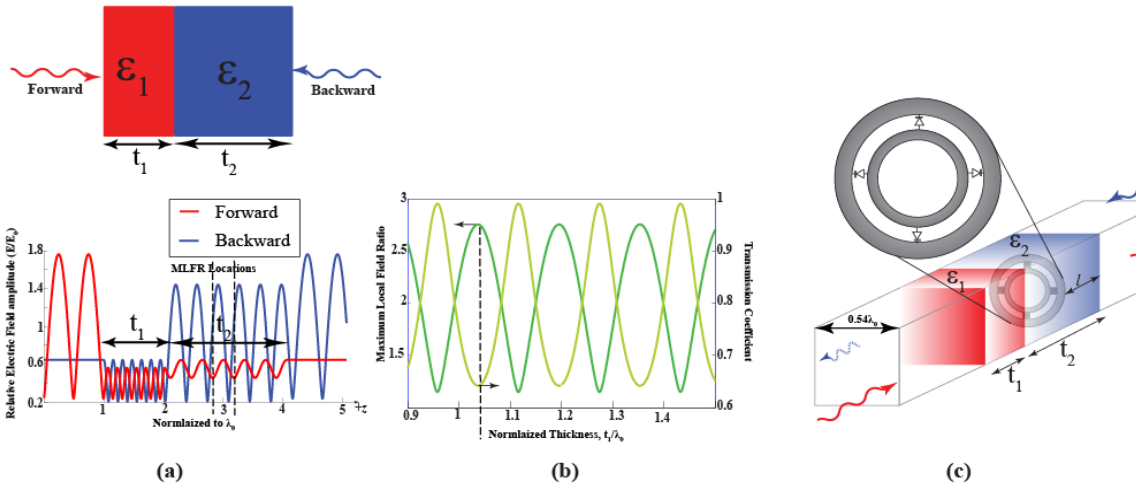

***Fig. 23 Concept of the proposed electromagnetic wave diode**: (a) The relative electric field amplitude distribution within a bilayered asymmetric one-dimensional (1D) slab infinitely extent in the transverse directions (normalized to incident field amplitude E_0). While the paired slab is reciprocal, the amplitude of the total electric field distribution in the partial standing waves within the structure is dependent on the side from which it is excited. The red and blue curves show the field amplitude distribution normalized to*

incident field amplitude E_0) for the forward (+z) and backward (-z) propagating waves, respectively. The dashed lines show two of the locations of maximum local field ratio "MLFR", where the ratio between the local field amplitude for the forward and backward illumination is maximum. These are the planes where nonlinearly loaded resonator should be inserted for the most efficient nonlinear response. (b) Maximum local field ratio (MLFR) (green curve) and transmission coefficient (yellow curve) versus normalized thickness t_1. The dashed line shows the operating point for which the normalized field distribution is shown in panel (a). (c) Bilayered asymmetric slab consisting of two layers with dielectric permittivities ε_1 and ε_2 and thicknesses t_1 and t_2 are inserted in the squared-cross section metallic waveguide. The inset shows the varactor-loaded thin resonator placed at a distance l from one of the slabs ends where one of the MLFR locations is. The resonator is made of two concentric rings loaded by four varactors distributed symmetrically along its perimeter. The bilayered slab and the ring resonator are placed within a rectangular waveguide.

The slab consists of two linear dielectric layers with dielectric permittivities ε_1 and ε_2 and thicknesses t_1 and t_2 respectively. Illuminating the slab from either side causes formation of partial standing wave patterns in the structure. Owing to geometrical asymmetry of the system the field profiles inside the slab would be generally different for opposite directions of illumination, see Fig. 23(a). Note that in such a linear system due to the structure's reciprocity transmission characteristics for both directions of illumination would be identical. However, the local field amplitudes in the partial

standing wave regions for the forward and backward directions of illumination are essentially different as depicted in Fig. 23(a). Furthermore, inside the slab, positions, where the local field amplitudes ratio between the cases of forward and backward propagating waves is maximum, namely maximum local field ratio (MLFR) locations, exist. Therefore, nonlinear, amplitude-dependent, resonant structures with thicknesses much smaller than the wavelength, i.e. essentially subwavelength, when placed at those locations may respond differently to the two different directions of illumination. In Fig. 23(b), we choose ε_1 and ε_2 to be $10\varepsilon_0$ and $2\varepsilon_0$, respectively, and t_2 to be 2.03 λ_0, where λ_0 is the free space wavelength at the operating frequency. We plot the MLFR along with the corresponding transmission coefficient versus the variation of the relative thickness of the first layer in the bilayer slab (by varying t_1 / λ_0). Our analysis shows that when $t_1 = 1.03\lambda_0$, about 0.65 transmission coefficient and an MLFR of 2.733 can be achieved. This is the case for which the field distribution is plotted in Fig. 23(a). We should emphasize that while we show the example of slabs with the thicknesses of $t_1 = 1.03\lambda_0$ and $t_2 = 2.03\lambda_0$ in order for the field distributions to be clearly visible to the reader; our design can be made for the subwavelength-thick slabs as shown in a following section. Moreover, although the above discussion was for the 1D slab infinitely extent in the transverse directions, hereafter without loss of generality and for the sake of simplicity and reduction in numerical complexity in the proof of concept we study the optical diode behavior in a rectangular waveguide at microwave frequencies. The corresponding geometry is shown in Fig. 23(c) where we have a metallic waveguide with

a squared cross section 0.54 λ_0 x 0.54 λ_0. Using the same parameters (thicknesses and permittivities) mentioned above for the bilayered slab, now embedded inside the waveguide we achieve a transmission coefficient of 0.425 and an MLFR of 4.4 as explained in details in a following section.

3.3 Maximum local field ratio versus Transmission coefficient in a bilayered asymmetric slab

In this section we show a more detailed discussion regarding the relationship and trade-offs between the transmission coefficient and the MLFR. Moreover, we show an example of thinner (subwavelength-thick) 1D slabs with the same set of dielectric constants in which the same MLFR and transmission coefficient are preserved).

As shown in Fig. 24 we perform a study, in which we fix ε_2 to be $2\varepsilon_0$ and t_2 to be $0.1\lambda_0$, where λ_0 is the free space wavelength. Then for different values of ε_1, we sweep over t_1 and plot both the transmission coefficient and the MLFR for each case. As shown in Fig. 24, there is a trade-off between achieving high transmission coefficient and high MLFR. Moreover, the lower bound of the transmission within the system is set by the level of asymmetry between the two slabs constituting the bi-layer slab, i.e. how different are ε_1 and ε_2. For example, comparing Fig. 24(a) where $\varepsilon_1 = 4\varepsilon_0$ and Fig. 24(f), where $\varepsilon_1 = 100\varepsilon_0$, ($\varepsilon_2 = 2\varepsilon_0$ for all cases as mentioned above), we can see clearly that for the former case the lower bound of the transmission coefficient is about 0.86, with a corresponding MLFR of around 1.75. However in the latter, the lower bound of

the transmission coefficient is as low as around 0.25 with a corresponding MLFR of around 8.3.

As a proof of concept we choose to utilize the case depicted in Fig. 24(d) in which we can achieve both good MLFR and acceptably high enough transmission coefficient to further demonstrate our concept. As depicted in Fig. 24(g) if we choose to operate at the near full transmission point (around 0.98 transmission coefficient), the field distributions inside the structure illuminated from both sides are almost identical and we do not achieve any significant MLFR. However if we choose to work at the lower bound of transmission (that is around 0.65 coefficient), this corresponds to an MLFR of around 2.733, which is clearly depicted in Fig 24(h). Note that in the previous section we utilize a bilayered slab of larger thickness (around $3\lambda_0$, and both as 1D slabs (Figs. 23(a) and 2(b) and inside the waveguide (Fig. 23(c)) than what is shown in this section mainly for the sake of visual clarity throughout all the figures. As shown here, however, we can achieve somewhat similar transmission coefficient and MLFR reported for the thicker structure (which directly translates into an acceptably low insertion loss accompanied by a good nonreciprocal transmission ratio after the nonlinear element is inserted) using a structure of a total thickness of around $0.327\lambda_0$ (for the 1D slab case) with the same set of dielectric constants. This verifies that in principle our approach may apply for subwavelength structures.

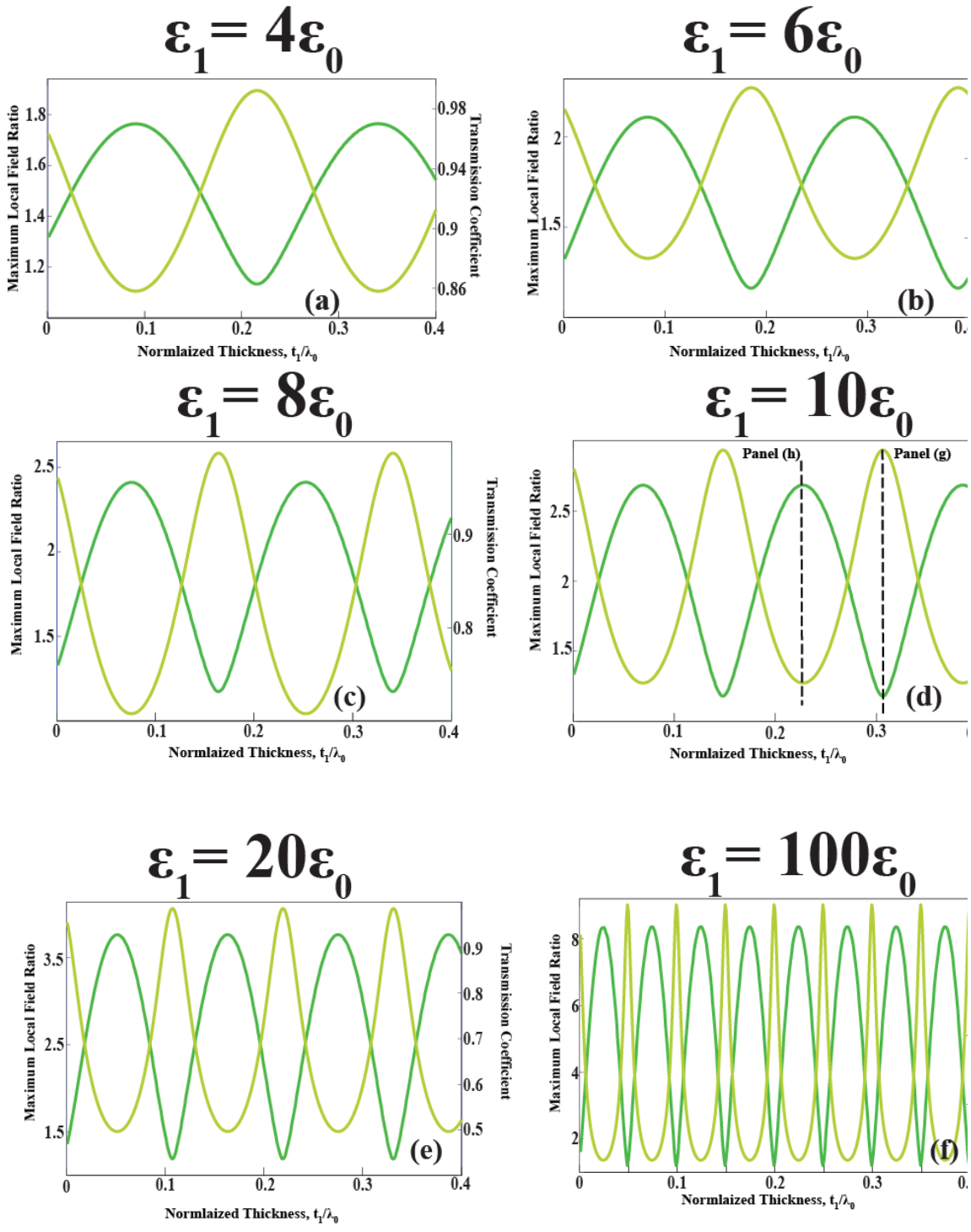
ε1= 4ε0
Maximum Local Field Ratio
Transmission Coefficient
Normlaized Thickness, t1/λ0
(a)
ε1= 6ε0
Maximum Local Field Ratio
Normlaized Thickness, t1/λ0
(b)
ε1= 8ε0
Maximum Local Field Ratio
Transmission Coefficient
Normlaized Thickness, t1/λ0
(c)
ε1= 10ε0
Panel (h)
Panel (g)
Maximum Local Field Ratio
Normlaized Thickness, t1/λ0
(d)
ε1= 20ε0
Maximum Local Field Ratio
Transmission Coefficient
Normlaized Thickness, t1/λ0
(e)
ε1= 100ε0
Maximum Local Field Ratio
Normlaized Thickness, t1/λ0
(f)

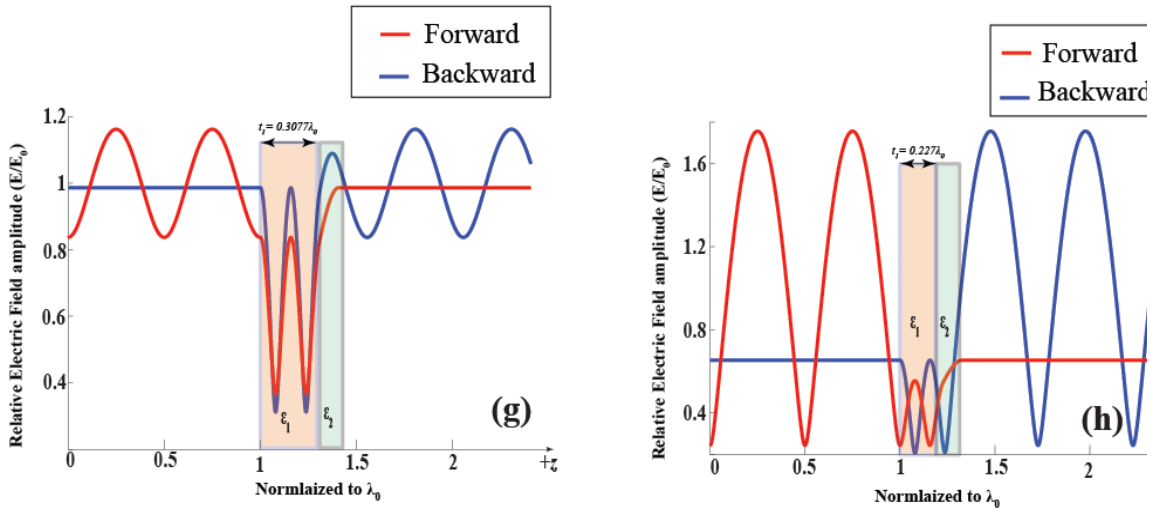

Fig. 24 Maximum local field ratio versus transmission coefficient*. Maximum local field ratio (green curve) and transmission coefficient (yellow curve) of a pair of 1D slabs infinitely extent in the transverse directions, versus normalized thickness* t_1 *for* $t_2 = 0.1\lambda_0$, $\varepsilon_2 = 2\varepsilon_0$, *and* $\varepsilon_1 = 4\varepsilon_0$ *(a),* $6\varepsilon_0$ *(b),* $8\varepsilon_0$ *(c),* $10\varepsilon_0$ *(d),* $20\varepsilon_0$ *(e), and* $100\varepsilon_0$ *(f). The relative electric field amplitude distribution within a bilayered asymmetric one-dimensional (1D) slab infinitely extent in the transverse directions (normalized to incident field amplitude* E_0*) for: a case of close to full transmission (about 0.98 transmission coefficient) and that leads to a negligible MLFR (g), a case of 0.65 transmission coefficient and a pronounced MLFR (h).*

3.4 Maximum local field ratio versus Transmission coefficient in a bilayered asymmetric slab inside a waveguide using commercially available materials

In Fig. 25(a) we repeat Fig. 23(b), but this time within the waveguide defining MLFR and transmission coefficient for the $0.54\lambda_0 \times 0.54\lambda_0$ waveguide and using realistic commercially available materials with their losses included. In Fig. 25(a) we have, $\varepsilon_1 = (10 + 0.0007i)\varepsilon_0$ which is commercially available from Emerson & Cuming under the set of materials labelled "ECCOSTOCK HiK500F" , $\varepsilon_2 = (2 + 0.0002i)\varepsilon_0$ which is the commercially available Teflon AF 1600 that can be purchased from (among many other companies) Dupont and $t_2 = 2.03\lambda_0$. We plot the MLFR along with the corresponding transmission coefficient versus the variation of the first layer t_1 / λ_0. The analysis shows that when $t_1 = 1.03\lambda_0$ we achieve a transmission coefficient of 0.425 and an MLFR of 4.4, which are the values utilized in our nonlinear diode in a rectangular waveguide example. We note that similar analysis is shown in Fig. 25(b), however limiting the thickness of the bilayered slab to be subwavelength by choosing $t_2 = 0.5\lambda_0$ and varying t_1 / λ_0. A similar transmission coefficient and MLFR to the ones shown in fig. 24(b) can be achieved for $t_2 = 0.19\lambda_0$.

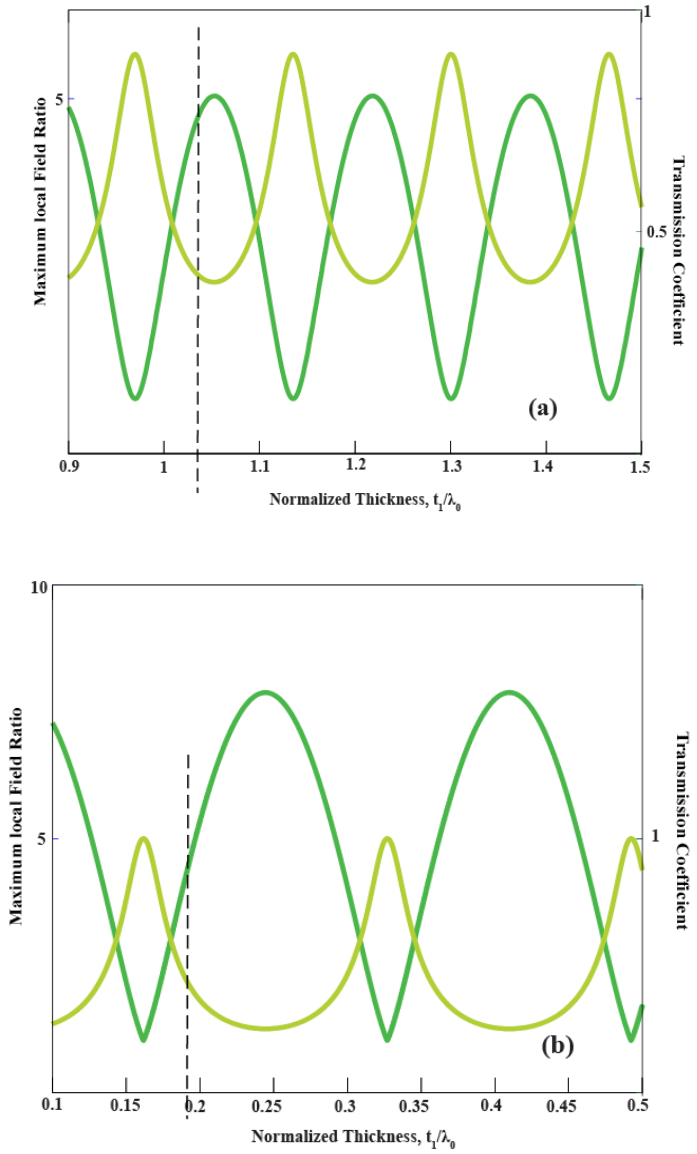

Fig. 25 **Maximum local field ratio versus transmission coefficient using commercially available dielectrics inside a waveguide.** *(a) Maximum local field ratio (MLFR) (green curve) and transmission coefficient (yellow curve) versus normalized thickness* t_1/λ_0 *with* $t_2 = 2.03\lambda_0$, $\varepsilon_1 = (10 + 0.0007i)\varepsilon_0$, *and* $\varepsilon_2 = (2 + 0.0002i)\varepsilon_0$ *(b) Similar to (a) with* $t_2 = 0.5\lambda_0$. *The dashed lines show the operating point for which a*

transmission coefficient is 0.425 and MLFR is 4.4 as the ones shown in fig. 24(b) where the bilayered slab total thickness was chosen to be around $3\lambda_0$ *for visual clarity of the figures.*

3.5 Geometry and materials

We now place the nonlinear subwavelength resonant structure at one of MLFR locations, i.e., $l = 1.65\lambda_0$, where l is the distance from the edge of the slab of permittivity ε_2 and thickness t_2 as shown in Fig. 23(c). The schematic of our nonlinear subwavelength resonant structure is shown in Fig. 26. Here we consider two concentric rings with four nonlinear amplitude-dependent capacitive elements (commonly known as varactors) [120–122] symmetrically placed between the rings, as shown in Fig. 26 considering that the nonlinear element is essentially subwavelength ring resonator (we note that our design can be easily extended to an infinite array of resonators, but here we consider a ring resonator in a waveguide).

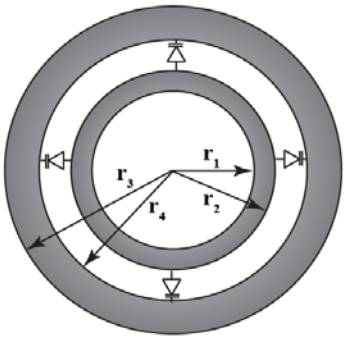

Fig. 26 Schematic of the nonlinear resonant structure*. It is formed of two concentric rings and loaded with four nonlinear Varactors*

The nonlinear resonant layer is chosen to be two concentric rings with r_1, r_2, r_3, and r_4 being $0.03\lambda_0$, $0.08\lambda_0$, $0.0975\lambda_0$, and $0.1475\lambda_0$ respectively as shown in Fig. 26. The rings are assumed to be perfect electric conductor (PEC) and have a thickness of $0.0004\lambda_0$ for the purpose of our numerical simulation. The resonator is loaded with four nonlinear varactors as shown in Fig. 23 and Fig. 26. Such a unit cell is suitable for a diode-like operation that is polarization-angle independent, as well as having a small footprint for a specific resonance frequency, as compared with a single ring resonator. The resonator is then incorporated at the MLFR location, such that when the resonator is fed from one side depending on the power level its resonance frequency may be different from the resonance frequency when fed from the other side, owing to the change of the varactor's capacitance. This is due to the fact that the local fields caused by excitations from the two sides are different. The dimensions of the resonator itself are chosen such that it is almost "transparent" (i.e., low scattering at off-resonance) when the varactor is

operated in the linear regime being excited with low power, and as the power level is increased, its functionality moves towards being “opaque” (i.e., high scattering at resonance). Therefore, when excited from the side that induces relatively low local field at the varactor’s location, the resonator is still “transparent” and we get a relatively high transmission, which is about 0.42 in this design for an input power of 30 dBm. On the other hand, when the structure is excited from the other side using the same power level, that induces high local field at the varactor’s location, the resonator turns to be “opaque” and the wave transmission in that direction is much less. The varactor diode used in our design is the so-called Heterostructure Barrier Varactor (HBV) [122], which exhibits a symmetric C (V) characteristic. It is clear that such symmetry property allows the use of an unbiased device and the capacitance control utilizing a moderate signal.

3.6 Concentric rings resonator modes and performance

In this section we shed some light on the chosen resonator and its performance. The shape of the resonance curve is due to the interaction between two ring eigenmodes with different symmetries. Note that an analogous system has been studied and classified using hybridization in [123] , where the modes were classified based on the induced charge distribution and the shape of the resonance curve was explained based on a hybridization model. In fig. 27 we show a similar analysis for our structure, which analogously resembles the results in [123].

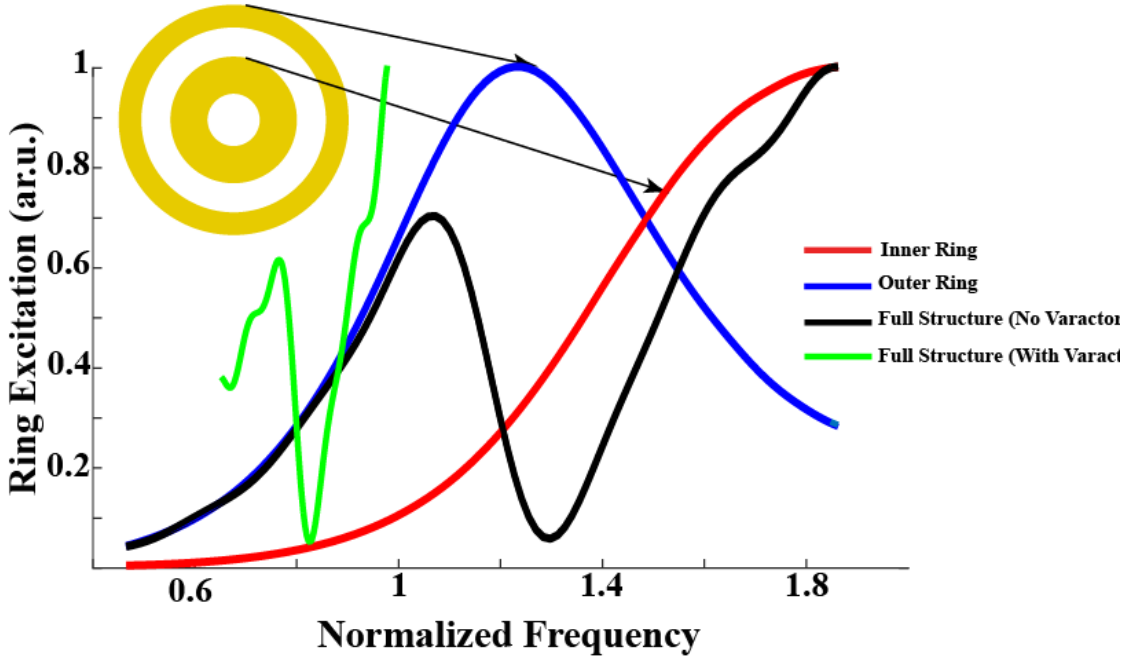

Fig. 27 Analysis of ring resonator resonances*. Ring excitation of inner (red curve), outer (blue curve), full structure without varactors (black curve), and full structure with varactors (green curve). The inset is from Ref* [123].

We further note that our analysis shows that qualitatively the ring response is the same inside the waveguide and for the case of a plane wave illumination, see fig. 28(a). In both cases the excitation of two modes (symmetric and antisymmetric) is clearly seen.

The corresponding field distribution is shown in Fig. 28(b), and (c) for the plane wave illumination and in fig. 28(d) and (e) for the waveguide excitation.

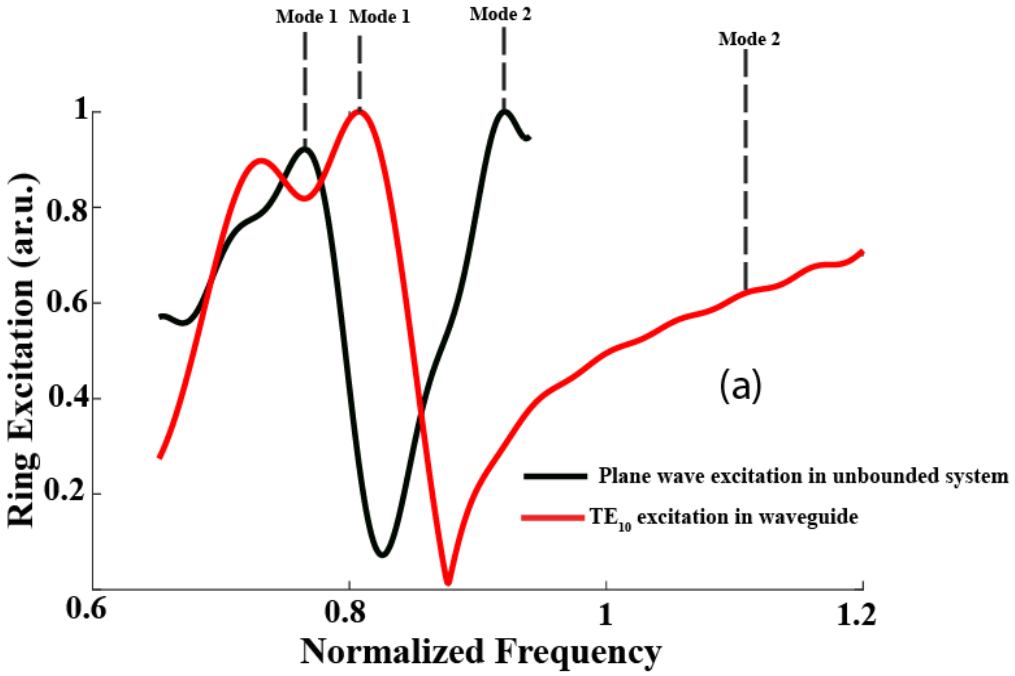

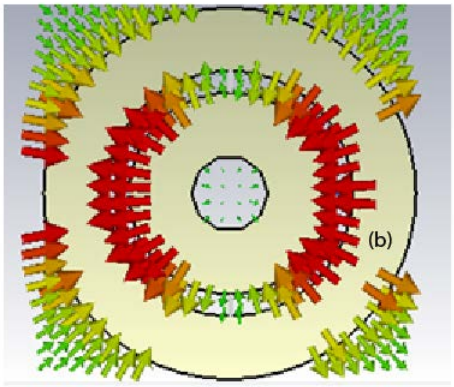

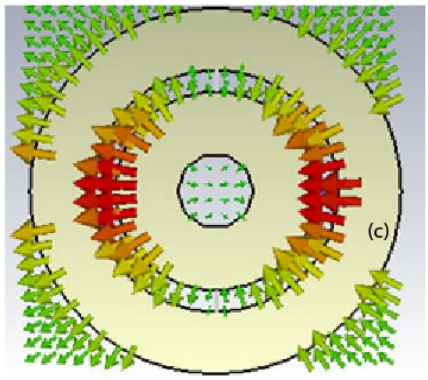

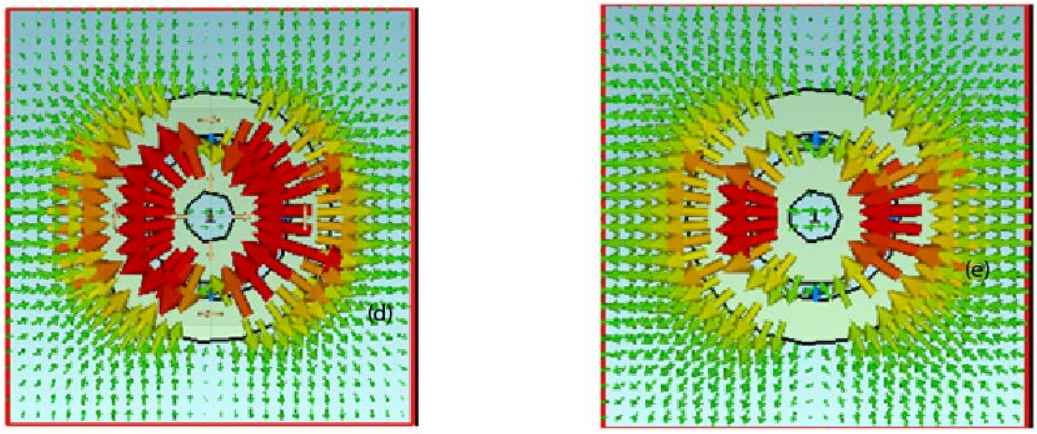

Fig. 28 Analysis of ring resonator resonances and eigen modes*. (a) Ring excitation in unbounded system excited by plane wave (black curve), and inside a waveguide excited by* TE_{10} *mode (red curve), Electric field distribution across the ring in unbounded system at (b) first resonance (labelled mode 1 on black curve), (c) second resonance (labelled mode 2 on black curve), Electric field distribution across the ring in a waveguide at (d) first resonance (labelled mode 1 on black curve), (e) second resonance (labelled mode 2 on black curve)*

We now address a very important question regarding the excitation of the ring resonator. It is clear that such resonator supports symmetric and antisymmetric modes, with parallel and anti-parallel currents along the two rings, with the anti-symmetric mode being the one that interacts with the diodes, since it is the only one allowing current flow through the diodes. The anti-symmetric mode can only be excited by waves with nonzero magnetic field perpendicular to the ring plane. Normally incident plane waves do not satisfy this requirement, so it may look at a first glance the excitation of the resonators is made possible only through the normal magnetic field component of the TE mode of the

waveguide containing the ring, and that it is not possible to excite the varactors in an unbounded scenario where we have a plane wave. We stress that the mode configuration is determined by the induced charge distribution (i.e., electric field map) and not the distribution of the surface current in the rings. Furthermore, our analysis of the surface current (see fig. 29) shows that the surface current distribution is always antisymmetric. And indeed, only anti-parallel current distribution excites the varactors. But we note that this configuration is always excited in our system, even in the case of a plane wave (where there is no longitudinal magnetic field). Thus our design is not limited only to TE modes and can be used for infinitely extended structures excited with plane waves.

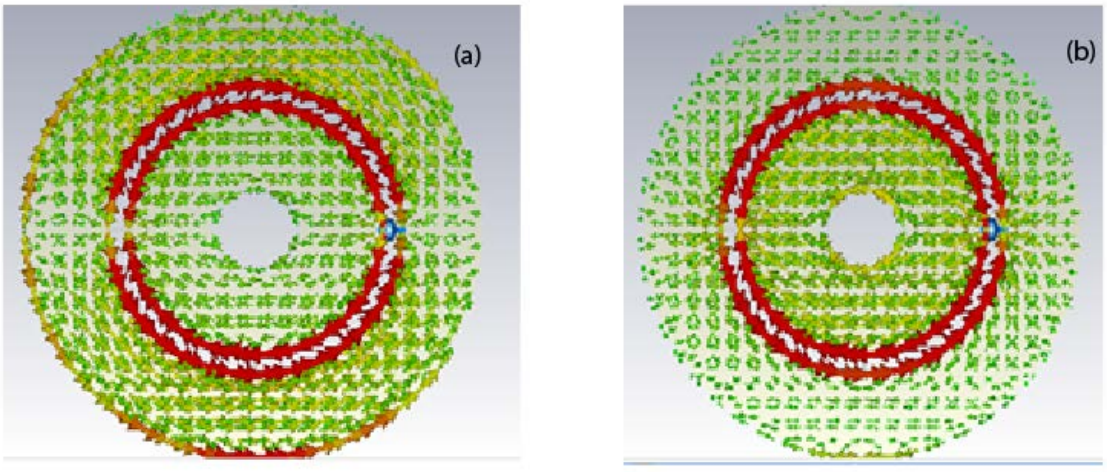

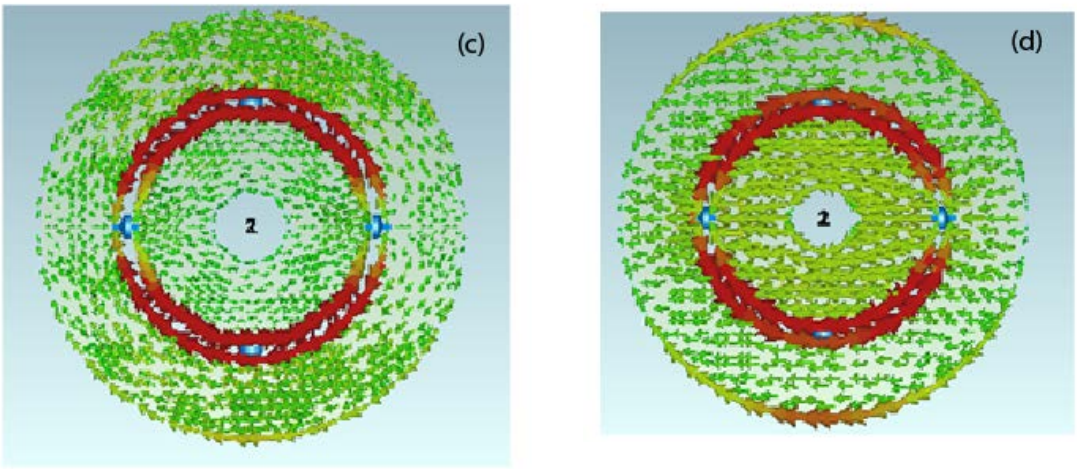

Fig. 29 Surface current distribution across the ring resonator. *Surface current distribution across the ring in unbounded system at (a) first resonance (labelled mode 1 on black curve), (b) second resonance (labelled mode 2 on black curve), Surface current distribution across the ring in a waveguide at (c) first resonance (labelled mode 1 on black curve), (d) second resonance (labelled mode 2 on black curve)*

3.7 Proof of preserving MLFR and its locations

In order to prove that the MLFR and its locations would be preserved when a sub-wavelength layer is added to such a structure we have developed a transmission line model for this case, see Fig. 30. Within this model the backward and forward plane waves can be modeled as a.c. voltage wave with an amplitude V. The resonant structure is described by lumped impedance Z. The impedances Z_1 and Z_2 correspond to the input impedances at the resonator's plane looking right (forward) and left (backward),

respectively. In this case the field amplitude within the subwavelength layer can be found as:

For forward propagating waves and as

$$v_1 = \frac{Z//Z_2}{Z//Z_2 + Z_1} V$$

and for backward propagating waves.

$$v_2 = \frac{Z//Z_1}{Z//Z_1 + Z_2} V$$

Thus

$$\frac{v_2}{v_1} = \frac{Z_1}{Z_2}$$

From this analysis, we clearly see that for exactly the same amplitudes of the incident forward and backward illuminations the ratio in the corresponding local amplitudes in the subwavelength layer is independent of the resonant structure placed there, and solely depends on the ratio of the input impedances looking both ways. In a transmission matrix approach the latter condition corresponds to the limit of having an electrically small enough resonant structure in the direction of propagation, over which no significant propagation phase accumulates.

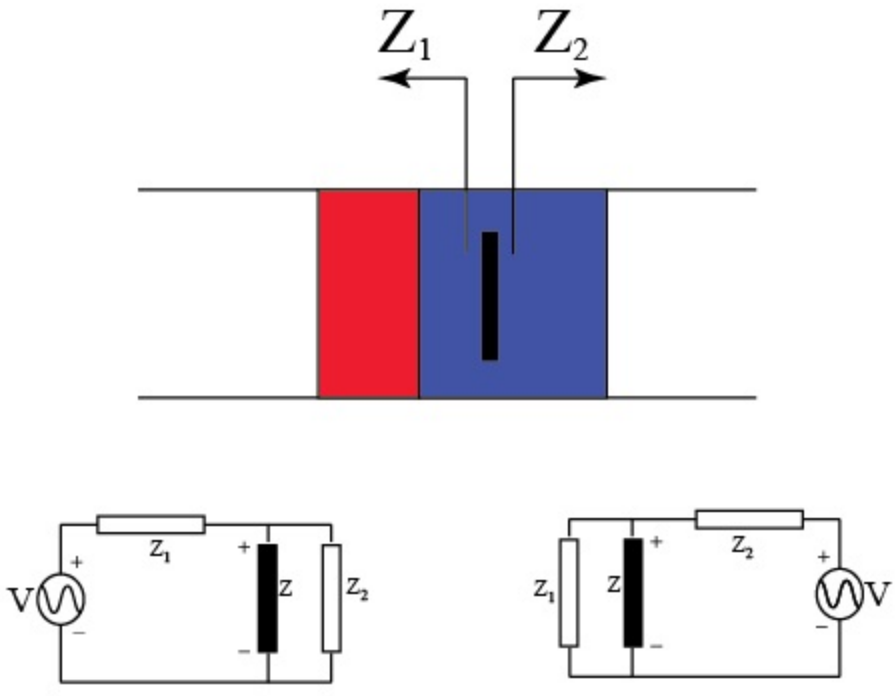

Fig. 30 Equivalent Transmission-Line Model of the asymmetric structure loaded by a planar resonant structure at "MLFR" locations. *Z_1 is the input impedance at the resonant structure plane looking towards the left, while Z_2 is the input impedance at the resonant structure plane looking towards the right*

We stress here that this condition of local symmetry breaking in field amplitudes for forward and backward illumination directions is independent of some of the characteristics of subwavelength layer itself (i.e. independent of its internal structure, resonant behavior, material parameters etc.) and is valid for the limit for which the layer thickness is much smaller than the operating wavelength. Recently a significant nonlinear response was predicted in various subwavelength systems, including plasmon enhanced

nonlinearities in nanoscale metallic nanostructures at optical frequencies [114,124], giant nonlinear response achieved by coupling electromagnetic modes in plasmonic metasurfaces with quantum engineered electronic intersubband transitions in semiconductor heterostructures [119], and strong nonlinerities in graphene in visible, infrared and terahertz frequency domains [125,126]. Utilizing such structures might pave a way for compact nonlinear electromagnetic diodes using our proposed structure

3.8 Performance of proposed electromagnetic 'diode'

As mentioned before, we choose the dimensions of the nonlinearly loaded resonator such that in its linear state its resonant frequency is detuned from a given operating frequency, implying that the ring is effectively "transparent". For higher intensities we expect a shift of its resonance frequency (due to changing the value of the varactor capacitance) towards the operating frequency with a corresponding decrease in transmission (when the resonance frequency of ring coincides with the operating frequency almost total reflection is expected). Consequently, by inserting such a nonlinear element at the MLFR location within the bilayered dielectric structure in the waveguide, as shown in Fig. 23(c) and Fig. 31(a), it is possible to tune the transmission properties with respect to the direction of illumination and the power level. It is worth noting that there are, in principle, two resonance phenomena at work here: (1) resonance of the ring, and (2) resonance due to the bilayered dielectric slab (i.e., Fabry-Perot-type resonance). Figs. 31 (b) and (c) demonstrate how the resonance behavior of the ring by itself is affected by the different values of capacitance of the varactor, since these capacitance values depend on the power level of the incident wave when the loaded ring

is inserted in the bilayered structure. In these two panels, the resonance behavior of the ring as characterized by its induced current when the ring is embedded in the waveguide filled with only the material with $\varepsilon_2 = 2\varepsilon_0$, and loaded with different values of capacitance of varactor is shown. The capacitance values, given in the captions, are selected based on the values that the varactor would have when the loaded ring is in the bilayered structure in the waveguide and is illuminated with the incoming wave in the forward and backward directions with different power levels. It is clear that for low power (5 dBm), the varactors are operating in their linear regime having almost the same value of capacitance for propagation in both directions and that there is only a very slight shift between the resonance frequencies positions (Fig. 31(b)), and consequently there is no pronounced difference in the transmission in both directions at the operating frequency. On the other hand, for the power of 30 dBm, the varactor capacitance values are different for different directions of propagation, leading to a major shift in resonance frequencies (Fig. 31(c)). The final transmission coefficient is influenced by both the resonance of the ring and the resonance of bilayered slab. The plots shown in Fig. 31 (b) and (c) are obtained using Time Domain Solver of CST Microwave Studio®. A waveguide port is used to excite the system with the TE_{10} mode of the waveguide using a power ranging from 3.126 mW (5 dBm) to 1 W (30 dBm). For each power level, the dynamic C (V) characteristics of the HBV is then plotted versus the induced voltage across the varactors exciting it from both ends of the waveguide, while sweeping over different values of capacitances. The operating point can then be found where the curves intersect (see Fig. 32, which is the plot for the 30 dBm power level). when the ring is

inside the waveguide filled with only the material with permittivity $\varepsilon_2 = 2\varepsilon_0$, and the value of capacitance of varactor is selected based on what it should be when the loaded ring is inserted in the bilayered dielectric slab and illuminated in the forward direction (when the capacitance is $C_f = 0.157pF$ for incident power level 5 dBm, and $C_f = 0.1pF$ for incident power level 30 dBm) and in the backward direction (when the capacitance is $C_b = 0.147pF$ for incident power level 5 dBm, and $C_b = 0.05pF$ for the power level 30 dBm). Fig. 31(b) and 31(c) show the resonance behavior of the ring when loaded with these various capacitance values. Fig. 31(d) is obtained when the ring is inserted in the waveguide with the bilayered dielectric slab present. A waveguide port is used to excite the system with the TE10 mode of the waveguide using a power ranging from 3.126 mW (5 dBm) to 1 W (30 dBm). For each power level, the dynamic C (V) characteristics of the HBV is then plotted versus the induced voltage across the varactors exciting it from both ends of the waveguide, while sweeping over different values of capacitances. The operating point can then be found where the curves intersect (see Fig. 32, which is the plot for the 30 dBm power level). These correspond to a negligible transmission coefficient for backward travelling wave and 0.42 for a forward travelling wave. The same approach is used to find the transmission coefficients in the forward and backward directions at every power level as shown in Fig. 31(d) where the ring is in the waveguide with the dielectric slabs present.

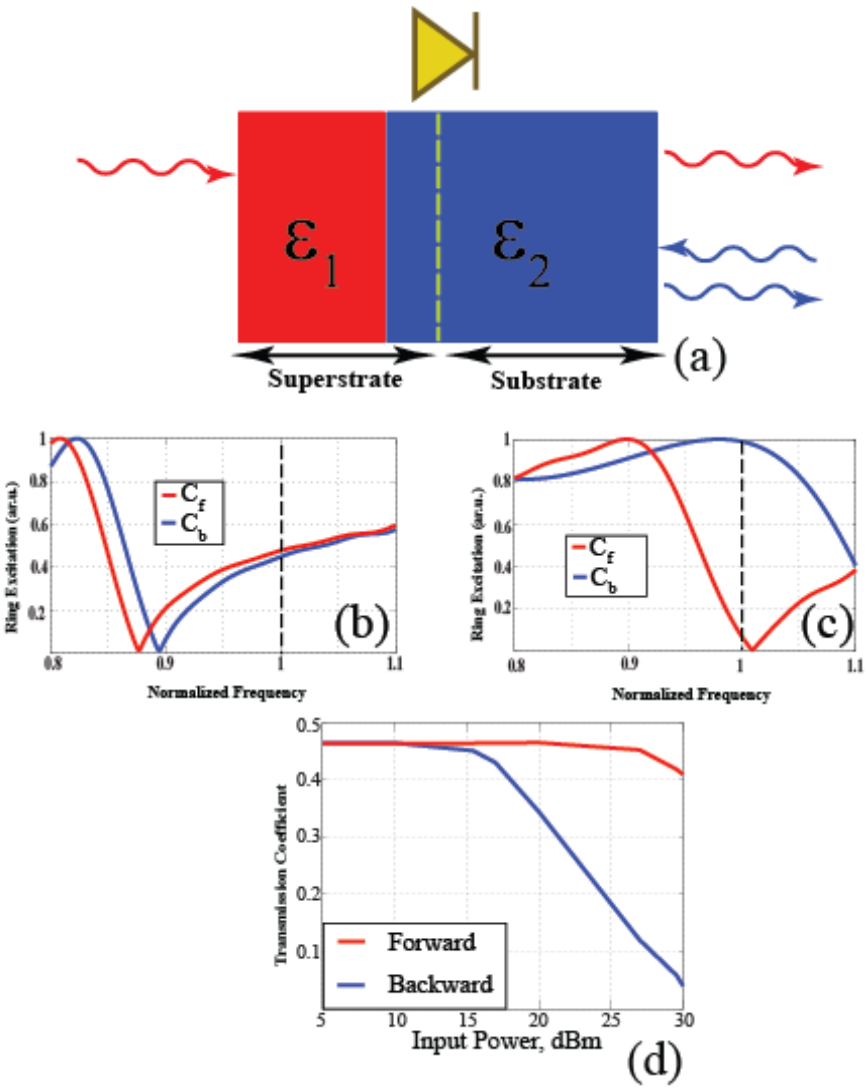

Fig. 31 Response of the nonlinearly loaded resonator ring and transmission coefficient of electromagnetic wave diode in the waveguide: *(a) Schematics of the wave diode. (b) The resonance behavior of the ring (i.e., its excited current in arbitrary units (ar.u.) vs normalized frequency (w.r.t. operating frequency), when the ring is located in the waveguide filled with material with* $\varepsilon_2 = 2\varepsilon_0$ *for two different values of varactor capacitance. These capacitance values,* $C_f = 0.157\,pF$ *and* $C_b = 0.147\,pF$*, are what the varactor experiences when the loaded*

ring in the bilayered structure and is illuminated with 5 dBm incident power in the forward (+z) and backward (-z) direction, respectively. In this case, we get almost the same excitation, which yields the same transmission characteristics for both. (c) Similar to (b), except the varactor capacitance values $C_f = 0.1pF$ *and* $C_b = 0.05pF$*, which are for the case of 30 dBm incident power. Here we note significant difference in the resonance of the ring for different capacitance values, yielding two different transmission coefficients at the operating frequency. (d) Transmission coefficient vs input power level. The red and blue curves show the cases of the forward and backward illuminations, respectively.*

Fig. 31(d) shows the calculated transmission coefficients in the structures for forward and backward directions of illumination at different incident power levels. We observe that for low power levels, the transmission properties for both directions of illumination are practically the same, and the structure has the transmission coefficient of about 0.462 for both cases symmetrically. With the increase of the incident power level we observe that a transmission for backward propagating wave is decreasing, whereas the transmission in a forward direction is practically not changing. For a 30 dBm incident power we already observe about 0.42 transmission coefficient for the forward illumination and a negligible transmission coefficient for the backward case. Moreover, the structure is robust towards changing the field polarization angle. This stability of the structure characteristics towards the change in the incident polarization is due to the symmetry of both the resonator structure, and the distribution of the nonlinear elements around the structure.

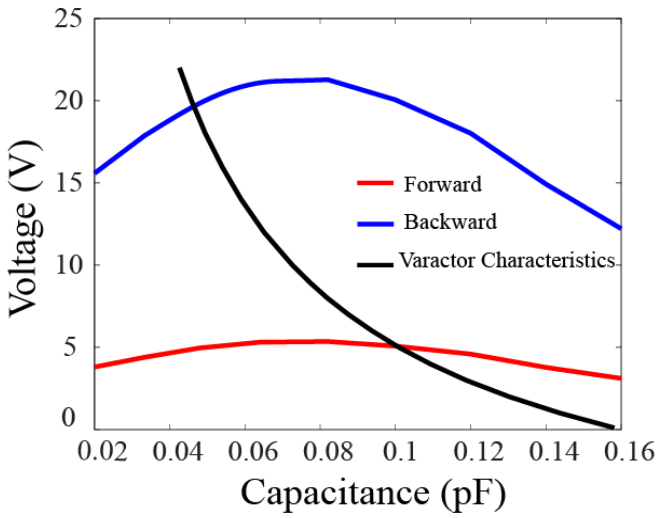

Fig. 32 Solution of the Nonlinear Problem, for an input power of 30 dBm*. The varactor's capacitance is swept over in the numerical simulator, and the induced voltage across the varactors is observed. The red and blue curves show the dependence of the voltage on the capacitance value of the varactors for the forward and the backward propagation, respectively. The black curve shows the C-V characteristics of the varactors. The points of intersection of the black curve with the red and the blue curves give the value of the capacitance which the varactor would exhibit in forward and backward directions, respectively*

We believe that our proposal of an efficient electromagnetic diode can find direct applications within various contexts and frequency regimes. For instance, we envision that our approach may be integrated efficiently within the Monolithic Microwave Integrated Circuits (MMIC's) platforms. Furthermore, our idea, when extended to the optical domain, may pave the way for efficient on chip optical logic circuitry and data processing.

The recent years have witnessed an astonishing progress in design of structures and systems that control and manipulate electromagnetic waves in desired fashions [11,127–130]. Of particular interest are ultrathin structures and composites, known as metasurfaces, that exhibit electromagnetic properties not readily attainable in nature [7,131,132]. The interest towards these systems has sparkled mostly due to a variety of promising applications in various ranges of electromagnetic spectrum: metasurfaces may be useful devices in today's microwave technology, where compact antennas, ultrathin layers with extreme chirality and asymmetric transmission, have been proposed and fabricated [133–135]; at optical frequencies metasurfaces may be the key towards the next generation of nanophotonics with various potential applications [131,132,136–138]; and even the THz and graphene-based technology is widely exploiting the metasurface principles [139–141].

Metasurfaces are usually constituted of regular metal and dielectric materials specifically crafted to give a desired electromagnetic response. It is the combination of the shape and dispersion properties of the inclusions that determines the properties of the whole system. Exploiting materials with nontrivial electromagnetic properties may significantly enhance the functionality and introduce new degrees of freedom for unprecedented features. For instance, gyrotropic materials that are sensitive to the magnetic biasing may be employed to tune and control the transmission properties of the system. More specifically, metastructures with gyrotropic properties exhibit time reversal asymmetry and may be exploited for nonreciprocal propagation and transmission, e.g. Faraday rotation of light polarization and asymmetric transmission for opposite directions of illumination – the latter is a property that is crucial for the electromagnetic wave

isolation [89,110,142–145]. In this framework developing all-passive metasurfaces that acquire efficient nonreciprocal behavior is of importance. Such systems may find broad range of applications from energy harvesting and light trapping in solar cells to nonreciprocal decoupling of transmitters and receivers within telecommunication and radar systems, and applications in image processing techniques. In section II we build upon the findings of section I and propose a paradigm for a quasi-2D metastructures that mimics the nonreciprocal property of Faraday rotation without using any magnetic or electric biasing.

3.9 Proposed concept of all-passive nonreciprocal metastructure

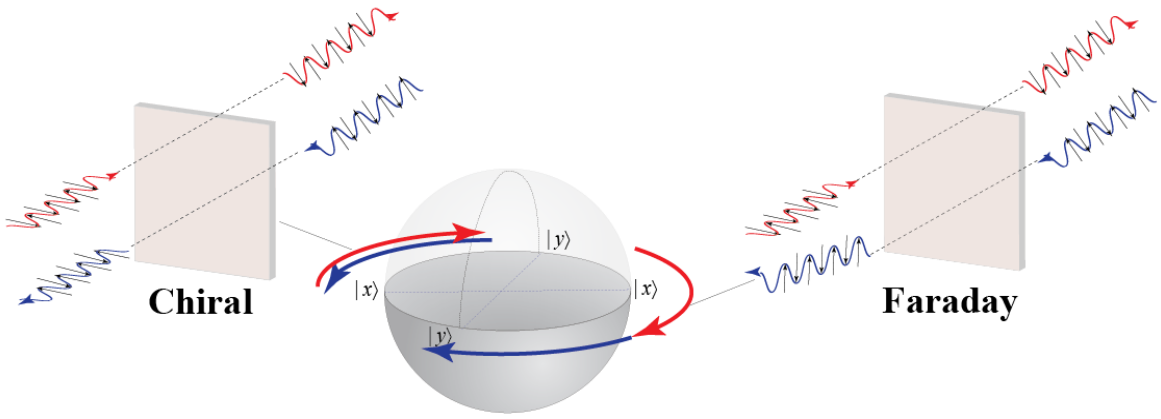

(a)

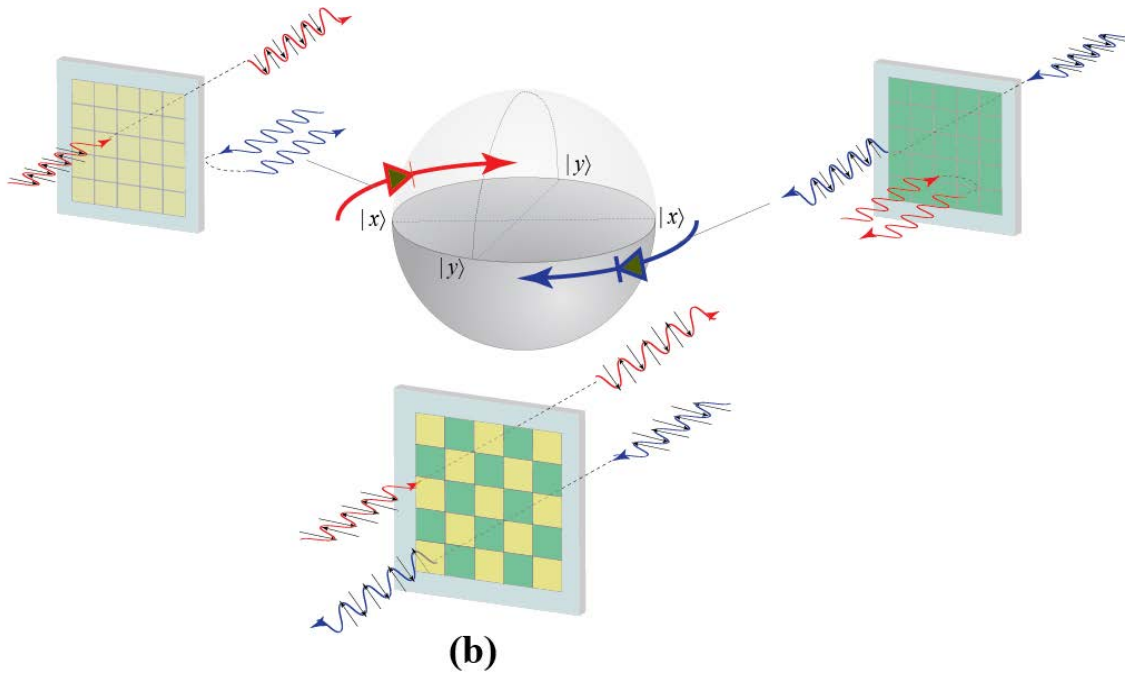

Fig. 33 Schematics of All-passive nonreciprocal metastructures*: (a) The difference between the 'reciprocal' polarization rotation due to chirality and the 'non-reciprocal' Faraday rotation phenomenon is shown, both mapped conceptually onto the Poincaré sphere. (b) Depending on the illumination direction of the incident wave, one of the two constituent designs (shown as green and yellow), acting as a "wave diode", allows the wave to go through, interacting with the chiral element (not shown) in the unit. Owing to this interaction, the plane of polarization of the wave rotates clockwise by nearly 90 degrees as it goes through this wave diode. The chiral elements in the diodes for waves going into the (+z) direction ("yellow" design) are mirror image of the chiral elements in the diodes for waves going into the (-z) direction ("green" design). The all-passive metastructure formed as the checkerboard pattern of such alternating designs may*

function as a nonreciprocal metasurface mimicking Faraday rotation, while no biasing electric or magnetic field is used.

Figure 33 shows the proposed concept. The metasurface unit cells consist of an all-passive electromagnetic "diode" (transmitting waves in one given direction only, which was discussed earlier) and a chiral element. We design the metastructure in a checkerboard fashion considering that two neighboring unit cells are mirror images of each other. Note that chiral elements in this case lead to the polarization rotation in the opposite directions, see Fig. 33. Consider illuminating the structure from one side. In this case only the unit cells with electromagnetic diodes allowing wave propagation would allow the wave to pass through. The wave in these cells would interact with the chiral structure and acquire a certain degree of polarization rotation (clockwise or counter-clockwise depending on the orientation of the chiral element in those units). On the other hand, illuminating the structure from the other side, the other set of unit "diode" cells will let the wave go through, but in these cells the chiral elements are the mirror-image of the other chiral element, thus leading to the rotation of the wave polarization in the same direction, which contrasts sharply with conventional chiral metamaterial structures and metasurfaces. Hence such a system would be mimicking the Faraday rotation of polarization. Clearly, the main challenge here is the design of an all-passive subwavelength electromagnetic diode with high performance characteristic which we have already addressed in a previous section.

3.10 Performance of proposed all-passive nonreciprocal metastructure

Having a building block that behaves as an electromagnetic diode exhibiting the intended relatively high throughput all-passive optical diode, we can proceed to investigating the intended all-passive quasi-2D metasurface that mimics the nonreciprocal behavior of Faraday rotation. For the sake of numerical proof of concept we choose the chiral structure in our unit cells to be the subwavelength bilayered chiral structures from Ref [146], which allows for almost 90^o polarization rotation with little reflection. A schematic of the unit cell constituting the metastructure (with two sub-unit cells as discussed before) is shown in Fig. 34(a). Fig. 34(b) shows a cross section of the electric field intensity distribution within the quasi-2D metastructure when illuminated with a plane wave that is linearly polarized along the x-direction and is propagating in the forward (+z) direction. Only the unit cells with the electromagnetic diode oriented to allow wave propagation in the (+z) direction are excited. As depicted in Fig. 34(c) the output's polarization in that case is a rotated version of the incident field's polarization. Illuminating the surface with a plane wave propagating in the opposite (i.e., backward (–z)) direction instead, only the unit cells with the electromagnetic diodes oriented such that to allow wave propagation in the (–z) direction are excited as shown in Fig 34(d). Since the chiral elements in these cells are mirror-image of the other chiral elements, we still get a rotated version of the incident wave, but with the same sense of rotation as the one obtained illuminating the surface from the other side as shown in Fig 34(e), mimicking the nonreciprocal Faraday rotation as required while no electric or magnetic bias is used.

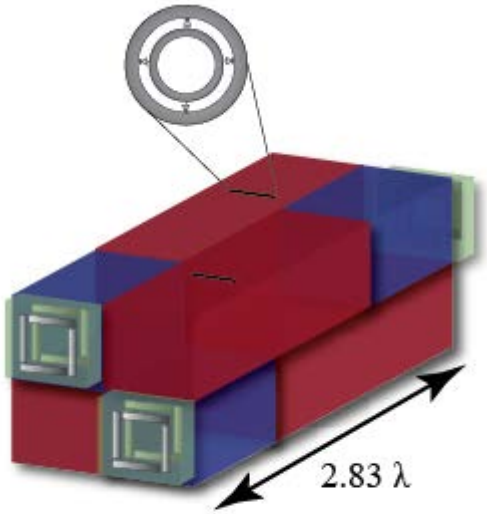

(a)

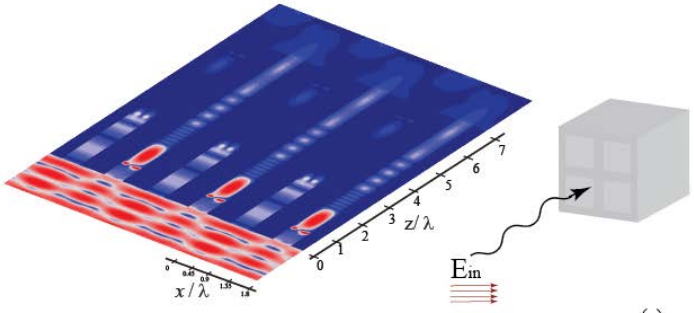

(b)

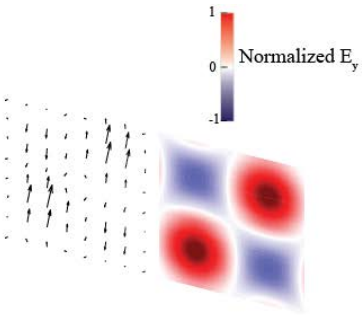

(c)

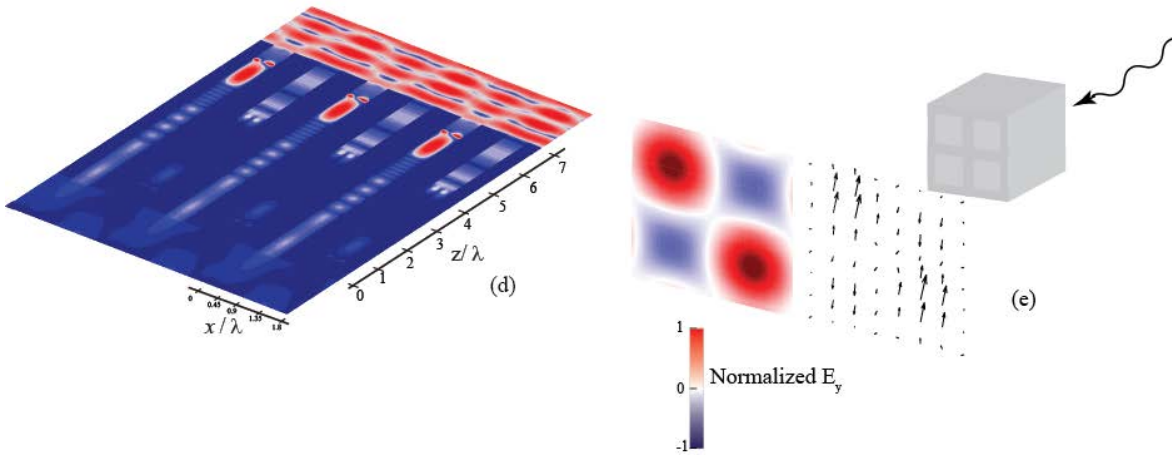

Fig. 34 Schematic of all-passive quasi-2D nonreciprocal metastructure*: (a) Geometry of the device with four units of the checkerboard including two pairs of mirror-imaged chiral elements shown in Fig. 33. (b) Cross section of the electric field intensity distribution within the metastructure with the incident wave propagating in the +z direction, (c) Simulation results for the output field (shown as compared with the incident field) when the incident wave propagates in the +z direction, (d) and (e) Similar to (b) and (c) but when the incident wave propagates in the -z direction.*

In conclusion, in this chapter we proposed a platform for all-passive metasurfaces with broken time-reversal symmetry. We investigated a systematic design procedure for achieving optical diode behavior without the usage of any sort of bias (neither magnetic nor electric) that is in principle applicable to any frequency regime. Moreover we

proposed a quasi-2D metastructure that mimics the non-reciprocal Faraday rotation phenomenon exhibiting high optical activity.

CHAPTER 4 Optical isolation with time-dependent materials in metal-insulator-metal waveguides

4.1 Introduction

It is well known that in order to achieve optical isolation, one needs to break the time-reversal symmetry. Based on the Lorentz reciprocity lemma, it is well known that the transmission symmetry may be broken within one of the following paradigms: magnetically active systems [88–90], systems exhibiting nonlinear response , and systems with time dependent material properties [9,91]. In bulk optics, optical isolation is usually achieved using materials exhibiting magneto-optical effects. Magneto-optical materials however prove to be difficult to integrate specially on a silicon photonics platform [147–149]. The lack of physical mechanisms for miniaturized integreable signal isolation has been a fundamental roadblock in integrated optics [150]. Thus, there has been intense interest for developing optical isolation schemes without using magneto-optical effects [105,111,151]. Nonlinearities have been exploited towards that goal as discussed in details in a previous chapter. On the other hand, a dynamic isolator using time-dependent materials was first proposed by Fan and his group [9]. Based on the effects of photonic transitions [152,153], it was shown that a linear, broadband and nonreciprocal isolation can be accomplished by spatio–temporal refractive index modulations that simultaneously causes frequency and wavevector shifts during the photonic transition process. This allows one-way light transmission while completely prohibiting the transmission of light signal in the opposite direction. This concept of time-dependent media and unidirectional nonreciprocal mode

conversion has been utilized and verified both theoretically [9] and experimentally [154] in the past in silicon waveguide environments. In this chapter we extend this concept into plasmonic Metal-Insulator-Metal (MIM) waveguides as depicted conceptually in fig. 35(a). Owing to the plasmonic nature of those waveguides we theoretically show that we can achieve optical isolation over a significantly smaller footprint than in the conventional silicon waveguide. Moreover, due to the plasmonic nature of the MIM waveguide and the interesting regimes in the dispersion relations we theoretically demonstrate that we can get a novel platform for complete wave flow isolation as we explain in the next sections.

4.2 Forward-Forward mode transition

Following a similar analysis to the one shown in [9] for a silicon slab waveguide in this section we investigate wave flow isolation in MIM waveguide. The MIM waveguide is constituted of a dielectric layer sandwiched between two metal layers as shown in the left panel of fig. 35(a). For such MIM waveguide, a supported TM mode has the following magnetic field distribution, depending on whether it is even or odd as shown in the inset of fig. 35(b) [155]:

$$H_{even} = \hat{z}H_0 e^{i\beta x}\begin{cases} \cosh(\sqrt{\beta^2 - k_d^2}\,\frac{d}{2})e^{-\sqrt{\beta^2-k_m^2}(y-\frac{d}{2})}, y > \frac{d}{2} \\ \cosh(\sqrt{\beta^2 - k_d^2}\,\frac{d}{2}), |\,y\,| < \frac{d}{2} \\ \cosh(\sqrt{\beta^2 - k_d^2}\,\frac{d}{2})e^{\sqrt{\beta^2-k_m^2}(y+\frac{d}{2})}, y < \frac{-d}{2} \end{cases} \quad (1)$$

$$H_{odd} = \hat{z}H_0 e^{i\beta x}\begin{cases} \sinh(\sqrt{\beta^2 - k_d^2}\,\frac{d}{2})e^{-\sqrt{\beta^2-k_m^2}(y-\frac{d}{2})}, y > \frac{d}{2} \\ \sinh(\sqrt{\beta^2 - k_d^2}\,\frac{d}{2}), |\,y\,| < \frac{d}{2} \\ -\sinh(\sqrt{\beta^2 - k_d^2}\,\frac{d}{2})e^{\sqrt{\beta^2-k_m^2}(y+\frac{d}{2})}, y < \frac{-d}{2} \end{cases} (2)$$

Moreover, the guided-wave number β satisfies the following dispersion relations for even and odd modes, respectively [156]:

$$Tanh[\sqrt{\beta^2 - k_d^2}\,\frac{d}{2}] = -\frac{\varepsilon_0}{\varepsilon_d}\frac{\sqrt{\beta^2 - k_m^2}}{\sqrt{\beta^2 - k_d^2}} \quad (3)$$

$$Coth[\sqrt{\beta^2 - k_d^2}\,\frac{d}{2}] = -\frac{\varepsilon_0}{\varepsilon_d}\frac{\sqrt{\beta^2 - k_m^2}}{\sqrt{\beta^2 - k_d^2}} (4)$$

In our analysis, the relative permittivity of the dielectric region ε_d is chosen to be 2, the relative permittivity of the metal ε_m is defined by a Drude model as $1-(\frac{f_p^2}{f})$ with $f_p = 760THz$. Consequently, $k_d = \frac{\omega}{c}\sqrt{\varepsilon_d}$ and $k_m = \frac{\omega}{c}\sqrt{\varepsilon_m}$. The height of the waveguide d is chosen to be $0.25\mu m$.. Worth mentioning here is that a lossless medium was assumed for the simplicity of discussion.

Such a waveguide possesses a band structure as shown in Fig. 35(b), with symmetric and antisymmetric modes located in the first and second bands, respectively. As originally

suggested by Fan and his group, an interband transition between modes with frequencies and wavevectors (ω_1, β_1) , and (ω_2, β_2) located in these two bands, can be induced by modulating the waveguide with an additional dielectric perturbation as in [9]. We choose ω_1 to be 370 THz, and ω_2 to be 380 THz. Consequently β_1 and β_2 are equal to 17.437 Mrad/m and 7.47 Mrad/m respectively. Such modulation would lead to an interband transition in the forward direction that is in turn not allowed in the backward direction. This is depicted in fig. 35(b) using the black arrows. Following the technique used in [9] , the electric field can be written as follows

$$\overrightarrow{E} = E_x \hat{x} + E_y \hat{y} \quad (5)$$

$$E_x = \left(\frac{a_1 E_{1x}}{2} e^{i(-\beta_1 x + \omega_1 t)} + \frac{a_1^* E_{1x}^*}{2} e^{-i(-\beta_1 x + \omega_1 t)} + \frac{a_2 E_{2x}}{2} e^{i(-\beta_2 x + \omega_2 t)} + \frac{a_2^* E_{2x}^*}{2} e^{-i(-\beta_2 x + \omega_2 t)}\right) \quad (6)$$

$$E_y = \left(\frac{a_1 E_{1y}}{2} e^{i(-\beta_1 x + \omega_1 t)} + \frac{a_1^* E_{1y}^*}{2} e^{-i(-\beta_1 x + \omega_1 t)} + \frac{a_2 E_{2y}}{2} e^{i(-\beta_2 x + \omega_2 t)} + \frac{a_2^* E_{2y}^*}{2} e^{-i(-\beta_2 x + \omega_2 t)}\right) \quad (7)$$

Where E_1 and E_2 are the modal profiles for the even and odd modes, respectively, normalized such that $|a_n|^2$ is the photon number flux carried by the nth mode.

The modulated permittivity of the dielectric can be written as follows [9]

$$\varepsilon_{\text{mod}} = \varepsilon_0 \left(\varepsilon_d + \frac{\partial \varepsilon}{2} e^{i(-k_{\text{mod}} x + \Omega_{\text{mod}} t)} + \frac{\partial \varepsilon}{2} e^{-i(-k_{\text{mod}} x + \Omega_{\text{mod}} t)}\right) \quad (8)$$

To maximize the coupling strength, by keeping the maximum possible field profile overlap between the even and odd modes, the modulation region was chosen to occupy half the waveguide width as shown in Fig. 35(a) [9]. By substituting eqs(5-8) into

Maxwell's equation and using perturbation theory assuming slow envelope variation, the following coupled mode equation can be derived

$$\frac{d}{dx}\begin{pmatrix} a_1 \\ a_2 \end{pmatrix} = \begin{pmatrix} 0 & i\dfrac{B}{A} \\ i\dfrac{D}{C} & 0 \end{pmatrix}\begin{pmatrix} a_1 \\ a_2 \end{pmatrix} \quad (9)$$

$$A = \int_{-\infty}^{\infty} (E_{y1}H_{z1}^{*} + H_{z1}E_{y1}^{*})dy \qquad (10)$$

$$B = \frac{1}{2}\varepsilon_0(\omega_2 - \Omega_{\text{mod}})\delta\varepsilon \int_{-\frac{d}{2}}^{0} (2E_{x1}E_{x2}^{*})dy \quad (11)$$

$$C = \int_{-\infty}^{\infty} (E_{y2}H_{z2}^{*} + H_{z2}E_{y2}^{*})dy \qquad (12)$$

$$D = \frac{1}{2}\varepsilon_0(\omega_1 + \Omega_{\text{mod}})\delta\varepsilon \int_{-\frac{d}{2}}^{0} (2E_{x2}E_{x1}^{*})dy \quad (13)$$

With an initial condition $a_1(0) = 1$ and $a_2(0) = 0$, the solution to equation (9) is $a_1 = \cos(\kappa z)$, and $a_2 = \sin(\kappa z)$, where $\kappa = \sqrt{\dfrac{BD}{CA}}$.

The electromagnetic field energy carried by mode 1 (even mode) will make a complete transition to mode 2 (odd mode) after propagating over a distance of coherence length $L_c = \dfrac{\pi}{2|\kappa|}$. Using the chosen parameters, with modulation depth $\partial\varepsilon = 0.1$ L_c is $5.69\mu m$.

Thus cascading the modulated waveguide by a notch filter at ω_2 would lead to the

intended waveflow isolation as depicted schematically in fig. 35(a). Fig. 35(c) shows the magnetic fields distribution that was analytically derived using perturbation theory, with continuous-wave (CW) excitation at ω_1 . The arrows represent the direction of incidence and the black rectangle indicates the modulated waveguide region. Exciting the structure from the left side at frequency ω_1 by the even mode as shown in the top panel, and after propagating through L_c the electromagnetic energy would be transferred into ω_2 carried by the odd mode, and by simply having a notch filter at ω_2 the energy flow is prohibited in that direction. The bottom panel of fig. 35(c) shows the magnetic field profile when exciting the structure from the right. In that direction, the electromagnetic energy is preserved in the even mode at ω_1 and thus coupled into the output unperturbed.

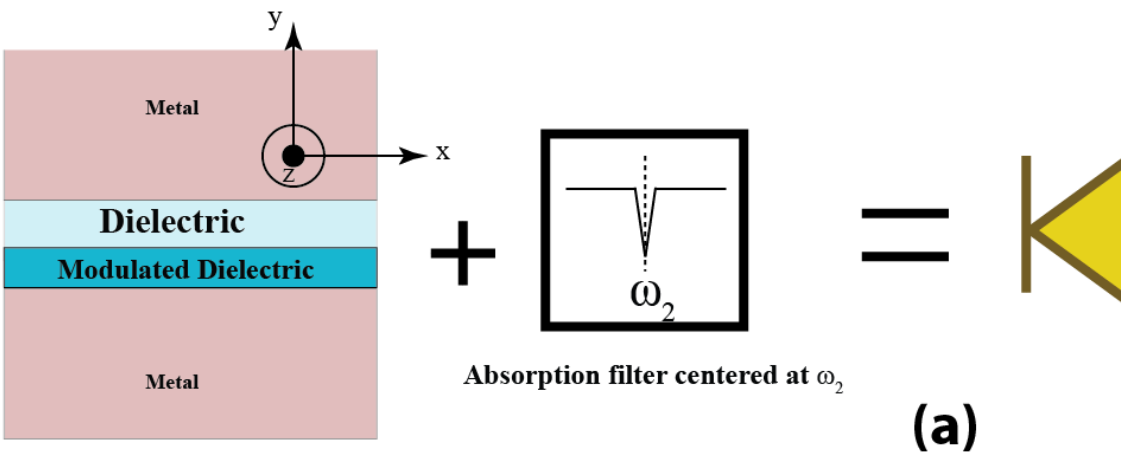

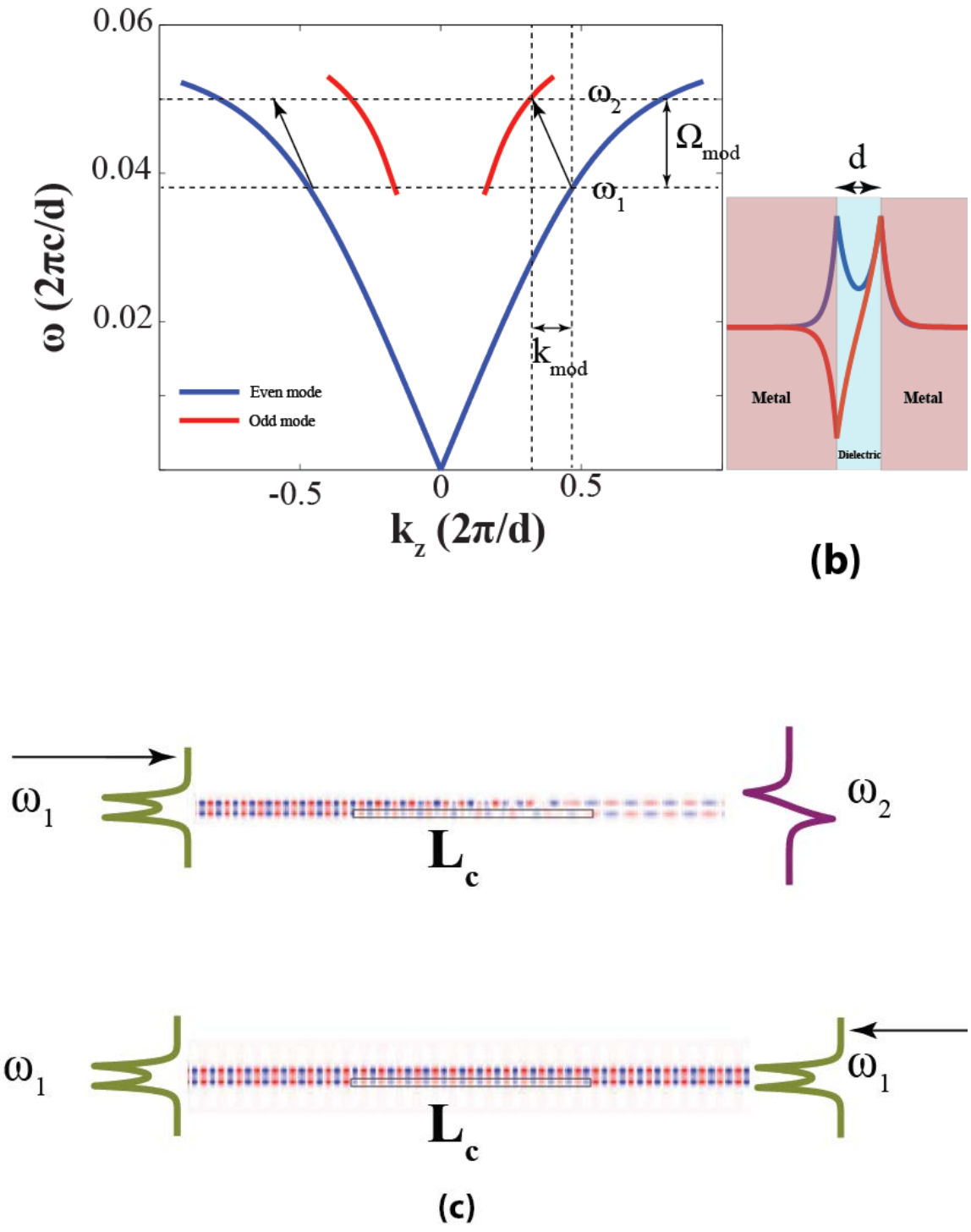

Fig. 35 Investigating waveflow isolation in plasmonic metal-dielectric-metal

***waveguides using spatio-temporal modulation (forward-forward mode transition)**, (a) Schematic of the proposed platform for wave flow isolation by modulating the dielectric spacer in a MIM waveguide cascading it with an absorption filter at ω_2[9]. (b) Conventional dispersion relations for MIM waveguide for the first TM even (blue) and odd (red) modes. The black arrows show the indirect photonic transition that is allowed only for one direction of propagation. The inset shows the magnetic field distributions for the even (blue) and the odd (red) modes. (c) Distribution of magnetic fields analytically derived using perturbation theory, with continuous-wave excitation at ω_1 . The arrows represent the direction of incidence and the black rectangle indicates the modulated waveguide region.*

4.3 Forward-Backward mode transition

In this section, we further investigate this platform we briefly reviewed in the previous section, and reveal an interesting regime for wave flow isolation. It has been shown that if the height of MIM waveguide is brought thinner, the odd mode dispersion relation exhibits a negative slope, i.e. there exists regimes where the energy flow direction and the wavenumber direction have opposite signs, a scenario analogous to what is observed in negative index materials. In that case we are able to achieve true waveflow isolation, omitting the need for the absorption filter as shown schematically in fig. 36(a). In our analysis, the relative permittivity of the dielectric ε_d is chosen to be 6.25, the relative permittivity of the metal ε_m is defined by a Drude model as $1-(\frac{f_p^2}{f})$

with $f_p = 2000THz$. Consequently, $k_d = \frac{\omega}{c}\sqrt{\varepsilon_d}$ and $k_m = \frac{\omega}{c}\sqrt{\varepsilon_m}$. The height of the waveguide d is chosen to be $15nm$. The band structure for using these parameters is shown in fig. 36(b), where clearly the odd mode exhibits the negative slope behavior discussed before. Intuitively, we can explain the performance of that structure as follows: Let's say we start with the even mode at $z = 0$ propagating in the positive z direction. For this mode both β and the energy flow direction share the same sign. If we properly choose the modulation parameters for the dielectric to achieve an interband transition as shown in fig. 36(b), the energy would be continuously transferring from the even mode to the odd mode, whose energy flow direction is the backward z direction.

In this scenario, unlike the case discussed earlier, the term $\frac{BD}{CA}$ turns out to be always negative, implying that the instead of the sinusoidal solution, we end up with exponential decay of the even mode into the odd mode as it propagates through the waveguide. Thus in such scenario, exciting the structure from one side (let's say $+z$ direction) at ω_1 the electromagnetic energy would be continuously couples into the odd mode at ω_2. This electromagnetic energy carried by the odd mode would be travelling into $-z$ direction because of the negative group velocity that is obvious from fig. 36(b). On the other hand, exciting the structure from the other side (into $-z$ direction), the electromagnetic energy carried by the even mode at ω_1 would go through unperturbed. Thus, optical isolation can be indeed achieved while omitting the need for the notch filter at ω_2.

Another interesting platform to consider is the pair of graphene sheets. Owing to the relatively easy modulation of graphene sheets' conductivities by simply applying an

electrical voltage we expect that this platform, with further optimization and design, can offer a promising domain for waveflow isolation and consequently more necessary functionalities for photonic circuits. As shown in the left panel of fig. 37, having 2 sheets of graphene we can constitute a parallel plate waveguide. The modulation scheme would be based on an alternating voltage can be applied to one of the sheets. By investigating the dispersion relations we can conclude that an analogous modulation scheme for the conductivity of the graphene sheet may lead to unidirectional mode conversion and consequently waveflow isolation when cascaded by a notch filter at ω_2 as discussed in a previous section. This opens the door for novel platforms in which optical isolation is achievable in graphene based waveguides, whose modulation is much easier than conventional silicon based waveguides.

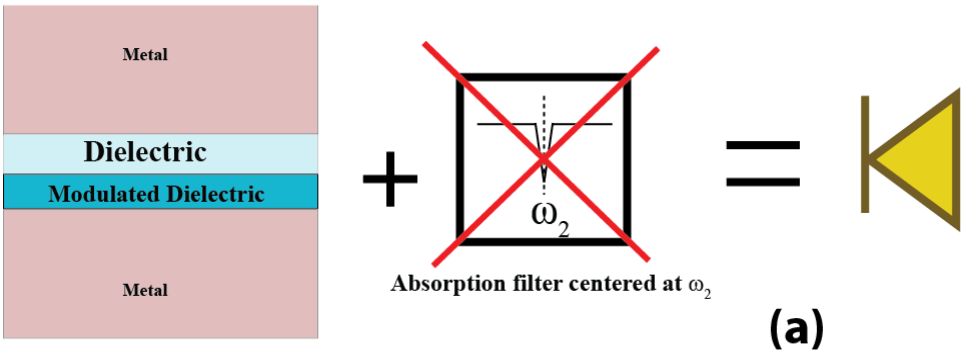

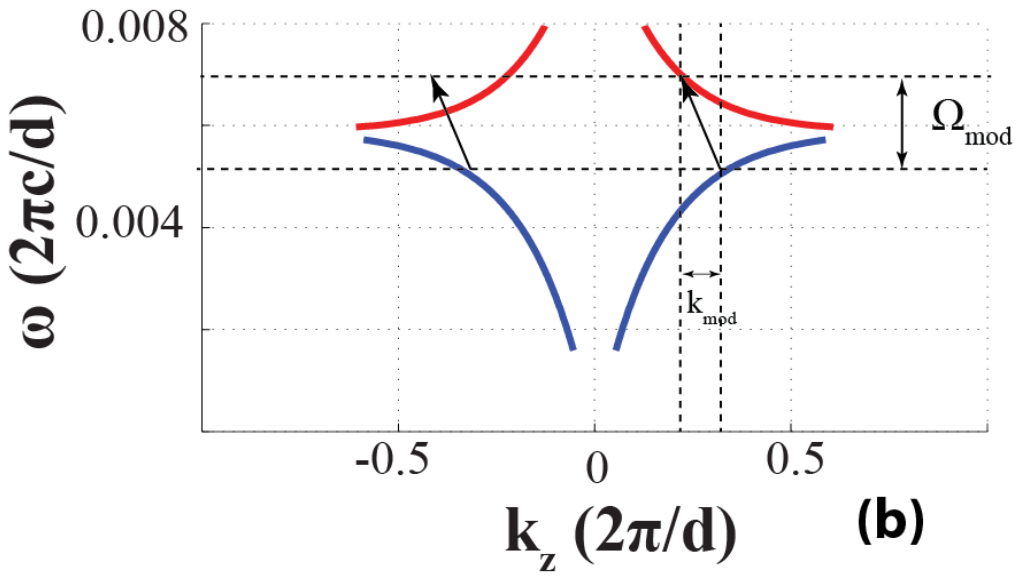

Fig. 36 Investigating waveflow isolation in plasmonic metal-dielectric-metal waveguides using spatio-temporal modulation (forward-backward mode transition) *(a) Schematic of the proposed platform for waveflow isolation by modulating the dielectric spacer in a MIM waveguide to achieve an indirect photonic transition from the forward even mode (blue) at* ω_1 *to the backward odd mode (red) at* ω_2*. (b) Dispersion relations for MIM waveguide for the first TM even (blue) and odd (red) modes. The black arrows show the indirect photonic transition that is allowed only for one direction of propagation.*

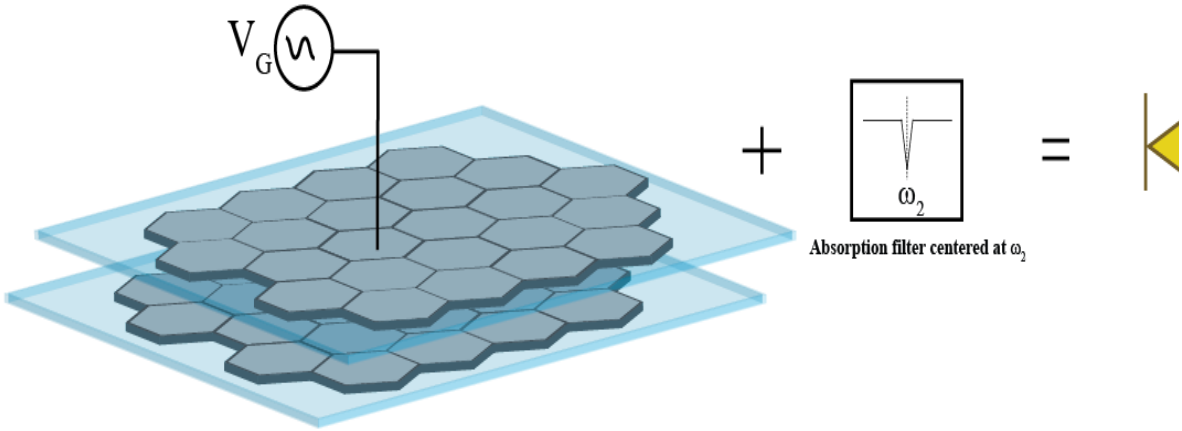

Fig. 37 Schematic of the proposed platform for wave flow isolation by modulating the conductivity of a graphene sheet in a graphene parallel plate waveguide

Chapter 5: Conclusion

In this dissertation, we investigated several research topics with the vision of proposing new techniques and roadmaps to narrow the gap between the electronic and the electromagnetic systems and open the door for further integrtation between these two fields, aiming for exciting features and performances in various applications and fields [4]. We explored the notion of "static optics", in which the electricity and magnetism are spatially decoupled and have their fields statically distributed, while being temporally dynamic. Having both permittivity and permeability approaching zero leads to a scenario with interesting possibilities . We investigated some of the unprecedented features that are exhibited within epsilon-and-mu near-zero (EMNZ) media, i.e., structures with both the relative permittivity and permeability near zero. In particular, we showed that using an EMNZ medium one might in principle "open up" and "stretch" the space, and have regions behaving as "single electromagnetic point" despite conventionally being electrically large. We also explored analytically and numerically that we can achieve electromagnetic invisibility of arbitrarily-shaped, electrically large, perfectly electric conducting objects when embedded in an EMNZ medium owing to the unusual scattering properties within an EMNZ medium. Moreover, we investigated some of the unusual effects that accompany placing classically radiating dipoles in the presence of an EMNZ medium. We believe that this will open doors to manipulating and engineering the radiation performance of more complicated systems like quantum emitters offering environments within which quantum effects including (among others) super-radiance and

coherence might be taken beyond conventionally known limits [157]. We suggested a possible implementation of a structure that would exhibit an EMNZ behavior and demonstrated the possibility of having electrically large volumes to behave as EMNZ media and experimentally verified our proposal in the microwave regime. The proposed structure was constituted of metallic waveguide designed to achieve a host medium whose effective permittivity approaches zero at the design frequency. Loading this waveguide with a properly designed dielectric rod allows for having an effective permeability being near zero as well. We envision that these ideas would open doors for geometry invariant cavities [158], a concept that would have unprecedented applications.

We have also investigated novel nonreciprocal platforms and we proposed several ideas and concepts that can be used towards having more integreable photonics. We explored a method for designing unidirectional structures that allow transmission of electromagnetic signals in one direction and prohibit it in the other direction exhibiting the diode-like behavior. We adopted a new approach that makes use of nonlinear elements or materials incorporated in planar resonant structures embedded into a spatially asymmetric structure to achieve such behavior. Since the structure is asymmetric in the wave flow direction, although being reciprocal, and obviously would exhibit the same transmission characteristics being fed from either side, the field distribution within that structure would however depend on the side from which it is being fed. Thus, by placing nonlinear elements or materials whose properties depend on the local field at some appropriate positions where the local field is significantly dependent on the side from which the structure is fed, we could consequently observe a significant difference in the

properties of those elements or materials, which then could be incorporated into a planar resonant structure to manipulate the direction-dependent transmission characteristics [7,8]. The main advantage of this approach is that this field profile asymmetry is not specific to a subset of the spectrum; the phenomenon is rather general, in the sense that it can be designed for and used at any frequency regime. Consequently the diode-like behavior is conceptually achievable just by designing appropriate nonlinearly loaded planar or quasi planar resonant structures that are suitable for the frequency regime of interest and locating them at a plane with high field asymmetry. Moreover we built upon those findings and proposed a metastructure that mimics the nonreciprocal phenomenon of Farady rotation in an all-passive fashion, omitting the need for any sort of bias (magnetic or electric) [7,8]. We envision that this may open doors for more functionalities within the field of metasurfaces and metastructures by incorporating nonlinearities to achieve unprecedented performances.

We also explored another platform for achieving electromagnetic isolation within time-dependent environements. It has been shown that temporal refractive index modulation of photonic structures can cause photon states to go through interband transitions analogous to electronic states in semiconductors [159]. Based on that fact it was shown that complete optical isolation can be achieved by inducing indirect photonic transitions in a silicon waveguide. We exploited the high confinement ability of metal-dielectric-metal waveguide and show theoretically that we can achieve optical isolation over a significantly smaller footprint. We showed numerically that by choosing a spatio-temporally varying modulation scheme that simultaneously induces the required

frequency and momentum shifts of photon states during the transition process, the transmission behavior of the structure becomes non-reciprocal. Moreover we proposed the possibility of achieving the optical isolation while omitting the need for the absorptive filters by designing that structure to exhibit frequency band in its dispersion diagrams where it supports a mode whose group and phase velocity acquire different signs.

Bibliography

1. Akimov, Y. A., Koh, W. S. & Ostrikov, K. Enhancement of optical absorption in thin-film solar cells through the excitation of higher-order nanoparticle plasmon modes. **17,** 10195–10205 (2009).

2. Liu, Z., Lee, H., Xiong, Y., Sun, C. & Zhang, X. Far-Field Optical Hyperlens Magnifying Sub-Diffraction-Limited Objects. *Science*, **315,** 1686 (2007).

3. Feng, J. *et al.* Nanoscale Plasmonic Interferometers for Multispectral, High-Throughput Biochemical Sensing. *Nano Lett.* **12,** 602–609 (2012).

4. Mahmoud, A. M. & Engheta, N. Wave-matter interactions in epsilon-and-mu-near-zero structures. *Nat. Commun.* **5,** 5638 (2014).

5. Ziolkowski, R. W. Propagation in and scattering from a matched metamaterial having a zero index of refraction. *Phys. Rev. A* **70,** 046608 (2004).

6. Huang, X., Lai, Y., Hang, Z. H., Zheng, H. & Chan, C. T. Dirac cones induced by accidental degeneracy in photonic crystals and zero-refractive-index materials. *Nat. Mater.* **10,** 582–586 (2011).

7. Mahmoud, A. M., Davoyan, A. R. & Engheta, N. Nonreciprocal passive metastructure without magnetic bias. *2013 IEEE Antennas Propag. Soc. Int. Symp.* 496–497 (2013).

8. Mahmoud, A. M., Davoyan, A. R. & Engheta, N. All-passive nonreciprocal metastructure. *Nat. Commun.* **6,** 1–7 (2015).

9. Yu, Z. & Fan, S. Complete optical isolation created by indirect interband photonic transitions. *Nat. Photonics* **3,** 91–94 (2009).

10. Pendry, J. Negative Refraction Makes a Perfect Lens. *Phys. Rev. Lett.* **85,** 3966–3969 (2000).

11. Alù, A. & Engheta, N. Achieving transparency with plasmonic and metamaterial

coatings. *Phys. Rev. E* **72,** 016623 (2005).

12. Alekseyev, L. V & Narimanov, E. Slow light and 3D imaging with non-magnetic negative index systems. *Opt. Express* **15,** 11184–11193 (2006).

13. Yuan, H. *et al.* A negative permeability material at red light. *Opt. Express* **15,** 1076–1083 (2007).

14. Veselago, V. G. The electrodynamics of substances with simultenously negative values of ε and μ. *Sov. Phys. USP* **10,** 509–514 (1964).

15. Alù, A., Silveirinha, M., Salandrino, A. & Engheta, N. Epsilon-near-zero metamaterials and electromagnetic sources: Tailoring the radiation phase pattern. *Phys. Rev. B* **75,** 155410 (2007).

16. Lovat, G. *et al.* Analysis of Directive Radiation From a Line Source in a Metamaterial Slab With Low Permittivity. *IEEE Trans. Antennas Propag.* **54,** 1017–1030 (2006).

17. Enoch, S., Tayeb, G., Sabouroux, P., Guerin, N. & Vincent, P. A Metamaterial for Directive Emission. *Phys. Rev. E* **89,** 213902 (2002).

18. Bahl, I. J. & Gupta, K. C. A Leaky-Wave Antenna Using an Artificial Dielectric Medium. *IEEE Trans. Antennas Propag.* **22,** 119–122 (1974).

19. Zhou, H. *et al.* A High-Directive Patch Antenna Based on All-Dielectric Near-Zero-Index Metamaterial Superstrates. *J. Electromagn. Waves Appl.* **24,** 1387–1396 (2010).

20. Yang, J., Huang, M. & Peng, J. Directive Emission Obtained by Mu and Epsilon-Near-Zero Metamaterials. *RADIOENGINEERING* **18,** 124–128 (2009).

21. Alù, A., Bilotti, F., Engheta, N. & Vegni, L. Metamaterial Covers Over a Small Aperture. **54,** 1632–1643 (2006).

22. Soric, J. C., Engheta, N., Maci, S. & Alù, A. Omnidirectional Metamaterial Antennas Based on ε-Near-Zero Channel Matching. *IEEE Trans. Antennas*

Propag. **61,** 33–44 (2013).

23. Jin, Y. & He, S. Enhancing and suppressing radiation with some permeability-near-zero structures. *Opt. Express* **18,** 16587–16593 (2010).

24. Silveirinha, M. & Engheta, N. Tunneling of Electromagnetic Energy through Subwavelength Channels and Bends using ε-Near- Zero Materials Tunneling of Electromagnetic Energy through Subwavelength Channels. *Phys. Rev. Lett.* **97,** 157403 (2006).

25. Silveirinha, M. & Engheta, N. Design of matched zero-index metamaterials using nonmagnetic inclusions in epsilon-near-zero media. *Phys. Rev. B* **75,** 075119 (2007).

26. Alù, A. & Engheta, N. Dielectric sensing in ε -near-zero narrow waveguide channels. *Phys. Rev. B* **78,** 045102 (2008).

27. Pan, Y. & Xu, S. Energy tunnelling through an ultrasmall epsilon-near-zero channel in circular waveguide. *IET Microwaves, Antennas Propag.* **3,** 821–825 (2009).

28. Marcos, S., Silveirinha, G. & Engheta, N. μ -near-zero supercoupling. *Phys. Rev. B* **91,** 195112 (2015).

29. Alù, A. & Engheta, N. Coaxial-to-Waveguide Matching With ε-Near-Zero Ultranarrow Channels and Bends. *IEEE Trans. Antennas Propag.* **58,** 328–339 (2010).

30. Luo, J., Xu, P., Gao, L., Lai, Y. & Chen, H. Manipulate the Transmissions Using Index-Near-Zero or Epsilon-Near-Zero Metamaterials with Coated Defects. *Plasmonics* **7,** 353–358 (2012).

31. Hao, J., Yan, W. & Qiu, M. Super-reflection and cloaking based on zero index metamaterial. **96,** 101109 (2010).

32. Nguyen, V. C., Chen, L. & Halterman, K. Total Transmission and Total Reflection by Zero Index Metamaterials with Defects. *Phys. Rev. Lett.* **105,** 233908 (2010).

33. Xu, Y. & Chen, H. Total reflection and transmission by epsilon-near-zero metamaterials with defects. *Appl. Phys. Lett.* **98,** 113501 (2011).

34. Sun, L., Feng, S. & Yang, X. Loss enhanced transmission and collimation in anisotropic epsilon-near- zero metamaterials. *Appl. Phys. Lett.* **101,** (2012).

35. Feng, S. Loss-Induced Omnidirectional Bending to the Normal in ε-Near-Zero Metamaterials. *Phys. Rev. Lett.* **108,** 193904 (2012).

36. Luo, J. *et al.* Realizing almost perfect bending waveguides with anisotropic epsilon-near-zero metamaterials. *Appl. Phys. Lett.* **100,** 221903 (2012).

37. Ma, H. F., Shi, J. H., Cai, B. G. & Cui, T. J. Total transmission and super reflection realized by anisotropic zero-index materials. *New J. Phys.* **14,** 123010 (2012).

38. Powell, D. A. *et al.* Nonlinear control of tunneling through an epsilon-near-zero channel. *Phys. Rev. A* **79,** 245135 (2009).

39. Ciattoni, A., Rizza, C. & Palange, E. Extreme nonlinear electrodynamics in metamaterials with very small linear dielectric permittivity. *Phys. Rev. A* **81,** 043839 (2010).

40. Argyropoulos, C., Chen, P.-Y., D'Aguanno, G., Engheta, N. & Alù, A. Boosting optical nonlinearities in ε-near-zero plasmonic channels. *Phys. Rev. B* **85,** 045129 (2012).

41. Naik, G. V, Kim, J. & Boltasseva, A. Oxides and nitrides as alternative plasmonic materials in the optical range [Invited]. *Opt. Mater. Express* **1,** 1090–1099 (2011).

42. Vesseur, E. J. R., Coenen, T., Caglayan, H., Engheta, N. & Polman, A. Experimental Verification of n=0 Structures for Visible Light. *Phys. Rev. Lett.* **110,** 013902 (2013).

43. Maas, R., Parsons, J., Engheta, N. & Polman, A. Experimental realization of an epsilon-near-zero metamaterial at visible wavelengths. *Nat. Photonics* **7,** 907–912

(2013).

44. Zhou, L., Song, Z., Huang, X. & Chan, C. T. Physics of the zero- n photonic gap: fundamentals and latest developments. *Nanophotonics* **1,** 181–198 (2012).

45. Li, Y. *et al.* On-chip zero-index metamaterials. *Nat. Photonics* **9,** 738–743 (2015).

46. Zhou, R., Zhang, H. & Xin, H. Metallic Wire Array as Low-Effective Index of Refraction Medium for Directive Antenna. *IEEE Trans. Antennas Propag.* **58,** 79–87 (2010).

47. He, Q., Xiao, S., Li, X. & Zhou, L. Optic-null medium : realization and applications. *Opt. Express* **21,** 28948–28959 (2013).

48. Monti, A., Bilotti, F., Toscano, A. & Vegni, L. Possible implementation of epsilon-near-zero metamaterials working at optical frequencies. *Opt. Commun.* **285,** 3412–3418 (2012).

49. Sun, L. & Yu, K. W. Strategy for designing broadband epsilon-near-zero metamaterials. *J. Opt. Soc. Am. B* **29,** 984–989 (2012).

50. Rizza, C., Di Falco, A. & Ciattoni, A. Gain assisted nanocomposite multilayers with near zero permittivity modulus at visible frequencies. **99,** 221107 (2011).

51. Lindell, I. V. & Sihvola, A. H. Electromagnetic boundary and its realization with anisotropic metamaterial. *Phys. Rev. E* **79,** 026604 (2009).

52. Lindell, I. V. & Sihvola, A. H. Zero- Axial-Parameter (ZAP) Medium Sheet. *PIER* **89,** 213–224 (2009).

53. Lindell, I. V. & Sihvola, A. H. Soft-and-Hard / D' B' Boundary Condition and its Realization by Electromagnetic Media. *IEEE Trans. Antennas Propag.* **61,** 478–482 (2013).

54. Fleury, R. & Alù, A. Enhanced superradiance in epsilon-near-zero plasmonic channels. *Phys. Rev. B* **87,** 201101 (2013).

55. Rotman, W. Plasma Simulation by Artificial Dielectrics and Parallel-Plate Media. *IRE Trans. Antennas Propag.* **10,** 82–95 (1962).

56. Rakić, A. D., Djurišić, A. B., Elazar, J. M. & Majewski, M. L. Optical properties of metallic films for vertical-cavity optoelectronic devices. *Appl. Opt.* **37,** 5271–5283 (1998).

57. Bykov, V. . P. Spontaneous emission from a medium with a band spectrum. *Sov. J. Quantum Electron* **4,** 861–871 (1975).

58. Krauss, T. F., De La Rue, R. M. Two-diemnsional photonic-bandgap structures operating at near-infrared wavelengths. *Nature* **383,** 699–702 (1996).

59. Yablonovitch, E. Inhibited Spontaneous Emission in Solid-State Physics and Electronics. **58,** 2059–2062 (1987).

60. Ohtaka, K. Energy band of photons and low-energy photon diffraction. *Phys. Rev. B* **19,** 5057–5067 (1979).

61. Qiu, M. & He, S. Large complete band gap in two-dimensional photonic crystals with elliptic air holes. *Phys. Rev. B* **60,** 610–612 (1999).

62. John, S. Strong Localization of Photons in Certain Disordered Dielectric Superlattices. *Phys. Rev. Lett.* **58,** 2486–2489 (1987).

63. Yablonovitch, E., Gmitter, T. J., Leung, K. M. Photonic Band Structure: The Face-Centered-Cubic Case Employing Nonsperical Atoms. *Phys. Rev. Lett.* **67,** 2295–2298 (1991).

64. Bykov, V. P. Spontaneous Emission in a Periodic Structure. *Sov. J. Exp. Theor. Phys.* **35,** 269–273 (1972).

65. Rayleigh, L. On the Remarkable Phenomenon of Crystalline Reflexion described by Prof. Stokes. *Phil. Mag* **26,** 256–265 (1888).

66. Fink, Y. *et al.* A Dielectric Omnidirectional Reflector. *Science*, **282,** 1679–1682 (1998).

67. Knight, J. . C., Birks, T. . A., Russell, P. S. J. & Atkin, D. M. All-silica single-mode optical fiber with photonic crystal cladding. *Opt. Lett.* **21,** 1547–1549 (1996).

68. Knight, J. C., Birks, T. A., Russell, P. S. J. & de Sandro, J. P. Properties of photonic crystal fiber and the effective index model. *J. Opt. Soc. Am* **15,** 748–752 (1998).

69. Wang, Z. & Fan, S. Optical circulators in two-dimensional magneto-optical photonic crystals. *Opt. Lett* **30,** 1989–1991 (2005).

70. Giovampaola, C. Della & Engheta, N. Plasmonics without negative dielectrics. *Phys. Rev. B* **93,** 195152 (2016).

71. Li, Y., Liberal, I., Della Giovampaola, C. & Engheta, N. Waveguide metatronics: Lumped circuitry based on structural dispersion. *Sci. Adv.* **2,** (2016).

72. Edwards, B., Alù, A., Young, M. E. & Engheta, N. Experimental Verification of Epsilon-Near-Zero Metamaterial Coupling and Energy Squeezing Using a Microwave Waveguide Experimental Verification of Epsilon-Near-Zero Metamaterial Coupling. *Phys. Rev. Lett.* **100,** 033903 (2008).

73. Alù, A. & Engheta, N. Boosting Molecular Fluorescence with a Plasmonic Nanolauncher. *Phys. Rev. Lett.* **103,** 043902 (2009).

74. Sokhoyan, R. & Atwater, H. A. Quantum optical properties of a dipole emitter coupled to an ε - near-zero nanoscale waveguide. *Opt Express* **21,** 5238–5241 (2013).

75. Fakonas, J. S., Lee, H., Kelaita, Y. A. & Atwater, H. A. Two-plasmon quantum interference. *Nat. Photonics* **8,** 317–320 (2014).

76. Dicke, R. H. Coherence in Spontaneous Radiation Processes. *Phys. Rev.* **93,** (1954).

77. Tiranov, a. D. & Kalachev, a. a. Collective spontaneous emission in a waveguide

with a near-zero refractive index. *Bull. Russ. Acad. Sci. Phys.* **78,** 176–179 (2014).

78. Zeng, X., Li, G., Yang, Y. & Zhu, S. Enhancement of the vacuum Rabi oscillation via surface plasma modes in single-negative metamaterials. *Phys. Rev. A* **86,** 033819 (2012).

79. Zeng, X., Xu, J. & Yang, Y. Spontaneous emission interference enhancement with a μ-negative metamaterial slab. *Phys. Rev. A* **84,** 033834 (2011).

80. Yang, Y., Xu, J., Chen, H. & Zhu, S. Quantum Interference Enhancement with Left-Handed Materials. *Phys. Rev. Lett.* **100,** 043601 (2008).

81. Song, G., Xu, J. & Yang, Y. Quantum interference between Zeeman levels near structures made of left-handed materials and matched zero-index metamaterials. *Phys. Rev. A* **89,** 053830 (2014).

82. Kästel, J. & Fleischhauer, M. Suppression of spontaneous emission and superradiance over macroscopic distances in media with negative refraction. *Phys. Rev. A* **71,** 1–011804 (2005).

83. Kästel, J. & Fleischhauer, M. Suppression of spontaneous emission and superradiance over macroscopic distances in media with negative refraction. *Phys. Rev. A* **71,** 011804 (2005).

84. Mart, L. & Garc, F. J. Superradiance mediated by graphene surface plasmons. **155438,** 1–6 (2012).

85. Huidobro, P. a., Nikitin, a. Y., González-Ballestero, C., Martín-Moreno, L. & García-Vidal, F. J. Superradiance mediated by graphene surface plasmons. *Phys. Rev. B* **85,** 155438 (2012).

86. Song, G., Xu, J. & Yang, Y. Spontaneous emission of a two-level system near the interface of topological insulators. *EPL (Europhysics Lett.* **105,** 64001 (2014).

87. Liu, Z., Li, W., Jiang, X. & Cao, J. C. Spontaneous emission from a medium with elliptic and hyperbolic dispersion. *Phys. Rev. A* **87,** 053836 (2013).

88. Wang, Z., Chong, Y., Joannopoulos, J. D. & Soljacić, M. Observation of unidirectional backscattering-immune topological electromagnetic states. *Nature* **461,** 772–775 (2009).

89. Yu, Z., Wang, Z. & Fan, S. One-way total reflection with one-dimensional magneto-optical photonic crystals. *Appl. Phys. Lett.* **90,** 23–25 (2007).

90. Davoyan, A., Mahmoud, A. & Engheta, N. Optical isolation with epsilon-near-zero metamaterials. *Opt. Express* **21,** 3279–3286 (2013).

91. Yu, Z. & Fan, S. Integrated Nonmagnetic Optical Isolators Based On Photonic Transitions. *IEEE J. Sel. Top. Quantum Electron.* **16,** 459–466 (2010).

92. Fan, L. *et al.* An All-Silicon Passive Optical Diode. *Science,* **335,** 447–450 (2012).

93. Fan, L. *et al.* Silicon optical diode with 40 dB nonreciprocal transmission. *Opt. Lett.* **38,** 1259–1261 (2013).

94. Fan, Y. *et al.* Subwavelength electromagnetic diode: One-way response of cascading nonlinear meta-atoms. *Appl. Phys. Lett.* **98,** 151903 (2011).

95. Miroshnichenko, A. E., Brasselet, E. & Kivshar, Y. S. Reversible optical nonreciprocity in periodic structures with liquid crystals. *Appl. Phys. Lett.* **96,** 063302 (2010).

96. Wang, J. *et al.* A Theoretical Model for an Optical Diode Built With Nonlinear Silicon Microrings. *J. Light. Technol.* **31,** 313–321 (2013).

97. Shadrivov, I. V, Fedotov, V. a, Powell, D. a, Kivshar, Y. S. & Zheludev, N. I. Electromagnetic wave analogue of an electronic diode. *New J. Phys.* **13,** 033025 (2011).

98. Zhang, Y. *et al.* Silicon optical diode based on cascaded photonic crystal cavities. *Opt. Lett.* **39,** 1370–1373 (2014).

99. Chang, L. *et al.* Parity–time symmetry and variable optical isolation in active–passive-coupled microresonators. *Nat. Photonics* **8,** 524–529 (2014).

100. Nazari, F. *et al.* Optical isolation via PT symmetric nonlinear Fano resonances. *Opt Express* **22,** 9574–9584 (2014).

101. Sahoo, P. K. & Joseph, J. Optical diode using nonlinear polystyrene ring resonators in two-dimensional photonic crystal structure. *Appl. Opt.* **52,** 8252–8257 (2013).

102. Li, N. & Ren, J. Non-reciprocal geometric wave diode by engineering asymmetric shapes of nonlinear materials. *Sci. Rep.* **4,** 6228 (2014).

103. Kong, X., Liu, S., Zhang, H., Dai, Y. & Yang, H. A theoretical study of a compact and highly efficient isolator consisting of nonlinear plasma and matching metamaterials. *Laser Phys.* **23,** 055404 (2013).

104. Gallo, K. & Assanto, G. All-optical diode based on second-harmonic generation in an asymmetric waveguide. *J. Opt. Soc. Am. B* **16,** 267 (1999).

105. Gallo, K., Assanto, G., Parameswaran, K. R. & Fejer, M. M. All-optical diode in a periodically poled lithium niobate waveguide. *Appl. Phys. Lett.* **79,** 314 (2001).

106. Feise, M., Shadrivov, I. & Kivshar, Y. Bistable diode action in left-handed periodic structures. *Phys. Rev. E* **71,** 037602 (2005).

107. Cai, X., Wang, X. & Li, S. Design of ultrahigh-contrast all-optical diodes based on coupled nonlinear photonic crystal defects. *Opt. Commun.* **285,** 1959–1963 (2012).

108. Bulgakov, E. N. & Sadreev, A. F. All-optical diode based on dipole modes of Kerr microcavity in asymmetric L-shaped photonic crystal waveguide. *Opt. Lett.* **39,** 1787–1790 (2014).

109. Khanikaev, A. B., Mousavi, S. H., Shvets, G. & Kivshar, Y. S. One-way extraordinary optical transmission and nonreciprocal spoof plasmons. *Phys. Rev. Lett.* **105,** 1–4 (2010).

110. Fang, K., Yu, Z., Liu, V. & Fan, S. Ultracompact nonreciprocal optical isolator based on guided resonance in a magneto-optical photonic crystal slab. *Opt. Lett.*

36, 4254 (2011).

111. Kodera, T., Sounas, D. & Caloz, C. Artificial Faraday rotation using a ring metamaterial structure without static magnetic field. *Appl. Phys. Lett.* **16,** 16058–16063 (2011).

112. Wang, Z. *et al.* Gyrotropic response in the absence of a bias field. *Proc. Natl. Acad. Sci. U. S. A.* **109,** 13194–7 (2012).

113. Shi, Y., Yu, Z. & Fan, S. Limitations of nonlinear optical isolators due to dynamic reciprocity. *Nat. Photonics* **9,** 388–392 (2015).

114. Carretero-Palacios, S. *et al.* Optical switching in metal-slit arrays on nonlinear dielectric substrates. *Opt. Lett.* **35,** 4211–4213 (2010).

115. Minovich, A. *et al.* Liquid crystal based nonlinear fishnet metamaterials. *Appl. Phys. Lett.* **100,** 121113 (2012).

116. Sounas, D. L., Caloz, C. & Alù, A. Giant non-reciprocity at the subwavelength scale using angular momentum-biased metamaterials. *Nat. Commun.* **4,** 2407 (2013).

117. Peng, B. *et al.* Parity–time-symmetric whispering-gallery microcavities. *Nat. Phys.* **10,** 394–398 (2014).

118. Minovich, A., Neshev, D. N., Powell, D. a., Shadrivov, I. V. & Kivshar, Y. S. Tunable fishnet metamaterials infiltrated by liquid crystals. *Appl. Phys. Lett.* **96,** 24–26 (2010).

119. Lee, J. *et al.* Giant nonlinear response from plasmonic metasurfaces coupled to intersubband transitions. *Nature* **511,** 65 (2014).

120. Shadrivov, I. V, Kozyrev, A. B., Weide, D. W. Van Der & Kivshar, Y. S. Nonlinear magnetic metamaterials. **16,** 165112–165117 (2008).

121. Nonlinear Optics, Third Edition: Robert W. Boyd: 9780123694706: Amazon.com: Books.

122. Carbonell, J., Boria, V. E. & Lippens, D. Nonlinear effects in split ring resonators loaded with heterostructure barrier varactors. *Microw. Opt. Technol. Lett.* **50,** 474–479 (2008).

123. Kaloss, M. *et al.* A Hybridization Model for the Plasmon Response of. **302,** 419–423 (2003).

124. Minovich, A. *et al.* Liquid crystal based nonlinear fishnet metamaterials Liquid crystal based nonlinear fishnet metamaterials. **121113,** 1–4 (2012).

125. Mikhailov, S. A. Non-linear electromagnetic response of graphene. **27002,** 5 (2007).

126. Novoselov, K. S. *et al.* Electric Field Effect in Atomically Thin Carbon Films. *Science (80-.).* **306,** 666–669 (2004).

127. N. Engheta, R. W. Z. *Electromagnetic Metamaterials: Physics and Engineering Explorations*.

128. Pendry, J. B., Schurig, D. & Smith, D. R. Controlling electromagnetic fields. *Science* **312,** 1780–2 (2006).

129. Soukoulis, C. M. & Wegener, M. Materials science. Optical metamaterials--more bulky and less lossy. *Science* **330,** 1633–4 (2010).

130. Pendry, J. B. Negative Refraction Makes a Perfect Lens. *Phys. Rev. Lett.* **85,** 3966–3969 (2000).

131. Yu, N. *et al.* Light propagation with phase discontinuities: generalized laws of reflection and refraction. *Science* **334,** 333–7 (2011).

132. Ni, X., Emani, N. K., Kildishev, A. V, Boltasseva, A. & Shalaev, V. M. Broadband Light Bending with Plasmonic Nanoantennas. *Science* **335,** 427 (2012).

133. Sievenpiper, D., Broas, R. F. J., Alexopolous, N. G. & Yablonovitch, E. High-

impedance electromagnetic surfaces with a forbidden frequency band. *IEEE Trans. Microw. Theory Tech.* **47,** 2059–2074 (1999).

134. Burokur, S. N., Daniel, J.-P., Ratajczak, P. & de Lustrac, a. Tunable bilayered metasurface for frequency reconfigurable directive emissions. *Appl. Phys. Lett.* **97,** 064101 (2010).

135. Germain, D., Seetharamdoo, D., Nawaz Burokur, S. & de Lustrac, A. Phase-compensated metasurface for a conformal microwave antenna. *Appl. Phys. Lett.* **103,** 124102 (2013).

136. Genevet, P. *et al.* Flat Optics: Controlling Wavefronts With Optical Antenna Metasurfaces. *IEEE J. Sel. Top. Quantum Electron.* **19,** 4700423–4700423 (2013).

137. A. Kildishev, A. Boltasseva, V. S. Planar Photonics with Metasurfaces. *Science* **339,** 1232009–1 (2013).

138. Yu, N. & Capasso, F. Flat optics with designer metasurfaces. *Nat. Mater.* **13,** (2014).

139. Chen, P.-Y. *et al.* Nanostructured graphene metasurface for tunable terahertz cloaking. *New J. Phys.* **15,** 123029 (2013).

140. Fallahi, A. & Perruisseau-Carrier, J. Design of tunable biperiodic graphene metasurfaces. *Phys. Rev. B* **86,** 195408 (2012).

141. Hadad, Y., Davoyan, A. R., Engheta, N. & Steinberg, B. Z. Extreme and Quantized Magneto-optics with Graphene Meta-atoms and Metasurfaces. *ACS Photonics* **1,** 1068–1073 (2014).

142. Temnov, V., Armelles, G. & Woggon, U. Active magneto-plasmonics in hybrid metal–ferromagnet structures. *Nat. Photonics* **4,** 107–111 (2010).

143. Belotelov, V., Doskolovich, L. & Zvezdin, a. Extraordinary Magneto-Optical Effects and Transmission through Metal-Dielectric Plasmonic Systems. *Phys. Rev. Lett.* **98,** 077401 (2007).

144. Chin, J. Y. *et al.* Nonreciprocal plasmonics enables giant enhancement of thin-film Faraday rotation. *Nat. Commun.* **4,** 1599 (2013).

145. Mazor, Y. & Steinberg, B. Z. Metaweaves: Sector-Way Nonreciprocal Metasurfaces. *Phys. Rev. Lett.* **112,** 153901 (2014).

146. Ye, Y. & He, S. 90 Polarization Rotator Using a Bilayered Chiral Metamaterial With Giant Optical Activity. *Appl. Phys. Lett.* **96,** 2008–2011 (2010).

147. Espinola, R. L., Izuhara, T., Tsai, M. & Osgood, R. M. Magneto-optical nonreciprocal phase shift in garnet ¯silicon-on-insulator waveguides. *Opt. Lett.* **29,** 941–943 (2004).

148. Levy, M. Nanomagnetic route to bias-magnet-free, on-chip Faraday rotators. *J. Opt. Soc. Am. B* **22,** 254–260 (2005).

149. Zaman, T. R. *et al.* Faraday rotation in an InP waveguide Faraday rotation in an InP waveguide. *Appl. Phys. Lett.* **90,** 023514 (2007).

150. Soljac, M. & Joannopoulos, J. D. Enhancement of nonlinear effects using photonic crystals. *Nat. Mater.* **3,** 211–219 (2004).

151. Marin Soljacic, Chiyan Luo, J. D. Joannopoulos, S. F. Nonlinear photonic crystal microdevices for optical integration. *Opt. Lett.* **28,** 637–639 (2003).

152. Dong, P., Preble, S. F., Robinson, J. T., Manipatruni, S. & Lipson, M. Inducing Photonic Transitions between Discrete Modes in a Silicon Optical Microcavity. *Phys. Rev. Lett.* **100,** 033904 (2008).

153. Winn, J. N., Fan, S., Joannopoulos, J. D. & Ippen, E. P. Interband transitions in photonic crystals. *Phys. Rev. B* **59,** 1551–1554 (1999).

154. Lira, H., Yu, Z., Fan, S. & Lipson, M. Electrically Driven Nonreciprocity Induced by Interband Photonic Transition on a Silicon Chip. *Phys. Rev. Lett.* **109,** 033901 (2012).

155. Davoyan, A. R., Shadrivov, I. V & Kivshar, Y. S. Nonlinear plasmonic slot

waveguides. **16,** 21209–21214 (2008).

156. Alù, A. & Engheta, N. Light squeezing through arbitrarily shaped plasmonic channels and sharp bends. *Phys. Rev. B* **78,** 35440 (2008).

157. Liberal, I. & Engheta, N. Nonradiating and radiating modes excited by quantum emitters in open epsilon-near-zero cavities. *arXiv:1512.01092*

158. Liberal, I., Mahmoud, A. M. & Engheta, N. Geometry-invariant resonant cavities. *Nat. Commun.* **7,** 1–7 (2016).

159. Yu, Z. & Fan, S. Optical isolation based on nonreciprocal phase shift induced by interband photonic transitions. *Appl. Phys. Lett.* **94,** (2009).